MULTISCALE DISCRETE DAMAGE THEORY FOR FAILURE MODELING OF COMPOSITE MATERIALS

By

Zimu Su

Dissertation

Submitted to the Faculty of the

Graduate School of Vanderbilt University

in partial fulfillment of the requirements

for the degree of

DOCTOR OF PHILOSOPHY

in

Civil Engineering

August 31, 2022

Nashville, Tennessee

Approved:

Caglar Oskay, Ph.D.

Douglas E. Adams, Ph.D.

Ravindra Duddu, Ph.D.

Haoxiang Luo, Ph.D.

Nelson Carvalho, Ph.D.

ACKNOWLEDGMENTS

I firstly want to express my immense gratitude to my advisor Dr. Caglar Oskay. I benefit substantially from his way of critical thinking to the problem, rigorous attitude towards the fundamentals and outstanding vision over the research field. All of those characteristics encourage and inspire me to make improvements and become an eligible PhD researcher. I also thank him for the mentorship and careness to my life especially during the pandemic, which is a hard time for everybody, but I feel encouraged and supportive with his help and suggestions.

I would also like to express my gratitude to my committee members Dr. Ravindra Duddu, Dr. Douglas Adams and Dr. Haoxiang Luo. We have had valuable discussions on my research and PhD life, and they provided very insightful guidance to my dissertation proposal. I also want to thank Dr. Nelson Calvalho for the valuable feedback to the studies of delamination migration and in-situ composite characterization.

I much appreciate my colleagues in Multiscale Computational Mechanics Laboratory (MCML) for long-time companion with me. Especially, I'd like to thank Dr. Xiang Zhang, Dr. Ruize Hu, Dr. Xiaoyu Zhang, Damin Xia, Alex Faupel and Ido Meshi. We had great discussions about the research and helped each other on the difficulties.

I also would like to express my gratitude towards my friends, Haiping Huang, Qimeng Wang and Jin Wang who I firstly met in Vanderbilt University. I feel great thankful to every friday night dinner with you all. I also appreciate my friends I met at school of engineering in Vanderbilt University and my roommate Yu Wang for the help in life and the enjoyable time spent together. Last but not least, I would like to appreciate deeply to my parents Danlu Sun and Zhiqing Su who have supported me this five years all the ways in the good and bad times without any hesitation. Their encouragements are the greatest treasure in my PhD life.

Finally, I acknowledge the financial support of the Office of Naval Research Airframe Structures and Materials (Award No: N00014-17-1-2040, Program Manager: William C. Nickerson, Dr. Anisur Rahman), the Air Force Research Laboratory (Contract No: FA8650-12-D-3212/0016 under University of Dayton Research Institute Subcontract No. RSC16122, Program Managers: Dr. Steven E. Olson and Dr. Stephen B. Clay) and NASA Langley Research Center (Sub-award No: C21-202035-VU through National Institute of Aerospace. Technical Program Director: Dr. James Ratcliff).

TABLE OF CONTENTS

LIST OF TABLES

LIST OF FIGURES

CHAPTER 1

INTRODUCTION

1.1 Background

In recent years, the application of composite materials has grown rapidly in many industries (e.g. aerospace, automobile, civil infrastructure, energy) due to its high stiffness to weight ratio, strength and durability, etc. A typical example of increasing demand can be found in commercial aircraft production. In 1990s, only 5-6% of the aircraft structure was made from composite, while the state-of-art design of Boeing 787 aircraft composed of composite above 50% by weight and 80% by volume [1, 2]. The increasing industrial usage of composite requires certification and sustainment of composite structures for achieving safety and optimality. One of major concerns for composite tolerance design is the complexity of damage and failure process. For instance, the fiber-reinforced composite laminated structure exhibits multiple failure modes, such as matrix cracking, fiber fracture, delamination, fiber-matrix debonding, etc [3]. More complicated failure mechanisms exist for specific geometry and loading scenarios, such as delamination migration, kink band failure, fiber pull-out, crack branching and merging, etc. Achieving comprehensive understandings and predictive capabilities for those composite failure processes and their interaction would allow leveraging the full capabilities like the high specific strength, stiffness, durability, etc.

The complexity of composite failure results from the existence of heterogeneous material microstructure. The composite failure process can be attributed to nucleation, propagation, accumulation and coalescence of microcrack within the microstructure, which is significantly smaller than the structural scale. The localization of microcrack leads to formation of macrocrack and the composite exhibits non-linear failure process (i.e. softening). Thus, the composite failure has multiscale characteristics because it is obviously affected by geometry, spatial distribution and material properties of individual components [4, 5]. Those microstructural characteristics enables complex composite failure process. In addition, the stochastic scatter of the structural response or size effects can be explained by the random nature of heterogeneous microstructure [6].

Phenomenological model is a common method for macroscale composite failure analysis. It treats composite as homogenized material and neglects its microstructure heterogeneity. The ma-

terial constitutive law is calibrated in a phenomenological way and adopts effective material properties. It is very straightforward to implement and computational efficient. In those studies, many numerical techniques have been directly employed for macroscale simulations. Numerical methods based on classic linear elastic fracture mechanics (LEFM) include J-integral [7] or virtual crack extension and closure techniques (VCCT) [8]. LEFM-based approach considers brittle crack growth with the assumption of negligible fracture process zone and requires inserting one or multiple precracks in the specimen. Cohesive zone model (CZM) [9, 10] is another type of common methodology in computational fracture mechanics but relies on predefined crack path within the composite specimen. To allow the crack growth independent of mesh discretization, element enrichment methods, such as the extended finite elements (XFEM) [11], the phantom node method (PNM) [12] and the floating node method (FNM) [13] have been developed. Continuum damage mechanics (CDM) is also a common method for failure prediction of composites with more than one damage state variables to describe the degradation of composite material properties [14–16]. However, by simply modeling in a homogenized manner, the simplified treatment of the failure process such as microcrack nucleation can ignore the microcrack characteristics such as tortuosity, interaction between components. Besides, the parameters in the phenomenological model is usually difficult to calibrate in the physical test. The micromechanical analysis have investigated those microstructure effects in great details, such as microstructure morphology [17, 18], interfacial properties [19, 20], interfacial defect [21], thermal residual stress [19], among others. But direct simulation of microstructure can only focus on fine-scale failure mechanisms and its extension to larger scale can be computationally prohibitive.

Different from failure modeling in a single spatial scale, the multiscale framework integrates features at both fine and coarse spatial scales. In the multiscale model, the fundamental physics of microscopic failure mechanisms is derived by the in-situ microstructure modeling, which considers the influence factors like geometry, properties, distribution of individual components. The in-situ microscopic failure is then incorporated to macroscopic analysis, which considers the influence of structural component (such as notch, laminate ply direction, etc.) and loading scenarios. There are two main categories of multiscale model [22] in terms of treatment of micro and macroscale problems. The concurrent approach solves the fine and coarse scale problems simultaneously in the same domain and the exchange of information are defined through the interface defined by

either disjoint or overlap fashion in the spatial domain. The hierarchical method fully defines the microstructure, and its fine-scale response is averaged and bridged to the structural scale. This dissertation focuses on computational homogenization method, which belongs to the hierarchical approach. The homogenization method provides a rigorous framework and strong mathematical basis to derive the coarse-scale constitutive formulation based on the response of representative fine-scale sample (i.e. representative volume element, or RVE), which is the smallest volume over which a measurement can be made that will yield a value representative of the whole [23]. Over the past few decades, homogenization theory has been developed not limited to the range of elasticity, but also includes various problems of material non-linearity, including plasticity (e.g. [24]), brittle fracture (e.g. [25]), large-deformation (e.g. [26]), etc.

1.2 Problem Statement and Motivation

1.2.1 Multiscale Failure Modeling

The adoption of homogenization method for failure prediction requires overcoming a number of computational challenges. For instance, when progressive failure is described using the continuum damage mechanics approach, localization limiters must be employed at all relevant scales to ensure mesh objectivity. Regardless of continuum or discrete representation of failure, consistent bridging of failure information across scales (i.e., homogenization and localization operators) must be established. In the presence of localization of damage, statistical homogeneity and ergodicity at the scale of the microstructure is lost and a representative volume element (RVE) cannot be defined [27]. An additional, no less critical challenge is that the computational cost associated with evaluating multiple nested numerical problems that involve failure and fracture processes is typically computationally prohibitive beyond small problems of academic relevance. In the past decade, significant effort has been therefore devoted to alleviate the above-mentioned computational challenges.

A number of early studies focused on applying computational homogenization principles to address problems, where fracture is localized to material interfaces (see e.g., [28, 29]). The applicability and generality of homogenization method to address fracture problems has been further extended since then. The formulations of homogenization method for fracture typically differ slightly according to the type of representation of failure at the fine and coarse scales. Discrete-discrete (for fine and coarse scales respectively), continuum-discrete and continuum-continuum representations

have been proposed. From the algorithmic standpoint, the work by Belytschko et al. [30] is of significance as it introduced the concept of microstructural domain splitting to bridge the fracture process and the bulk behavior separately across scales. The idea has been employed by a number of others since then. Verhoosel et al. [31] introduced the methodology to link the progressive evolution (i.e., cohesive cracks) of macroscopic interfacial and bulk cracks to the corresponding microscopic processes in the discrete-discrete sense. This approach was later extended to continuum-discrete failure representations [32, 33]. Coenen et al. [34] introduced a methodology to perform bulk and discontinuity upscaling without the need for microstructure domain splitting. Bosco et al. [35] extended this methodology to account for strain discontinuities across the macroscale crack surface. A computational framework similar to above that includes strong discontinuity enrichment has been developed in Ref. [36].

Extending homogenization method to problems where failure at the coarse scale is modeled in a continuum setting typically requires a different treatment to achieve objective formulations. One approach is to explicitly treat the coarse scale problem using a nonlocal formulation (e.g., gradient or integral type localization limiter [37, 38]). Kouznetsova et al. [39] proposed a gradient enhanced homogenization method to study localization problems where the characteristic length of localization is larger than the microstructure size. Oliver et al. [40] proposed a multiscale approach, where failure at each scale is represented using the continuum strong discontinuity approach. Leveraging their earlier work on RVE existence, Gitman et al. [41] proposed an alternative scale bridging strategy, in which the RVE size is tied to the macroscale finite element size for regularization, named the couple volume approach. An idea similar to the couple volume approach is employed in the dissertation.

While the elegant theories mentioned above provide a consistent upscaling strategy in the presence of nucleation and propagation of failure, they are often computationally too costly for application to problems that involve large structures. Due to this limitation, a significant majority (if not all) of these approaches has been applied in 2-D problems. The high computational cost can be alleviated using either surrogate modeling (e.g., machine learning [42–44]) or basis reduction strategies, such as proper orthogonal decomposition [45], proper generalized decomposition [46], fast Fourier transform [47], non-linear transformation field analysis [48, 49], and eigendeformation-based homogenization [50–54], etc. A multiscale model need to be established with consistent formulations

addressing all the aforementioned complications (i.e. ill-posed strain softening, violation of RVE, prohibitive computational cost).

1.2.2 Composite Fatigue

Long-term fatigue degradation of composite structures remains to be a structural design consideration. Studies that couple Paris Law (or a variant) with J-integral, VCCT (e.g. [8, 13, 55]) have been employed to study crack growth in composite laminates. CZM is mostly used for fatigue interlaminar crack growth (e.g. [56, 57]). Some studies also used CZM to describe intralaminar crack propagation [58–60] by placing cohesive zone elements at all element faces. More common practices employ element enrichment technologies, such as XFEM [61, 62], PNM [63] and FNM [13] to represent the crack configuration without limitation of mesh bias, while CZM and VCCT are employed for modeling the crack growth within it. CDM is another common methodology to explore fatigue response in composite material (e.g. [64–66]) due to its simplicity and directness for computational implementation. CDM-based multiscale model has been developed recently. Arnold et al. [67] employed the Generalized Method of Cells accelerated with cycle jump approach. Oskay et al. proposed a multiscale spatial-temporal life prediction approach that relies on model order reduction in space and time [68–70]. However, the related mesh-size sensitivity issue has received little attention for fatigue. Only nonlocal approach using gradient damage type [71] and integral type [72] localization limiters have been employed to achieve mesh-size objectivity in the fatigue case.

1.2.3 Failure Modeling for Delamination Migration

Delamination migration is a typical type of kinking (or re-oriented) cracks in composites. It has been observed in low-velocity impact [73], stiffener debonding [74], and notched multidirectional laminates [75] among others. The migration behavior is associated with the local micro crack accumulation at the delamination front, which becomes kinked crack if energetically favorable and reverts to delamination growth at another ply interface [76]. The difficulty of delamination migration modeling lies in adaptivity of failure modeling to arbitrary oriented crack propagation which is dependent on the local loading state. Many studies employ element enrichment method to alleviate the limitation of fixed crack path setting in computation fracture mechanics method. The combi-

nation of VCCT and FNM [76, 77], CZM and FNM [78–80], CZM and XFEM [11], CZM and regularized XFEM [81] have been reported for delamination migration modeling in different configurations of multidirectional laminates. Continuum damage modeling (CDM) has also been used to model delamination migration [82–84]. In the context of multiscale model, an adaptive strategy needs to be proposed to model the arbitrary-oriented crack in the a-priori defined microstructure.

1.2.4 Shear Non-linearity

The unidirectional composite laminates under shear loading exhibits significant non-linear deformation which might significantly reduce the loading capacity of composite structure. The phenomenological models (such as Tsai and Hahn criterion [85]), and plasticity/viscoplasticity theory [86, 87] are the two main types of approach for shear non-linearity modeling. Plasticity or viscoplasticity theory can be integrated in the multiscale framework based on eigen-strain homogenization theory. The theory leverages the decomposition of elastic and inelastic strain (i.e. plasticity/viscoplasticity flow) in different volumetric parts which are a-priori partitioned within the microstructure domain. Besides, approximation basis is applied to evaluate inelastic strain field for model reduction. However, the spurious over-stiff non-linear response has been observed due to the stress redistribution around the elastic fiber and yielded matrix (fiber has much higher yield stress than matrix). Alleviation strategy needs to be developed to regularize the inaccurate approximation of inelastic strain field.

1.2.5 In-situ Properties Characterization

Besides the aforementioned computational challenges in the development of multiscale model, an accurate calibration of in-situ material properties (i.e., elasticity, thermal, fracture) is also critical as it provides a reliable input for the multiscale model to achieve accurate outcome. Those constituent material parameters are typically identified by a combination of (1) inverse calibration informed by experiments at a larger scale [88–93]; and (2) ex-situ experiments that isolates a specific property (e.g., fiber pullout for shear dominated interface failure [94], fiber tensile testing [95]). In certain cases, molecular dynamics have also been employed to estimate constituent properties of some materials [18, 96]. A number of complicating factors present difficulties for identification of composite constituent parameters. Some of the composite constituents, e.g., many matrix materials,

exhibit significant differences in their in-situ and ex-situ behavior [97–99], therefore relying purely on ex-situ experimentation to characterize all properties is often not possible. Inverse calibration with experiments at larger scale often results in non-unique parameter sets, which may result in different microscale or structural response prediction, contributing to prediction uncertainty. Furthermore, all experiments exhibits certain amount of measurement noise that could lead to erroneous properties, the magnitude of which is seldom quantified.

Characterization of composite constituent properties based on in-situ experiments at the microscale offers an alternative approach. Nanoidentation testing have been employed to investigate the in-situ properties of composite materials including the Young's modulus [97, 98], plasticity [100], and viscoplasticity [99] by indenting the substrate of individual constituent within a small localized region of the specimen. The spatial variation of matrix stiffness has also been observed at small length scales at the fiber-matrix interphase regions (e.g. [101, 102] in polymer matrix composite). Hardiman et al. [98] observed that the stiffness variation is related to the size of resin pockets in a carbon fiber reinforced polymer (CFRP). Quantitative measurement of properties using nanoindentation requires that the effect of fiber constraints should be alleviated [98, 103]. The presence of fibers enables the indentation at the interphase and resin pocket to overestimate the in-situ properties [104].

Image-based measurement techniques, such as digital image correlation (DIC) [105–108], X-ray Computed Tomography (CT) [109] and template matching (TM) [110] has been advancing to provide detailed and accurate measurements at the scale of the composite microstructure. Combining high-magnification microscopy and high-resolution digital imaging, microscale image-based measurement methods measure displacement and strain field at the scale of fiber in the composite materials with or without presence of failure [105–108]. Similar to nano-indentation studies [97, 98], significant discrepancies were discovered in the deformation of epoxy resin in a CFRP between DIC measurements and the outcomes of simulations, which used constitutive properties of the bulk material [107]. To the best of the author's knowledge, rich datasets obtained from image-based measurement techniques have not been deployed in systematic studies to characterize the in-situ constitutive properties or models.

1.3 Objectives

The dissertation proposes a new multiscale model for failure analysis of composite materials and outlines a series of numerical studies to extend its application to various failure problems, including fatigue, delamination migration, shear non-linearity. Besides, a robust optimization framework is established for inverse characterization of in-situ composite properties. Addressing the above topics leads to the formulation of following objectives:

1. Develop a discrete-continuum multiscale model based reduced-order computational homogenization approach, which is also called multiscale discrete damage theory (MDDT). Establish regularization formulation to achieve mesh size objectivity and multiscale consistency.

2. Extend MDDT model with the capabilities to predict fatigue failure of laminated composite with high computational efficiency. Investigate regularization for mesh-size objectivity in fatigue failure modeling.

3. Extend MDDT with adaptivity of failure modeling to kinking crack propagation. Apply the proposed extension for delamination migration modeling.

4. Investigate the capability of homogenized-based multiscale model to describe shear-nonlinearity within the matrix phase. Develop regularization method for the spurious over-stiff non-linear response.

5. Use optimization approach to inversely characterize in-situ epoxy resin properties in fiber-reinforced composite based on image-based measurement of microscopic displacements. Mitigate the effect of random measurement noise on the characterization results.

1.4 Dissertation Outline

Chapter 2 demonstrates the fundamentals of multiscale discrete damage theory. The formulations of the proposed modeling approach are established based on homogenization method and eigen-deformation theory. The basis reduction approach and the treatment of mesh size objectivity are discussed. The proposed model is verified in the context of unnotched and notched laminated composite configurations. This chapter covers the work published in Ref. [25].

In chapter 3, the MDDT approach is extended with temporal multiscale model to achieve computational efficiency for fatigue analysis. The detailed treatment for mesh-size objectivity and related fatigue cohesive model are discussed. The verification are conducted in the context of unnotched and open-hole laminated composite configurations. A parametric study is conducted in terms of mode-I and mode-II fatigue damage evolution parameters to explain the fatigue failure behavior in composite laminates. The content in this chapter has been published in Ref. [111].

In chapter 4, the effective microstructure rotation and identification criterion for microcrack nucleation are proposed for adaptivity of MDDT to re-oriented or kinking crack propagation. The proposed model is verified in the context of unnotched specimens under multiaxial loading conditions. The model is then applied to four point bending analysis of notched concrete beam and delamination migration modeling with experimental validation. The study presented in this chapter has been published in Ref. [112].

In chapter 5, visco-plasticity theory is integrated into multiscale homogenization theory for modeling shear non-linearity. The phenomenon of over-stiff non-linear response after yielding is investigated. The regularization strategy is discussed and verified in the context of un-notched specimen.

Chapter 6 proposes a generalized framework for inverse characterization of in-situ composite material properties based on microscopic displacement measurement. The formulations for robust optimization are proposed to mitigate effect of random measurement noise based on statistical inference theory.

Chapter 7 summarizes the final conclusions and main contributions from those research studies, and discusses the potential development of MDDT approach for the future research.

CHAPTER 2

MULTISCALE DISCRETE DAMAGE THEORY (MDDT)

2.1 Introduction

This chapter proposes a new multiscale scheme for composite failure modeling based on reduced-order homogenization theory. Discrete-continuum representation of failure is employed at fine and coarse scale. The a-priori defined microstructure is embedded with multiple discrete failure interfaces, each of which is also called failure path for a potential failure mode. The microscopic failure process is bridged to continuum representation of damage at the coarse scale, standing for diffuse damage observed at a larger spatial scale. Model reduction technique is employed by utilizing basis function to approximate the cohesive separation along the failure path. The issue of mesh-size sensitivity related to continuum damage representation is alleviated by a new proposed regularization scheme, wherein the microstructure size is adjusted in an effective manner by scaling coefficient tensors as a function of macroscopic element size using analytical relationship. The proposed MDDT formulations and regularization scheme are verified in the context of un-notched specimen, notched single lamina and cross-ply laminates.

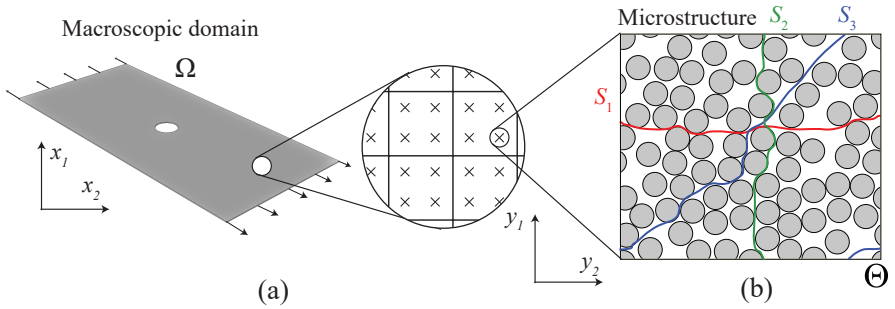

Figure 2.1: Spatial multiscale modeling strategy for composite laminates. (a) Macroscopic domain (b) Microstructure domain, S_i (i=1,2,3) denote failure paths (surfaces in 3-D).

2.2 Formulations

2.2.1 Eigendeformation-based Homogenization Method

Consider a heterogeneous structure that occupies a domain, $\Omega \subset \mathbb{R}^{n_{\mathrm{sd}}}$, where $n_{\mathrm{sd}} = 2, 3$ is the number of spatial dimensions. The body is made of a periodic arrangement of a microstructural volume, which is denoted as $\Theta \subset \mathbb{R}^{n_{\mathrm{sd}}}$ and typically consists of two or more material constituents. Only brittle or quasi-brittle fracture are considered in the failure path in this chapter. The effect of additional nonlinear processes (e.g., shear nonlinearity within the matrix) will be considered in chapter 5. Due to the geometrical arrangement of the constituents at the micro- or mesoscales (e.g., laminated configurations of a unidirectionally reinforced composite), the fracture patterns within the structure could be complex and diffuse. Propagating cracks may change direction to follow a load path, or multiple cracks may form within different parts or individual components and interact.

The proposed approach is based on the computational homogenization method with multiscale spatial scales [113]. The macroscopic and the microstructural domains are parameterized using position coordinates, $\mathbf{x}$ and $\mathbf{y}$, respectively (Fig. 2.1). The two scales are related to each other by the scaling parameter, $0 < \zeta \ll 1$ such that $\mathbf{y}(\mathbf{x}) = \mathbf{x}/\zeta$, and the response fields (e.g., displacement, stress, strain) are expressed as a function of the micro- and macroscopic coordinates. The governing equations of the boundary value problems are obtained through a two-scale asymptotic analysis, the details of which are skipped herein for brevity and available in the literature [113–115].

The displacement field over the microstructure, $\mathbf{u}$ is expressed in terms of a two-scale asymptotic decomposition:

$$\mathbf{u}\left(\mathbf{x}, \mathbf{y}, t\right) = \mathbf{u}^0\left(\mathbf{x}, t\right) + \zeta \mathbf{u}^1\left(\mathbf{x}, \mathbf{y}, t\right) \tag{2.1}$$

The leading order displacement field $\mathbf{u}^0$ is continuous and constant across the microstructure. The microcrack nucleates discontinuity of microscopic displacement field (i.e. displacement jump or separation) along the surface $S_a \subset \mathbb{R}^{n_{\mathrm{sd}}-1}$: $\boldsymbol{\delta}_a\left(\mathbf{x}, \mathbf{y}, t\right) := [\![\mathbf{u}^1]\!]$. The microscale displacement field $\mathbf{u}^1$ and the separation $\boldsymbol{\delta}$ are taken to be periodic over the microstructure and their contribution to the overall displacement field is of $O(\zeta)$. Employing the concept of eigen-separations [51] and the classical mathematical homogenization, the microstructural displacement field is expressed as:

$$\mathbf{u}^1\left(\mathbf{x}, \mathbf{y}, t\right) = \mathbf{H}\left(\mathbf{y}\right) : \boldsymbol{\epsilon}^0\left(\mathbf{x}, t\right) + \sum_{a=1}^{n} \left(\mathbf{h}_a * \boldsymbol{\delta}_a\right)\left(\mathbf{x}, \mathbf{y}, t\right) \tag{2.2}$$

where, $\boldsymbol{\epsilon}^0 = \nabla^s_{\mathbf{x}}\mathbf{u}^0$, $\nabla^s_{\mathbf{x}}$ is the symmetric gradient operator with respect to the macroscopic coordinates, considering the small strain theory, $\mathbf{H}(\mathbf{y})$ and $\mathbf{h}_a(\mathbf{y}, \hat{\mathbf{y}})$ are the elastic and separation influence functions of the microstructure, respectively, and $(\cdot * \cdot)_{Sa}$ denotes the convolution operation over the discontinuity path, S_a:

$$(\mathbf{h}_a * \boldsymbol{\delta}_a)_{S_a}(\mathbf{x}, \mathbf{y}, t) = \int_S \mathbf{h}_a(\mathbf{y}, \hat{\mathbf{y}}) \cdot \boldsymbol{\delta}_a(\mathbf{x}, \hat{\mathbf{y}}) d\hat{\mathbf{y}} \tag{2.3}$$

The third-order elastic influence function, $\mathbf{H}$ provides the variation of the response over the microstructure volume. The second-order separation influence function $\mathbf{h}_a$ can be considered as green function as response to normal and tangential separations applied along the discontinuity path. The numerical evaluation of $\mathbf{H}$ and $\mathbf{h}_a$ are provided in Ref. [51, 114].

Taking the symmetric gradient of Eq. 2.2, the strain field over the microstructure is expressed as:

$$\boldsymbol{\epsilon}(\mathbf{x}, \mathbf{y}, t) = \boldsymbol{\epsilon}^0(\mathbf{x}, t) + \boldsymbol{\epsilon}^1_{\mathbf{y}}(\mathbf{x}, \mathbf{y}, t) = \mathbf{A}(\mathbf{y})\boldsymbol{\epsilon}^0 + \sum_{a=1}^{n} (\mathbf{g}_a * \boldsymbol{\delta}_a)_S \tag{2.4}$$

where $\boldsymbol{\epsilon}^1_{\mathbf{y}} = \nabla^s_{\mathbf{y}}\mathbf{u}^1$, $\mathbf{A} = \mathbf{I} + \mathbf{G}$, $\mathbf{I}$, $\mathbf{I}$ is the fourth order identity tensor, $\mathbf{G} = \nabla^s_{\mathbf{y}}\mathbf{H}$ is the elastic polarization tensor, and $\mathbf{g}_a = \nabla^s_{\mathbf{y}}\mathbf{h}_a$ stands for the separation polarization tensor. The macroscopic strain, $\bar{\boldsymbol{\epsilon}}$ is obtained by averaging Eq. 2.4 over the domain of the microstructure:

$$\bar{\boldsymbol{\epsilon}}(\mathbf{x}, t) := \langle \boldsymbol{\epsilon} \rangle_\Theta = \boldsymbol{\epsilon}^0(\mathbf{x}, t) + \langle (\mathbf{g}_a * \boldsymbol{\delta}_a)_{S_a} \rangle_\Theta \tag{2.5}$$

where, $\langle \cdot \rangle_\Theta$ denotes the volume (or surface) averaging operator with respect to the domain denoted in the subscript. Because the separation influence function is discontinuous across the discontinuity path, its averaging over the microstructure volume becomes zero due to periodicity setting. Therefore, the second term in Eq. 2.5 vanishes: $\langle (\mathbf{g} * \boldsymbol{\delta})_{S_a} \rangle_\Theta = (\langle \mathbf{g}_a \rangle_\Theta * \boldsymbol{\delta})_{S_a} = \mathbf{0}$, and hence $\bar{\boldsymbol{\epsilon}} = \boldsymbol{\epsilon}^0$.

The microscale equilibrium equation defined over the microstructural volume is:

$$\nabla_{\mathbf{y}} \cdot \boldsymbol{\sigma}(\mathbf{x}, \mathbf{y}, t) = \nabla_{\mathbf{y}} \cdot (\mathbf{L}(\mathbf{y}) : \boldsymbol{\epsilon}) = \mathbf{0}; \quad \mathbf{y} \in \Theta \tag{2.6}$$

where $\boldsymbol{\sigma}$ denotes stress, and $\mathbf{L}$ is the tensor of elastic moduli associated with the spatial point

in microstructure and varies in different material constituents. Substituting Eqs. 2.4 and 2.5 into Eq. 2.6, premultiplying the resulting equation with the influence function, $\mathbf{h}_a$ and integrating over the microstructure yields ($\forall \hat{\mathbf{y}} \in S_a$):

$$\mathbf{t}_a\left(\mathbf{x}, \hat{\mathbf{y}}, t\right) - \mathbf{C}_a\left(\hat{\mathbf{y}}\right) : \bar{\boldsymbol{\epsilon}}\left(\mathbf{x}, t\right) - \sum_{b=1}^{n} \int_{\Theta} \mathbf{g}_a\left(\mathbf{y}, \hat{\mathbf{y}}\right) : \mathbf{L}\left(\mathbf{y}\right) : \left(\mathbf{g}_b * \boldsymbol{\delta}_b\right)\left(\mathbf{x}, \mathbf{y}, t\right) d\mathbf{y} = \mathbf{0} \tag{2.7}$$

where, $\mathbf{t}_a$ is the traction along the discontinuity path, and $\mathbf{C}_a$ is a third order coefficient tensor:

$$\mathbf{C}_a\left(\hat{\mathbf{y}}\right) := \int_{\Theta} \mathbf{g}_a\left(\mathbf{y}, \hat{\mathbf{y}}\right) : \mathbf{L}\left(\mathbf{y}\right) : \mathbf{A}\left(\mathbf{y}\right) d\mathbf{y} \tag{2.8}$$

The weak equilibrium statement in Eq. 2.7 can be also considered as applying weighted residuals method with collocation over the discontinuity path. It provides the microstructural equilibrium state consisting of traction, separations along the discontinuity path and homogenized strain induced in the microstructure volume. Eq. 2.7 is closed by introducing cohesive traction-separation constitutive law:

$$\mathbf{t} = \hat{\mathbf{t}}\left(\boldsymbol{\delta}, \mathbf{q}\right) \tag{2.9}$$

where $\mathbf{q}$ denote a vector of internal state variables that define the evolution of the cohesive law. It is only dependent on material constituent and the subscript $(\cdot)_a$ is omitted here. The proposed model admits various forms of constitutive laws for the cohesive behavior such as the classical bi-linear [116] and others (e.g. [68, 69]).

2.2.2 Model Reduction

A number of reduced-order basis functions, $N^{(a\alpha)}$ are applied to the separation variable in the discontinuity path:

$$\boldsymbol{\delta}_a\left(\mathbf{x}, \mathbf{y}, t\right) = \sum_{\gamma=1}^{m_a} N^{(a\gamma)}\left(\mathbf{y}\right) \boldsymbol{\delta}^{(a\gamma)}\left(\mathbf{x}, t\right); \quad \mathbf{y} \in S_a \tag{2.10}$$

where $\boldsymbol{\delta}^{(a\gamma)}$ denotes the reduced-order separation coefficient associated with the γ^{th} basis function within the discontinuity path a, m_a is the corresponding number of basis functions. For simplicity, the coefficients can be marked with an unified index for the basis function among all the failure path: $(a\gamma)$ $\{a = 1 : n;\, \gamma = 1 : m_a\} \rightarrow (\alpha)\{\alpha = 1 : m\}$, and $S^{(\alpha)} = S_a$ for all $\gamma = 1 : m_a$. Denoting

$m = \sum_{a=1}^{n} m_a$ for total number of basis functions and S for all discontinuity path: $S = \cup_{a=1}^{n} S_a$, Eq. 2.10 becomes:

$$\boldsymbol{\delta}\left(\mathbf{x}, \hat{\mathbf{y}}, t\right) = \sum_{\alpha=1}^{m} N^{(\alpha)}\left(\hat{\mathbf{y}}\right) \boldsymbol{\delta}^{(\alpha)}\left(\mathbf{x}, t\right); \quad \hat{\mathbf{y}} \in S^{(\alpha)} \tag{2.11}$$

The separation coefficients can be inversely evaluated as a function of nonlocal weight function:

$$\boldsymbol{\delta}^{(\alpha)}\left(\mathbf{x}, t\right) = \int_{S} \nu^{(\alpha)}\left(\hat{\mathbf{y}}\right) \boldsymbol{\delta}\left(\mathbf{x}, \hat{\mathbf{y}}, t\right) d\hat{\mathbf{y}} \tag{2.12}$$

where the basis and weight functions must satisfy the following constraints [52]:

$$\text{Orthonormality:} \quad \int_S \nu^{(\alpha)}\left(\hat{\mathbf{y}}\right) N^{(\beta)}\left(\hat{\mathbf{y}}\right) d\hat{\mathbf{y}} = \delta_{\alpha\beta} \tag{2.13a}$$

$$\text{Partition of unity:} \quad \sum_{\alpha=1}^{m} N^{(\alpha)}\left(\hat{\mathbf{y}}\right) = 1; \quad \hat{\mathbf{y}} \in S \tag{2.13b}$$

$$\text{Positivity:} \quad \nu^{(\alpha)}\left(\hat{\mathbf{y}}\right) \geq 0; \quad \hat{\mathbf{y}} \in S \tag{2.13c}$$

$$\text{Normality:} \quad \int_S \nu^{(\alpha)}\left(\hat{\mathbf{y}}\right) d\hat{\mathbf{y}} = 1 \tag{2.13d}$$

Substituting Eq. 2.11 into Eq. 2.7, premultiplying the resulting equation with the weight function $\nu^{(\alpha)}$ and integrating over the discontinuity path, $S^{(\alpha)}$ results in the following expression:

$$\mathbf{t}^{(\alpha)}\left(\mathbf{x}, t\right) - \mathbf{C}^{(\alpha)} : \bar{\boldsymbol{\epsilon}}\left(\mathbf{x}, t\right) + \sum_{\beta=1}^{m} \mathbf{D}^{(\alpha\beta)} \cdot \boldsymbol{\delta}^{(\beta)}\left(\mathbf{x}, t\right) = \mathbf{0}; \quad \alpha = 1, 2, \ldots, m \tag{2.14}$$

where the coefficient tensors after model reduction are expressed as:

$$\mathbf{C}^{(\alpha)} := \int_{S^{(\alpha)}} \nu^{(\alpha)}\left(\mathbf{y}\right) \mathbf{C}\left(\mathbf{y}\right) d\mathbf{y} \tag{2.15}$$

$$\mathbf{D}^{(\alpha\beta)} := -\int_{S^{(\alpha)}} \nu^{(\alpha)}\left(\mathbf{y}\right) \mathbf{D}^{(\beta)}\left(\mathbf{y}\right) \tag{2.16}$$

$$\mathbf{D}^{(\alpha)}\left(\hat{\mathbf{y}}\right) := \int_{\Theta} \mathbf{g}\left(\mathbf{y}, \hat{\mathbf{y}}\right) : \mathbf{L}\left(\mathbf{y}\right) : \mathbf{R}^{(\alpha)}\left(\mathbf{y}\right) d\mathbf{y} \tag{2.17}$$

$$\mathbf{R}^{(\alpha)}\left(\mathbf{y}\right) := \int_{S^{(\alpha)}} N^{(\alpha)}\left(\hat{\mathbf{y}}\right) \mathbf{g}\left(\mathbf{y}, \hat{\mathbf{y}}\right) d\hat{\mathbf{y}} \tag{2.18}$$

The unit normal to the discontinuity path (or failure path), $\mathbf{n}^{(\alpha)}$ can be expressed as:

$$\mathbf{n}^{(\alpha)} := \frac{1}{|S^{(\alpha)}|} \int_{S^{(\alpha)}} N^{(\alpha)}\left(\hat{\mathbf{y}}\right) \mathbf{n}\left(\hat{\mathbf{y}}\right) d\hat{\mathbf{y}} \tag{2.19}$$

The reduced order microscale problem is an algebraic nonlinear system of equations (i.e. Eq. 2.14, 2.9) in which, the macroscale strain acts as the forcing function and the traction and separation coefficients are evaluated as unknowns. The number of equations at certain macroscopic point depends on spatial dimensions and number of basis functions: $n_{\mathrm{sd}} \times m$. In this thesis, the form of piecewise function is employed for the approximation basis due to its simplicity:

$$N^{(\alpha)}\left(\hat{\mathbf{y}}\right) = \begin{cases} 1 & \text{if } \hat{\mathbf{y}} \in S^{(\alpha)} \\ 0 & \text{elsewhere} \end{cases} \qquad \nu^{(\alpha)}\left(\hat{\mathbf{y}}\right) = \begin{cases} 1/|S^{(\alpha)}| & \text{if } \hat{\mathbf{y}} \in S^{(\alpha)} \\ 0 & \text{elsewhere} \end{cases} \tag{2.20}$$

The rest of pieces is the macroscopic stress-strain relationship as a function of separation coefficients. By averaging the stress field over the microstructure volume, there is:

$$\bar{\boldsymbol{\sigma}}\left(\mathbf{x},t\right) := \left\langle \boldsymbol{\sigma}\left(\mathbf{x},\mathbf{y},t\right)\right\rangle_{\Theta} = \bar{\mathbf{L}} : \bar{\boldsymbol{\epsilon}}\left(\mathbf{x},t\right) + \sum_{\alpha=1}^{m} \mathbf{Z}^{(\alpha)} \cdot \boldsymbol{\delta}^{(\alpha)}\left(\mathbf{x},t\right) \tag{2.21}$$

where,

$$\mathbf{Z}^{(\alpha)} := \left\langle \mathbf{L}\left(\mathbf{y}\right) : \mathbf{R}^{(\alpha)}\left(\mathbf{y}\right)\right\rangle_{\Theta} \tag{2.22}$$

$$\bar{\mathbf{L}} := \left\langle \mathbf{L}\left(\mathbf{y}\right) : \mathbf{A}\left(\mathbf{y}\right)\right\rangle_{\Theta} \tag{2.23}$$

in which, $\bar{\mathbf{L}}$ is the tensor of homogenized elastic moduli of the composite. The third order coefficient tensor, $\mathbf{Z}^{(\alpha)}$ provides the stress contribution due to the separation coefficient, $\boldsymbol{\delta}^{(\alpha)}$.

2.2.3 Regularization for Mesh-size Objectivity

The macroscopic stress-strain relationship inevitably exhibits strain softening (i.e., loss of ellipticity). The unregularized formulations (or reduced-order model, i.e. including Eq. 2.11, 2.21) would cause mesh size sensitivity in the presence of failure localization because the amount of dissipation depends on macroscopic element size. This section proposes a regularization scheme bearing the resemblance to Gitman et al. [117]. Since RVE definition is terminated due to failure localization in the microstructure, the fracture energy can be adjusted by changing the size of microstructure domain, as the microcrack density is changed in view of microstructure periodicity. Thus, the energetic consistency can be achieved by altering the microstructure size as a function of macroscopic

element size. The size adjustment can be done in an *effective* manner, meaning an analytical equivalency relationship is established between the reduced order model and macroscopic element size by scaling the coefficient tensors, rather than numerically computing a separate reduced order model for every macroscopic element with a different size. The "reference" microstructure is the only one which is discretized for computing the coefficient tensors (i.e. reference coefficient tensors). Also, it is important to note that the analytical relations assumes linear or near-linear softening behavior (e.g., bilinear law [116]) in cohesive softening.

Let $\xi^{(\alpha)} = l/h^{(\alpha)}$ denote the length scale ratio, where l stands for the reference microstructure size (e.g., smallest RVE or unit cell) and $h^{(\alpha)}$ the characteristic length of the macroscale element, which can be evaluated by Govindjee's expression [118] along the normal direction of a failure path. The reduced order model associated with the length scale ratio, $\xi^{(\alpha)}$ is then obtained by scaling the reference coefficient tensors:

$$\hat{\mathbf{D}}^{(\alpha\beta)}\left(\xi^{(\alpha)}\right) = \boldsymbol{\eta}^{(\alpha)}\left(\xi^{(\alpha)}\right) \cdot \mathbf{D}^{(\alpha\beta)} \tag{2.24}$$

When expressed in terms of the local coordinate systems aligned with the unit normals and two tangential directions of the failure paths, the matrix form of the scaling tensor is diagonal:

$$\left[\boldsymbol{\eta}^{(\alpha)}\left(\xi^{(\alpha)}\right)\right] = \begin{bmatrix} \eta_N^{(\alpha)}(\xi^{(\alpha)}) & 0 & 0 \\ 0 & \eta_{S_1}^{(\alpha)}(\xi^{(\alpha)}) & 0 \\ 0 & 0 & \eta_{S_2}^{(\alpha)}(\xi^{(\alpha)}) \end{bmatrix} \tag{2.25}$$

Scaled $\widetilde{\mathbf{Z}}^{(\alpha)}\left(\xi^{(\alpha)}\right)$ is defined in the matrix form as:

$$\left[\hat{\mathbf{Z}}^{(\alpha)}\left(\xi^{(\alpha)}\right)\right] = \begin{bmatrix} \eta_N^{(\alpha)}\mathbf{Z}_{11}^{(\alpha)} & \eta_{S_1}^{(\alpha)}\mathbf{Z}_{12}^{(\alpha)} & \eta_{S_2}^{(\alpha)}\mathbf{Z}_{13}^{(\alpha)} \\ \eta_{S_1}^{(\alpha)}\mathbf{Z}_{12}^{(\alpha)} & \mathbf{Z}_{22}^{(\alpha)} & \mathbf{Z}_{23}^{(\alpha)} \\ \eta_{S_2}^{(\alpha)}\mathbf{Z}_{13}^{(\alpha)} & \mathbf{Z}_{23}^{(\alpha)} & \mathbf{Z}_{33}^{(\alpha)} \end{bmatrix} \tag{2.26}$$

$\mathbf{D}^{(\alpha\beta)}$ and $\mathbf{Z}^{(\alpha)}$ are the reference coefficient tensors, taken as $\mathbf{D}^{(\alpha\beta)}\left(\xi^{(\alpha)}\right) = \hat{\mathbf{D}}^{(\alpha\beta)}\left(\xi^{(\alpha)} = 1\right)$ and $\mathbf{Z}^{(\alpha)} = \hat{\mathbf{Z}}^{(\alpha)}\ (\xi^{(\alpha)} = 1)$, when the size of the reference microstructure equals the macroscopic element size. $\eta_N^{(\alpha)}$, $\eta_{S_1}^{(\alpha)}$ and $\eta_{S_2}^{(\alpha)}$ are respectively the scaling factors that are computed using coeffi-

cient tensor components in the normal and two orthogonal shear directions of the failure path:

$$\eta_N^{(\alpha)} = \frac{\xi^{(\alpha)} A_N^{(\alpha)}}{A_N^{(\alpha)} + \left(1-\xi^{(\alpha)}\right)\left(D_N^{(\alpha)} \bar{L}_N^{(\alpha)} + Z_N^{(\alpha)} C_N^{(\alpha)}\right)(\bar{L}_N^{(\alpha)})^{-1}} \tag{2.27}$$

$$\eta_{S_1}^{(\alpha)} = \frac{\xi^{(\alpha)} A_{S_1}^{(\alpha)}}{A_{S_1}^{(\alpha)} + \left(1-\xi^{(\alpha)}\right)\left(D_{S_1}^{(\alpha)} \bar{L}_{S_1}^{(\alpha)} + Z_{S_1}^{(\alpha)} C_{S_1}^{(\alpha)}\right)(\bar{L}_{S_1}^{(\alpha)})^{-1}} \tag{2.28}$$

$$\eta_{S_2}^{(\alpha)} = \frac{\xi^{(\alpha)} A_{S_2}^{(\alpha)}}{A_{S_2}^{(\alpha)} + \left(1-\xi^{(\alpha)}\right)\left(D_{S_2}^{(\alpha)} \bar{L}_{S_2}^{(\alpha)} + Z_{S_2}^{(\alpha)} C_{S_2}^{(\alpha)}\right)(\bar{L}_{S_2}^{(\alpha)})^{-1}} \tag{2.29}$$

where $A_N^{(\alpha)}$, $A_{S_1}^{(\alpha)}$ and $A_{S_2}^{(\alpha)}$ stand for the softening slopes of the traction-separation relationship, defined as $A_N^{(\alpha)} = \partial t_N^{(\alpha)} / \partial \delta_N^{(\alpha)}$, $A_{S_1}^{(\alpha)} = \partial t_{S_1}^{(\alpha)} / \partial \delta_{S_1}^{(\alpha)}$, $A_{S_2}^{(\alpha)} = \partial t_{S_2}^{(\alpha)} / \partial \delta_{S_2}^{(\alpha)}$. t_N, t_{S_1}, t_{S_2} and δ_N, δ_{S_1}, δ_{S_2} are respectively normal and two tangential components of the traction and separation vectors. $D_N^{(\alpha)}$, $D_{S_1}^{(\alpha)}$, $D_{S_2}^{(\alpha)}$, $C_N^{(\alpha)}$, $C_{S_1}^{(\alpha)}$, $C_{S_2}^{(\alpha)}$, $\bar{L}_N^{(\alpha)}$, $\bar{L}_{S_1}^{(\alpha)}$, $\bar{L}_{S_2}^{(\alpha)}$ are respectively linear compositions of the coefficient tensor components in terms of the aforementioned local coordinates of the failure path. The detailed derivation of coefficient tensor scaling is provided in the Appendix.

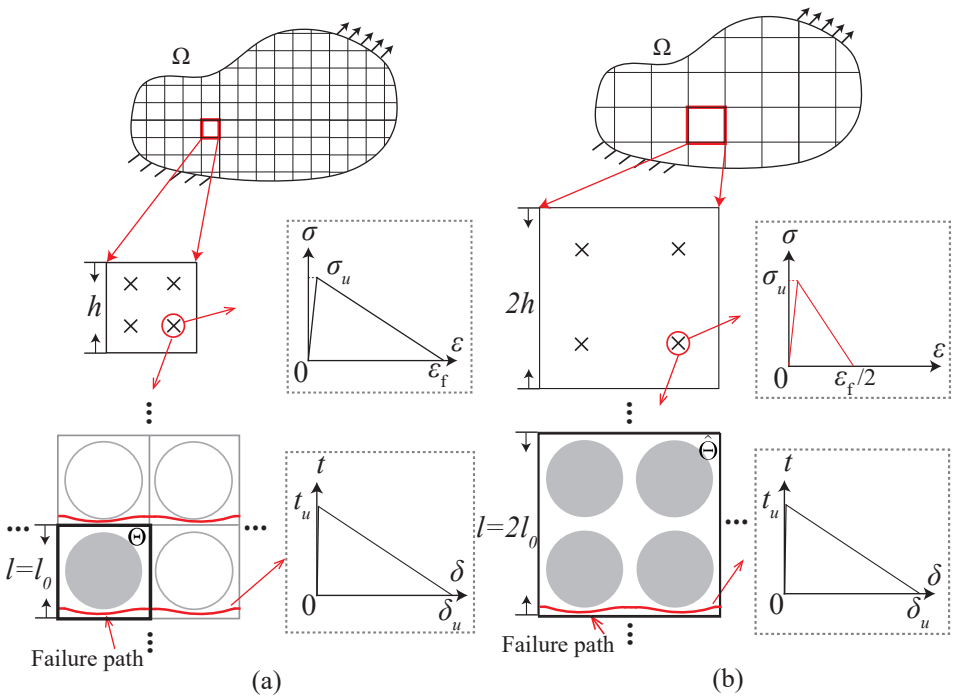

Figure 2.2: Regularization strategy for mesh-size objectivity. (a) Macroscopic stress-strain relationship and cohesive behavior (i.e. traction-separation curve) when characteristic element size is h, (b) when characteristic element size is set to $2h$ using a larger microstructure which leads to less microcrack density.

The regularization methodology is schematically illustrated in Fig. 2.2. Unlike the crack band approach [119], which also employs the strategy of energy consistency, the constitutive (i.e., traction-separation) behavior remains unchanged in the present approach. The microstructure size (i.e., the corresponding MDDT model) is adjusted instead to regularize dissipated energy within the microstructure. The softening slope of the resulting macroscopic stress-strain relationship varies as a function of the length scale parameter.

One consideration is the relationship between the size of the microstructure, physical observable within the localization band and the macroscopic mesh size. Let w and ρ, respectively denote the width of the localization band and the microcrack density within the band. l_0 denotes the size of the smallest microstructure that can represent the morphology (e.g., a single fiber unit cell in Fig. 2.2) with a single failure path, and $h = aw$ the size of the macroscopic element along the direction normal to the failure path. a is a constant that sets the macroscopic element size relative to localization band width w. Using the energy equivalence principle, the microcrack density within the localizing element must be set as: $\rho_h = \rho/a$. Noting that the microcrack density within the element is inversely proportional to the microstructure size, l, and defining $\rho_0 = 1/l_0$ as the crack density associated with the unit cell, we obtain:

$$\frac{l}{l_0} = \frac{\rho_0 h}{\rho w} \tag{2.30}$$

The reference reduced order model is typically chosen to be the smallest representative volume or the unit cell that describes the microstructural geometry (i.e., $l = l_0$), and the corresponding macroscopic element size is expressed as: $h = \rho w l_0$.

2.2.4 Residual Stiffness Correction

Eigenstrain-based homogenization models have been shown to exhibit spurious post-failure residual stiffness, particularly when low order models are employed [120]. The inaccurate response enables the macroscopic element to retain some load carrying capacity after failure and alters load redistribution in a failure propagation scenario. In this chapter, the issue of post-failure residual stiffness is alleviated by extending the idea of coefficient tensor scaling. The coefficient tensor $\mathbf{Z}$ in macroscopic stress-strain relationship is regularized with scaling factor η^r. By enforcing the

residual stiffness under a small amount, η^r under mode-I (denoted by η_N^r) is expressed as:

$$\eta_N^r = -(1 - k_N^r)\frac{D_N^{(\alpha)}\bar{L}^{(\alpha)}}{Z_N^{(\alpha)}C_N^{(\alpha)}} + k_N^r \tag{2.31}$$

where k_N^r is the correction factor for residual stiffness in mode-I, equals to the ratio of corrected residual stiffness and original stiffness. Eq. 2.31 under mode-II is expressed in the similar form.

2.3 Numerical Implementation

The overall strategy for the numerical implementation for MDDT model consists of the construction of the reduced order microstructure model at the *pre-processing* stage, and the evaluation of the macroscopic problem. The pre-processing stage consists of the following steps: (1) Characterization and discretization of the material microstructure; (2) Identification of crack morphologies to be included in the reduced order model; (3) Evaluation of microstructure problems to compute the influence functions, and numerical integrations to compute the coefficient tensors; (4) Identification of the size scale ratios and scaling the coefficient tensors for mesh size and residual stiffness. In this chapter, smallest unit cell morphology is employed, and the crack morphologies embedded in the unit cell is identified based on set of expected failure modes (e.g., transverse matrix crack, fiber fracture) that the macroscopic structure is expected to undergo. The evaluation of the elastic and separation influence functions follow the procedures outlined in Ref. [51] and skipped herein for brevity.

2.3.1 Cohesive Law and Mode Mixity

The cohesive behavior within the failure path is expressed using a simple constitutive relationship as a function of an isotropic damage variable:

$$\mathbf{t}^{(\alpha)} = (1 - \omega^{(\alpha)})\mathbf{K}^{(\alpha)} \cdot \boldsymbol{\delta}^{(\alpha)} \tag{2.32}$$

where $\omega^{(\alpha)} \in [0, 1]$ is the damage variable in the failure path, α. $\omega^{(\alpha)}$ is a scalar state variable with $\omega^{(\alpha)} = 0$ and $\omega^{(\alpha)} = 1$, respectively denote the state of no damage and a cohesionless crack along the failure path, respectively. $\mathbf{K}^{(\alpha)}$ is the tensor of cohesive stiffnesses, a second order tensor that is diagonal when expressed in the local basis aligned with the unit normal to the failure path, $\mathbf{n}^{(\alpha)}$,

expressed in Eq. 2.19.

Damage evolution is expressed as a monotonically increasing function of the history variable, $\kappa^{(\beta)}$ as:

$$\omega^{(\beta)} = \Phi\left(\kappa^{(\beta)}\right) \tag{2.33}$$

where,

$$\kappa^{(\beta)} = \max_{\tau\in[0,t]}\left\{\left\langle \nu^{(\beta)}(\tau) - \nu_0^{(\beta)}\right\rangle_+\right\} \tag{2.34}$$

in which, $\nu^{(\beta)}(\tau)$ and $\nu_0^{(\beta)}$ are the damage equivalent separation and the initial damage equivalent separation, respectively. $\nu_0^{(\beta)}$ is a parameter that indicates damage initiation (i.e., the value of $\nu^{(\beta)}(\tau)$ below which damage does not evolve). $\langle\cdot\rangle_+$ represents the Macaulay bracket expressed as $\langle\cdot\rangle_+ = [(\cdot)+|\cdot|]/2$. Damage equivalent separation can be expressed as a function of the components of the separation coefficients:

$$\nu^{(\beta)} = k_N^{(\beta)}\hat{\delta}_N^{(\beta)} + k_S^{(\beta)}\sqrt{\left(\hat{\delta}_{S_1}^{(\beta)}\right)^2 + \left(\hat{\delta}_{S_2}^{(\beta)}\right)^2} \tag{2.35}$$

in which, $[\hat{\boldsymbol{\delta}}^{(\beta)}] = [\hat{\delta}_N^{(\beta)}, \hat{\delta}_{S_1}^{(\beta)}, \hat{\delta}_{S_2}^{(\beta)}]$ is the separation vector and its components expressed along the basis aligned with the failure path normal (i.e., $\hat{\delta}_N^{(\beta)}$ is normal separation and $\hat{\delta}_{S_i}^{(\beta)}$, $i = 1, 2$ are tangential separation components). Expressed in terms of the same basis, the tensor of cohesive stiffnesses become:

$$[\mathbf{K}^{(\beta)}] = \begin{bmatrix} k_N^{(\beta)} & 0 & 0 \\ 0 & k_S^{(\beta)} & 0 \\ 0 & 0 & k_S^{(\beta)} \end{bmatrix} \tag{2.36}$$

k_N and k_S are the normal and tangential stiffnesses, respectively.

The damage evolution in the failure path as a function of the history variable has the form:

$$\Phi\left(\kappa^{(\beta)}\right) = \begin{cases} \dfrac{1}{\alpha_2^{(\beta)}}\arctan\left(\alpha_1^{(\beta)}\kappa^{(\beta)}\right) & \text{if } \kappa^{(\beta)} \leq \dfrac{\tan(\alpha_2^{(\beta)})}{\alpha_1^{(\beta)}} \\ 1 & \text{otherwise} \end{cases} \tag{2.37}$$

In the numerical implementation, the presence of Macaulay bracket in Eq. 2.34 introduces a discontinuity and results in lack of convergence in some cases. In order to improve convergence

of the nonlinear evaluation of the system, we replace the Macaulay bracket with a C^1 continuous approximation, which introduces continuity by the addition of a small arc with radius r at the elbow of the ramp (i.e., Macaulay) function (see Ref. [24]):

$$\langle x \rangle_c = \begin{cases} 0 & x < -\tan^{-1}(3\pi r/8) \\ r - \sqrt{r^2 - [x + \tan^{-1}(3\pi r/8)]^2} & -\tan^{-1}(3\pi r/8) \leq x \leq \dfrac{\tan^{-1}(3\pi r/8)}{\sqrt{2}} \\ x & x > \dfrac{\tan^{-1}(3\pi r/8)}{\sqrt{2}} \end{cases} \tag{2.38}$$

In the following numerical examples of this chapter, r is selected to be 8.5×10^{-4}.

2.3.2 Macroscopic Stress Update Procedure

Given: Homogenized strain ${}_t\bar{\boldsymbol{\epsilon}}$ and its increment $\Delta\bar{\boldsymbol{\epsilon}}$, separations in local coordinate system ${}_t\hat{\boldsymbol{\delta}}^{(\beta)}$ and damage variables ${}_t\omega^{(\beta)}$ of each failure path ($\beta = 1, 2, ..., m$). The left subscript denotes the incremental step, i.e., ${}_t(\cdot)$ and ${}_{t+\Delta t}(\cdot)$ stands for the variables at the previous and current increments, respectively. For simplicity, subscript ${}_{t+\Delta t}(\cdot)$ is omitted for simplicity.

Compute: The macroscopic stress $\bar{\boldsymbol{\sigma}}$; current separations $\hat{\boldsymbol{\delta}}^{(\beta)}$ and damage variables $\omega^{(\beta)}$ of each failure path.

In this section, the coefficient tensors and other tensors are expressed in matrix form following the Voigt notation. To obtain the separation vector $\hat{\boldsymbol{\delta}}^{(\beta)} = [\hat{\delta}_N^{(\beta)}, \hat{\delta}_{S_1}^{(\beta)}, \hat{\delta}_{S_2}^{(\beta)}]$, the governing equations of the reduced order model are solved using the Newton-Raphson method. A penalty term is added to enforce contact constraint along the failure paths under compression. The general form of the resulting nonlinear system is given as:

$$\boldsymbol{\Psi} = \mathbf{M}(\mathbf{d})\mathbf{d} + \mathbf{f}(\bar{\boldsymbol{\epsilon}}) + \mathbf{f}^c(\mathbf{d}) = \mathbf{0} \tag{2.39}$$

where $\mathbf{f}$ is the force vector, $\mathbf{f}^c$ is the penalty function, $\mathbf{d}$ is the state variable vector constituted by

the separation vectors: $\mathbf{d} = [\hat{\boldsymbol{\delta}}^{(1)}, \hat{\boldsymbol{\delta}}^{(2)}, ...\hat{\boldsymbol{\delta}}^{(m)}]^{\mathrm{T}}$. Based on Eq. 2.14, $\mathbf{M}$ is defined as:

$$\mathbf{M} = \begin{bmatrix} (1-\omega^{(1)})\mathbf{K}^{(1)} + \mathbf{D}^{(11)} & \mathbf{D}^{(12)} & \cdots & \mathbf{D}^{(1m)} \\ \mathbf{D}^{(21)} & (1-\omega^{(2)})\mathbf{K}^{(2)} + \mathbf{D}^{(22)} & \cdots & \mathbf{D}^{(2m)} \\ \vdots & \vdots & \ddots & \vdots \\ \mathbf{D}^{(m1)} & \mathbf{D}^{(m2)} & \cdots & (1-\omega^{(m)})\mathbf{K}^{(m)} + \mathbf{D}^{(mm)} \end{bmatrix} \tag{2.40}$$

where $\mathbf{K}^{(\beta)}$ represents cohesive stiffnesses and the matrix form of the coefficient tensor is stated as $\mathbf{D}^{(\alpha\beta)} = [D_{ij}^{(\alpha\beta)}]; i, j = 1, 2, 3$. The damage variable $\omega^{(\beta)}$ is computed using the damage evolution equations in terms of the corresponding separation $\hat{\boldsymbol{\delta}}^{(\beta)}$.

The force vector, $\mathbf{f}(\bar{\boldsymbol{\epsilon}})$ is given as:

$$\mathbf{f} = [\mathbf{C}^{(1)}; \mathbf{C}^{(2)}; ...\mathbf{C}^{(m)}]\bar{\boldsymbol{\epsilon}} \tag{2.41}$$

in which, semicolon indicates column matrix construction, and the components of the homogenized strain vector is expressed in the Voigt form: $\bar{\boldsymbol{\epsilon}} = [\hat{\epsilon}_{11}, \hat{\epsilon}_{22}, \hat{\epsilon}_{33}, \hat{\epsilon}_{12}, \hat{\epsilon}_{13}, \hat{\epsilon}_{23}]^{\mathrm{T}}$.

The penalty function $\mathbf{f}^c(\mathbf{d})$ to enforce the unilateral contact constraint is given as:

$$\mathbf{f}^c = \frac{1}{\chi}[\langle\delta_N^{(1)}\rangle_-, 0, 0, \langle\delta_N^{(2)}\rangle_-, 0, 0, ...\langle\delta_N^{(m)}\rangle_-, 0, 0]^{\mathrm{T}} \tag{2.42}$$

where $\chi \ll 1$ is the penalty parameter, and $\langle\cdot\rangle_-$ is defined as $\langle\cdot\rangle_- = [|\cdot| - (\cdot)]/2$.

Based on the definitions above, the solution procedure for the nonlinear system consists of the following steps:

1. Update the homogenized strain: $\bar{\boldsymbol{\epsilon}} = {}_t\bar{\boldsymbol{\epsilon}} + \Delta\bar{\boldsymbol{\epsilon}}$;
2. Initialize the unknown coefficients: ${}^0\mathbf{d} = {}_t\mathbf{d}$;
3. Loop until convergence;
   - 3a. Compute the system residual: ${}^k\partial\boldsymbol{\Psi}({}^k\mathbf{d})$;
   - 3b. Check convergence: $\| {}^k\partial\boldsymbol{\Psi} \| \leq tol$;
   - 3c. If convergence: Exit loop;
   - 3d. Compute system Jacobian: ${}^k(\partial\boldsymbol{\Psi}/\partial\mathbf{d})$;
   - 3e. Update unknown coefficients: ${}^{k+1}\mathbf{d} = {}^k\mathbf{d} - {}^k(\partial\boldsymbol{\Psi}/\partial\mathbf{d})^{-1}\,{}^k\boldsymbol{\Psi}$;

3f. $k \leftarrow k+1$

4. Update the macroscopic stress $\bar{\boldsymbol{\sigma}}$ based on Eq. 2.21.

2.3.3 Macroscopic Tangent Moduli

A closed form expression for the macroscopic tangent moduli tensor is defined based on Eq. 2.21:

$$\mathscr{L} = \frac{\partial \bar{\boldsymbol{\sigma}}}{\partial \bar{\boldsymbol{\epsilon}}} = \bar{\mathbf{L}} + \sum_{\beta=1}^{m} \mathbf{Z}^{(\beta)} \frac{\partial \hat{\boldsymbol{\delta}}^{(\beta)}}{\partial \bar{\boldsymbol{\epsilon}}} \tag{2.43}$$

The derivative of the separation vector with respect to the homogenized strain is computed by leveraging Eq. 2.39 and expressing the residual as $(\mathbf{d}(\bar{\boldsymbol{\epsilon}}), \bar{\boldsymbol{\epsilon}})$:

$$\frac{\partial \mathbf{d}}{\partial \bar{\boldsymbol{\epsilon}}} = -\left[\frac{\partial \boldsymbol{\Psi}}{\partial \mathbf{d}}\right]^{-1} \frac{\partial \boldsymbol{\Psi}}{\partial \bar{\boldsymbol{\epsilon}}} \tag{2.44}$$

where,

$$\frac{\partial \boldsymbol{\Psi}}{\partial \bar{\boldsymbol{\epsilon}}} = [\mathbf{C}^{(1)}; \mathbf{C}^{(2)}; ...\mathbf{C}^{(m)}] \tag{2.45}$$

and

$$\frac{\partial \boldsymbol{\Psi}}{\partial \mathbf{d}} = \frac{\partial \mathbf{M}}{\partial \mathbf{d}}\mathbf{d} + \mathbf{M} + \frac{\partial \mathbf{f}^c}{\partial \mathbf{d}} \tag{2.46}$$

The derivative of penalty function is given as:

$$\frac{\partial \mathbf{f}^c}{\partial \mathbf{d}} = \frac{1}{2\chi}\begin{bmatrix} \boldsymbol{F}_c^{(1)} & \mathbf{0} & \cdots & \mathbf{0} \\ \mathbf{0} & \boldsymbol{F}_c^{(2)} & \cdots & \mathbf{0} \\ \vdots & \vdots & \ddots & \vdots \\ \mathbf{0} & \mathbf{0} & \cdots & \boldsymbol{F}_c^{(m)} \end{bmatrix}; \quad \boldsymbol{F}_c^{(\beta)} = \begin{bmatrix} 1-\mathrm{sgn}(\hat{\delta}_N^{(\beta)}) & 0 & 0 \\ 0 & 0 & 0 \\ 0 & 0 & 0 \end{bmatrix} \tag{2.47}$$

The derivative of $\mathbf{M}$ is calculated by:

$$\frac{\partial \mathbf{M}}{\partial \mathbf{d}} = \sum_{\beta=1}^{m} \frac{\partial \mathbf{M}}{\partial \omega^{(\beta)}} \frac{\partial \omega^{(\beta)}}{\partial \mathbf{d}} \tag{2.48}$$

in which the only nonzero components are $-\mathbf{K}^{(\beta)}$ and $\partial\omega^{(\beta)}/\partial\hat{\boldsymbol{\delta}}^{(\beta)}$, respectively. The derivative of

damage $\omega^{(\beta)}$ can be expanded through the damage evolution equations by the chain rule:

$$\frac{\partial \omega^{(\beta)}}{\partial \hat{\boldsymbol{\delta}}^{(\beta)}} = \frac{\partial \omega^{(\beta)}}{\partial \kappa^{(\beta)}} \frac{\partial \kappa^{(\beta)}}{\partial \nu^{(\beta)}} \frac{\partial \nu^{(\beta)}}{\partial \hat{\boldsymbol{\delta}}^{(\beta)}} = \frac{\alpha_1 H_c(\Delta\nu^{(\beta)})}{\alpha_2[1+(\alpha_1\kappa^{(\beta)})^2]} \left[k_N^{(\beta)}, k_S^{(\beta)} \frac{\hat{\delta}_{S_1}^{(\beta)}}{\|\hat{\boldsymbol{\delta}}_S^{(\beta)}\|}, k_S^{(\beta)} \frac{\hat{\delta}_{S_2}^{(\beta)}}{\|\hat{\boldsymbol{\delta}}_S^{(\beta)}\|} \right]^{\mathrm{T}}$$

where $\Delta\nu^{(\beta)}$ stands for the increment of equivalent separation ${}^{k}\nu^{(\beta)} - {}_{t}\nu^{(\beta)}$, $\|\hat{\boldsymbol{\delta}}_S^{(\beta)}\| = \sqrt{\left(\hat{\delta}_{S_1}^{(\beta)}\right)^2 + \left(\hat{\delta}_{S_2}^{(\beta)}\right)^2}$, the function H_c is the derivative of the modified Macaulay bracket in Eq. 2.38:

$$H_c(x) = \begin{cases} 0 & x < -\tan^{-1}(3\pi r/8) \\ \dfrac{x + \tan^{-1}(3\pi r/8)}{\sqrt{r^2 - [x + \tan^{-1}(3\pi r/8)]^2}} & -\tan^{-1}(3\pi r/8) \le x \le \dfrac{\tan^{-1}(3\pi r/8)}{\sqrt{2}} \\ 1 & x > \dfrac{\tan^{-1}(3\pi r/8)}{\sqrt{2}} \end{cases} \tag{2.49}$$

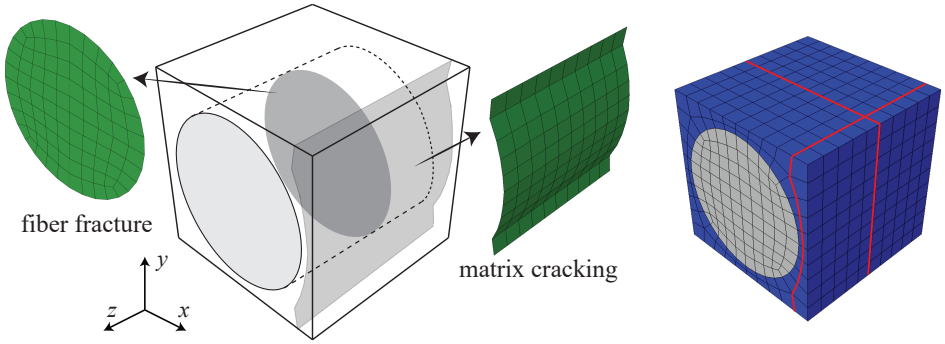

Figure 2.3: Microstructure configuration with failure paths of "transversely matrix cracking" and "fiber fracture".

2.4 Numerical Verification

2.4.1 Unnotched Lamina Analyses

The performance of MDDT model is firstly assessed in the context of uniformly loaded specimens, which corresponds to the behavior of an unnotched lamina. Figure 2.3 shows the microstructural configuration and the failure paths employed in the analysis. The unit cell is a unidirectional fiber-reinforced matrix with 65% fiber volume fraction. Two failure paths are considered ($m = 2$). The "transverse matrix cracking" path resides within the domain of the matrix material, whereas the "fiber fracture" path is within the domain of the fiber material. The matrix cracking and fiber frac-

ture paths are approximate planes with normals along x and z directions, respectively as indicated in Fig. 2.3. These two failure paths correspond to two of the primary failure modes observed in laminated fiber reinforced composites subjected to tension loading. In case of failure under uniaxial loading along the z direction, the unit cell is expected to undergo failure by fiber fracture as well as the fracture within the matrix ligament. Under this loading condition, the matrix ligament failure is expected to immediately follow or simultaneously occur with fiber fracture, but it is ignored in this chapter in view of the high disparity between the fiber and matrix moduli, and due to the brittle nature of the fracture process along the fiber direction. In long fiber composites, the path of a transverse matrix crack often follows fiber-matrix interfaces as well. Inclusion of such a path requires defining the interface strength and failure parameters which are not straightforward using traditional experimental characterization techniques. For purposes of model verification, the path of the transverse matrix cracking mode is taken to go through the matrix phase only.

The elastic and fracture parameters for matrix and fiber employed in the numerical examples are summarized in Table 3.1. The mode I cohesive strength and energies are 4.87 GPa and 48.72 MPa-mm for fiber fracture, and 84.86 MPa and 4.24 MPa-mm for transverse matrix cracking. The mode II fracture properties are considered to be the same as mode I in this section. Fracture energies employed in this section are relatively large to exacerbate the quasi-brittle behavior and the softening stage, in order to clearly demonstrate mesh size objectivity.

Table 2.1: Model parameters for matrix and fiber

Matrix Properties (isotropic)							
E [GPa]		ν		α_1[MPa^{-1}]	α_2[rad]		K [MPa]
3.55		0.35		8×10^{-3}	1.57		10^9
Fiber Properties (transversely isotropic)							
E_1 [GPa]	E_2 [GPa]	G_{12}[GPa]	ν_{12}	ν_{23}	α_1[MPa^{-1}]	α_2[rad]	K [MPa]
263.00	13.00	27.50	0.32	0.20	1.3×10^{-4}	1.57	10^{10}

2.4.1.1 Mesh Size Objectivity

Figure 2.4 displays the geometry, loading and boundary conditions of the macroscopic domain. The macroscopic specimen is subjected to displacement-controlled loading until failure. In Fig. 2.4a and 2.4c, the configurations are perpendicular to the failure paths under uniaxial tension condition

resulting in mode I fracture within the matrix and fiber, respectively. Symmetry boundary conditions are applied to the three sides normal to x,y and z directions. The configuration in Fig. 2.4b is a simple shear test, in which mesh size sensitivity is studied under mode II fracture conditions. This is achieved by suppressing the possibility of the onset of mode I dominated fracture through the use of single failure path parallel to the shear loading. The inclusion of a failure path oriented at 45 degree angle to the shear loading would enable mode I fracture under simple shear. In order to ensure damage localization in the examples, the properties in one layer of elements along the expected fracture surface (illustrated as dark regions in Fig. 2.4) have been slightly perturbed. The macroscale domain is discretized using four different element sizes (denoted as h) of 1 mm, 0.5 mm, 0.25 mm, 0.125mm. 8-noded tri-linear hexahedral elements with reduced integration (1 quadrature point per element) and hourglass control are employed in the macroscale discretizations.

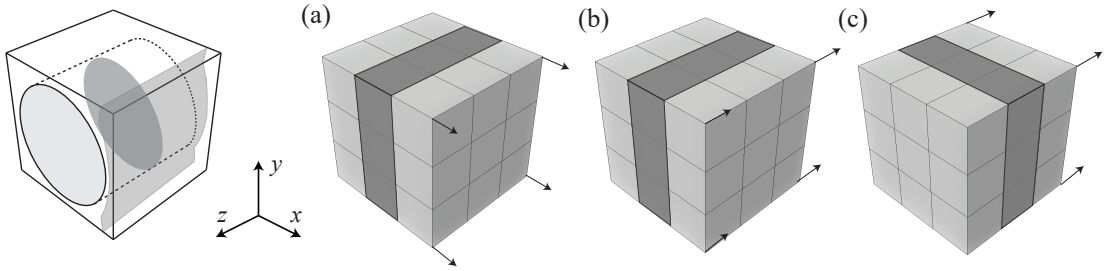

Figure 2.4: Geometry and loading conditions for the unnotched specimen under (a) matrix cracking dominated mode I condition, (b) matrix cracking dominated mode II condition, (c) fiber fracture dominated mode I condition.

Figures 2.5a-c show the macroscopic stress-strain curves, along with the evolution the critical cohesive damage variable (i.e., $\omega^{(m)}$ or $\omega^{(f)}$) in the localization zones for the three loading configurations shown in Fig. 2.5. The first two loading configurations result in failure completely dominated by transverse matrix cracking, whereas the last configuration results in fiber fracture dominated failure. In all cases, no appreciable damage accumulation is observed in the non-dominant failure path. The stress-strain curves for the four discretizations are nearly overlapping and the overall softening stiffness in the specimen stays the same regardless of the mesh size in both matrix cracking and fiber fracture dominated cases. In all cases, the macroscopic stress (along with the traction along the dominant failure path within the unit cell) reaches its peak when the cohesive damage variable of the dominant failure path reaches a value slightly lower than unity. Macroscopic stress (and traction along the failure path) vanishes when damage value reaches unity. Figure 2.5d illustrates the

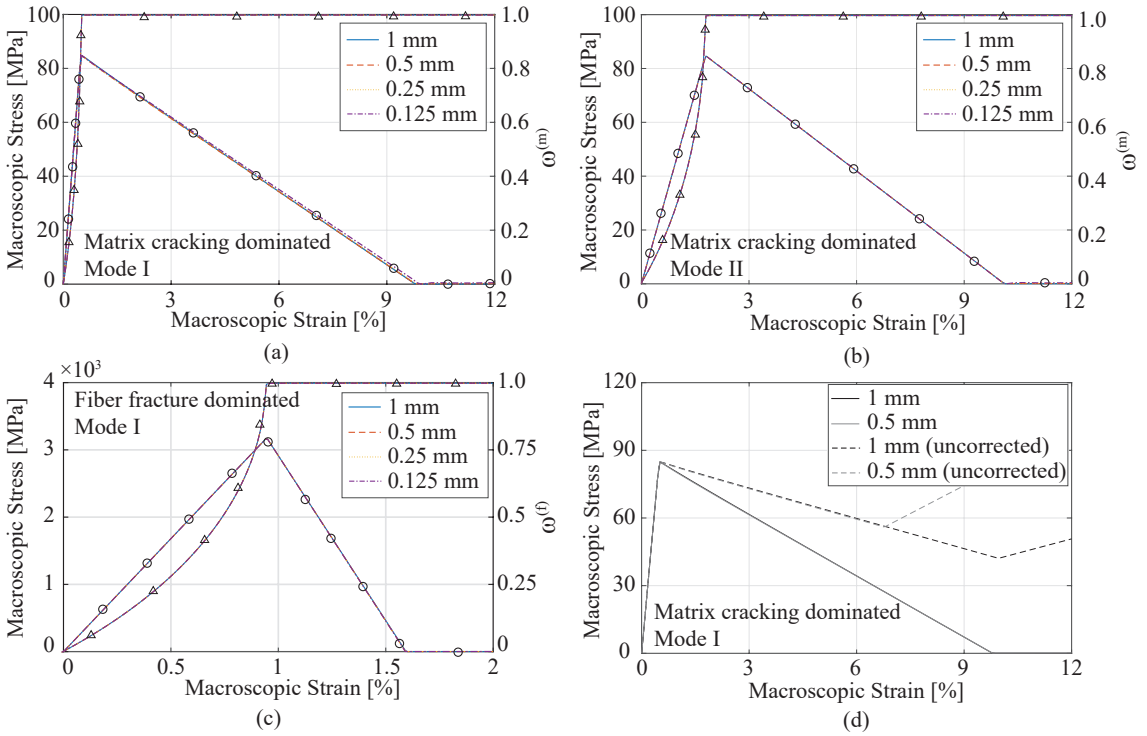

Figure 2.5: The macroscopic stress-strain curves (denoted by circle mark) and damage evolution (denoted by triangle mark) of unnotched specimen with element size of h=1 mm, 0.5 mm, 0.25 mm, 0.125 mm under (a) matrix cracking dominated mode I condition, (b) matrix cracking dominated mode II condition, (c) fiber fracture dominated mode I condition, (d) matrix cracking dominated mode I with and without residual stiffness correction.

impact of the residual stiffness correction on the resulting macroscopic stress-strain curves. The figure compares those predicted by the $h = 1$mm and $h = 0.5$mm simulations for matrix dominated failure under uniaxial loading (Fig. 2.4a). In the absence of residual stiffness correction, a significant residual stiffness is predicted, which gets larger as the mesh is refined. The proposed correction eliminates this spurious effect.

In Fig. 2.6, mesh size insensitivity of the proposed formulation has been demonstrated for unit cells with different fiber volume fractions subjected to matrix dominated failure under mode I loading as shown in Fig. 2.4a. Three unit cells with fiber volume fractions of 55%, 60% and 65% were considered. The simulations demonstrate that the behavior is mesh size independent for all values of fiber volume fraction. Only small discrepancies have been observed between the specimens with different fiber volume fractions. The macroscopic stiffnesses are 7.85 GPa, 8.28 GPa, and 8.73 GPa for 55%, 60% and 65% configurations, respectively. The ultimate macroscopic strengths and strains

to failure are largely unaffected by the fiber volume fractions within the range of values considered. This is because the failure is dictated by the matrix properties, and the overall traction state that the matrix failure path undergoes is not significantly affected by the change in the fiber volume fraction.

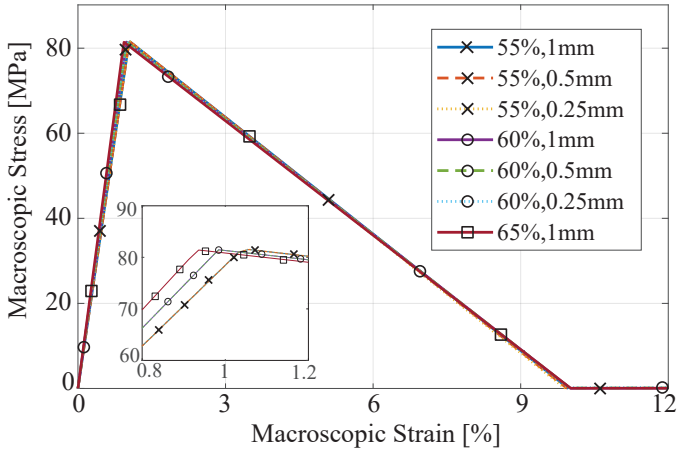

Figure 2.6: The macroscopic stress-strain curves for unit cells with different fiber volume fractions.

The proposed model has been verified by comparing the model predictions with direct numerical simulations of fully resolved microstructure. Abaqus in-built cohesive zone model (CZM) is employed as the reference. The unnotched specimen with the same geometry and failure path conditions is considered. The finite element mesh of the unit cell and the failure path modeled using cohesive zone elements are shown in Fig. 2.7. COH3D8 elements from the Abaqus cohesive element library were used. Maximum nominal stress criterion for damage initiation and linear energy-based damage evolution are employed for traction-separation response of the cohesive element. The stress-strain curves obtained under mode I and II conditions compared with the MDDT model are shown in Fig. 2.7. A good overall agreement is observed between the two methods. Damage contours of the cohesive interface demonstrate spatially non-uniform damage evolution. Before reaching the ultimate stress, damage evolves more rapidly in regions closer to the fiber and propagates outward. The MDDT model approximates spatial evolution of damage as uniform within the failure path. The discrepancies between the reference and proposed models near the peak strength are attributed to this approximation.

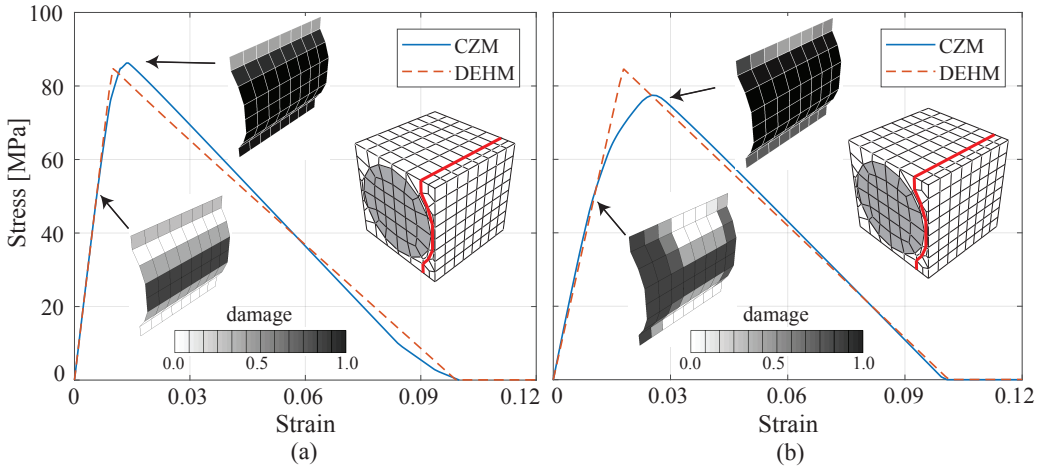

Figure 2.7: Stress-strain curves predicted by the reference and the proposed approaches, under (a) Mode I condition, and (b) Mode II conditions. Inset contours indicate damage within the cohesive interface.

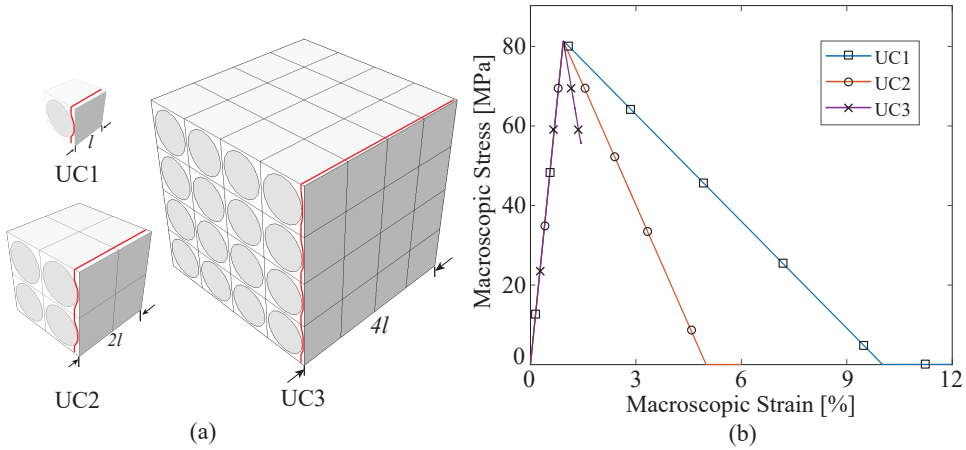

Figure 2.8: (a) Unit cells with different sizes and microcrack densities, and (b) the corresponding macroscale stress-strain curves.

2.4.1.2 Effect of Unit Cell Size and Microcrack Density

The role of using unit cells with different sizes on the overall macroscopic response is investigated using the unnotched specimen configuration under mode I loading shown in Fig. 2.4a. Three unit cells (named UC1, UC2 and UC3) shown in Fig. 2.8a are considered. UC1 is the single fiber square unit cell employed in the verification studies above, whereas UC2 and UC3 are generated by tiling UC1 twice and four times along all directions, respectively. All unit cells consider a single transverse matrix failure path. While the geometric attributes of all three unit cells are identical, the microcrack densities they represent are different. Simulations are performed using $h = 1$ mm over

the same macroscale domain (Fig. 2.4a). ROMs for the unit cells were not regularized to ensure that the crack spacing is not adjusted based on the size scale ratio. The stress-strain curves for the three unit cells are compared in Fig. 2.8b. The pre-peak response as well as the peak strength predicted by the three configurations are identical since the behavior is controlled by the geometric attributes of the unit cells in this regime. In the softening regime, the stress-strain response becomes progressively more brittle with increasing unit cell size. This is because, the smaller microstructure with larger crack density dissipates more energy compared with larger microstructures with wider microcrack spacing via progressive loss of cohesion along the microcracks.

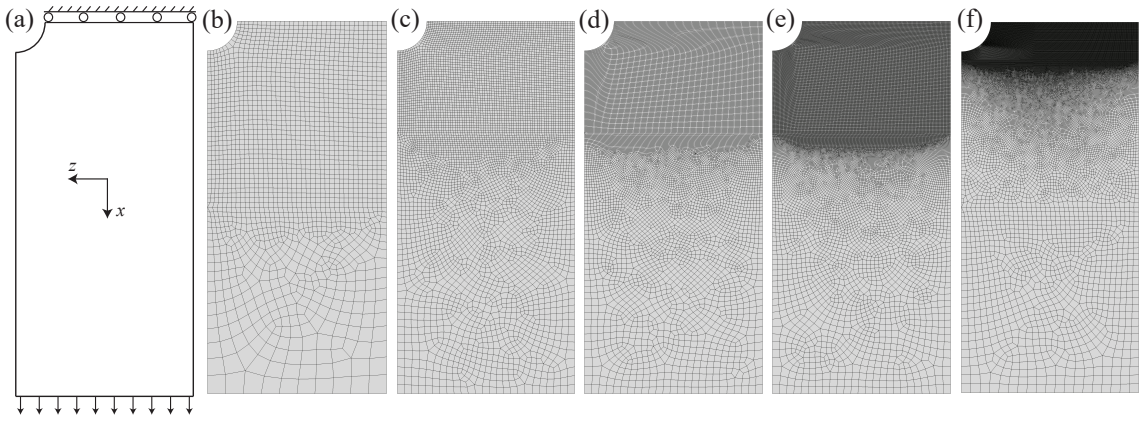

Figure 2.9: (a) Geometry, loading and boundary conditions for open-hole configuration. Mesh discretizations of (b) h=0.5 mm, (c) h=0.25 mm, (d) h=0.0625 mm, (e) h=0.03125 mm.

2.4.2 Open-hole Laminate Analysis

The capabilities of the MDDT approach are further assessed using two open-hole laminated composite configurations. Figure 2.9a shows the geometry, loading and boundary conditions of a 90° (i.e., the fibers are oriented along the z-direction) single-ply lamina specimen. The reduced order model shown in Fig. 2.3 that includes matrix cracking and fiber fracture paths is employed in this section. The overall dimensions of the specimen are 38mm, 80mm and 0.125mm in width, length and thickness, respectively. The radius of the hole is 3.175mm. Symmetry boundary conditions are applied at the three sides and 1/8 of the specimen is modeled. The domain is subjected to displacement-controlled uniaxial tension loading. The model parameters and the corresponding fracture properties for the fiber and matrix materials are shown in Table 2.2. The resulting mode I cohesive strength and energies for fiber fracture are 3.97 GPa and 12.57 MPa-mm, and for trans-

verse matrix cracking are 84.75 MPa and 0.27 MPa-mm. The values for the strength of the fiber, and the strength and fracture energy of the matrix are generally consistent with generic unidirectionally carbon fiber reinforced thermoset composites. While the fracture energy for the fiber is not easy to obtain experimentally and generally considered purely brittle, new experimental studies point to quasi-brittle behavior for fiber as well (see Ref. [121]). Under the applied loading and geometry conditions, fracture in the specimen is expected to initiate near the hole in the form of matrix cracking and propagate as mode I dominated fracture. In order to ensure that the mesh alignment does not impede crack propagation, the domain of the specimen around the notch is discretized using structured meshes aligned with the fiber direction. The sizes of h=0.5mm, 0.25mm, 0.125mm, 0.0625mm, and 0.03125mm are used in the structured portion of the mesh (see Fig. 2.9b-f). For all the meshes, there is single element discretization per ply in the thickness direction.

Table 2.2: Fracture process parameters used in the open-hole simulations

Matrix Failure						
G_{Ic}	G_{IIc}	t_{ult}	α_1	α_2	K_I	K_{II}
[MPa mm]	[MPa mm]	[MPa]	[MPa^{-1}]	[rad]	[MPa]	[MPa]
0.27	0.98	84.75	7.5×10^{-3}	1.57	10^5	2.8×10^8
Fiber Failure						
G_{Ic}	G_{IIc}	t_{ult}	α_1	α_2	K_I	K_{II}
[MPa mm]	[MPa mm]	[MPa]	[MPa^{-1}]	[rad]	[MPa]	[MPa]
12.57	12.57	3967.82	1.6×10^{-4}	1.57	10^{10}	10^{10}

Figure 2.10 compares the transverse matrix damage contours and crack propagation paths predicted using three different discretizations (h=0.25mm, 0.125mm, 0.0625mm) at the exact same stage of the loading process. The other two discretizations show the same pattern of response. In the figure, the crack is displayed by removing the elements which have reached complete damage state ($\omega^{(m)} = 1$) during the post processing stage. Element erosion is not employed in the simulations. The damage contours show that damage nucleates at the brim of the hole, followed by the crack initiation and extension along the fiber direction. The simulation results show that a damage process zone forms near the notch followed by rapid propagation of the transverse matrix crack. Both the process zone as well as the crack propagation are independent of the element size employed in the discretization. Figure 2.10a shows the force-displacement curves generated by var-

ious mesh densities. The formation of the damage process zone around the notch occurs during the hardening stage. Near the onset of crack nucleation (when damage in the transverse matrix crack path reaches unity in the first element), the force-displacement curve reaches peak. The crack propagation occurs as the force-displacement curve undergoes vertical drop. Despite the brittle nature of the structural cracking, the crack propagation phase is well-resolved using the proposed approach. This is evidenced by the fine resolution of the force drop in all simulations. The structural stiffness and strength is consistently predicted using the proposed approach with different mesh resolution (see inset in Fig. 2.10b). The mesh size insensitivity is further evidenced in Fig. 2.10c that shows the failure strength as a function of element size. The mean predicted value is 45 MPa, the standard deviation of 0.5 MPa.

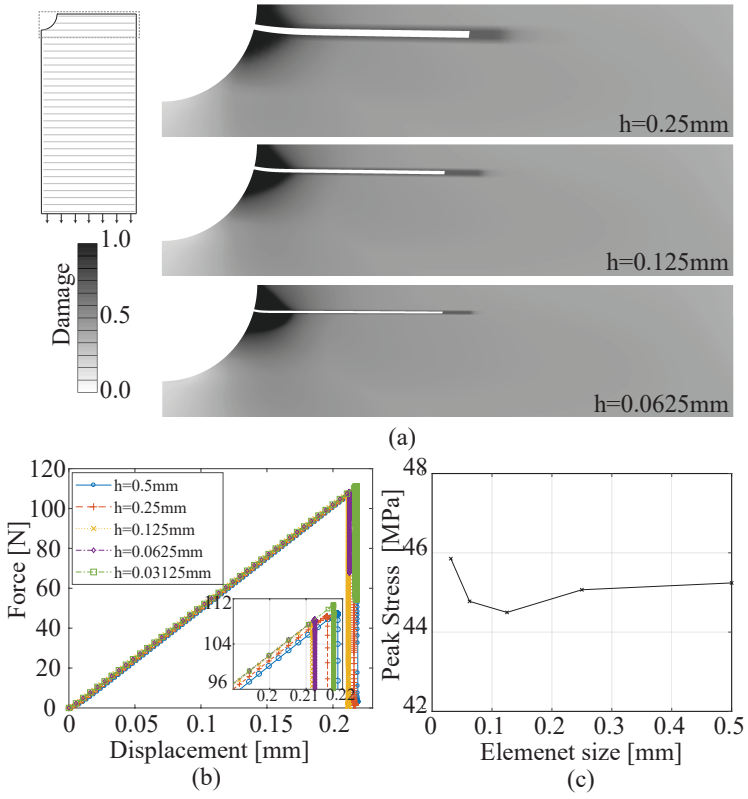

Figure 2.10: (a). Transverse matrix damage ($\omega^{(m)}$) contours and crack propagation in 90^o open-hole specimens with three element sizes of h=0.25 mm (top), h=0.125mm (middle), h=0.0625mm (bottom). (a) Force-displacement curves, (b) Peak (ultimate) strength as a function of element size.

Next, the capabilities of the proposed approach is demonstrated in a laminate configuration that results in more complex failure patterns. We study a $[0°/90°]_S$ laminate that includes four plies along the thickness direction. Only two of the plies were modeled exploiting symmetry in the

thickness direction. The remaining geometrical, loading and mesh configurations are set identical to those of the 90° lamina example described above. The damage contours within the zero and ninety plies predicted by three mesh sizes (i.e. h=0.25mm, 0.125mm, 0.0625mm) at the exact same stage of the loading process are shown in Fig. 2.11a. In the 0° ply, both fiber and matrix damage are observed, which nucleate at the notch. Fiber crack propagation is the critical mode and determines the strength of the structure. Before the nucleation of fiber fracture, the matrix damage forms a process zone near the notch and transverse matrix crack propagates along the vertical direction parallel to loading (i.e., splitting). The length of the split is approximately twice the radius of the hole. The lines(identified as red on the electronic version of the manuscript) in the figures are included to indicate the orientation of the matrix cracks and not a part of the simulations. The fiber crack then initiates and quickly propagates along the lateral direction (z direction). In the 90° layer, no fiber damage is observed. The transverse matrix damage in 90° ply extends around the axial splitting matrix crack in the 0° ply. The matrix damage in both plies form and propagate at approximately the same stages of loading and they stop to expand once the fiber fracture propagates and finally leads to overall structural failure. The pattern of damage contours described above matches well with those experimentally observed in specimens with similar laminate configurations (See e.g. Ref. [122]). No significant delamination occurs in $[0^\circ/90^\circ]$ cross-ply configurations. It is important to note that there are no significant differences between the final state of splitting and transverse matrix damage predicted by different discretizations in Fig. 2.11a, indicating that the matrix failure propagation before the overall structural failure is mesh size insensitive.

Figure 2.11b,c display the force-displacement curves predicted by the five discretizations, as well as the variation of the peak strength of the laminate as a function of element size. Similar to the 0° lamina case, the MDDT approach captures the crack propagation stage in the cross ply laminate. The mean strength is 805 MPa with a standard deviation of 9 MPa. The good agreement in strength predictions of different discretizations indicates that the total fracture dissipation for all the fracture mode is independent of mesh size choice and points to mesh-size objectivity.

2.5 Conclusion

This chapter demonstrates the main idea and mathematical framework of MDDT model. The proposed approach offers a reduced order representation of discrete fracture process at the scale of the

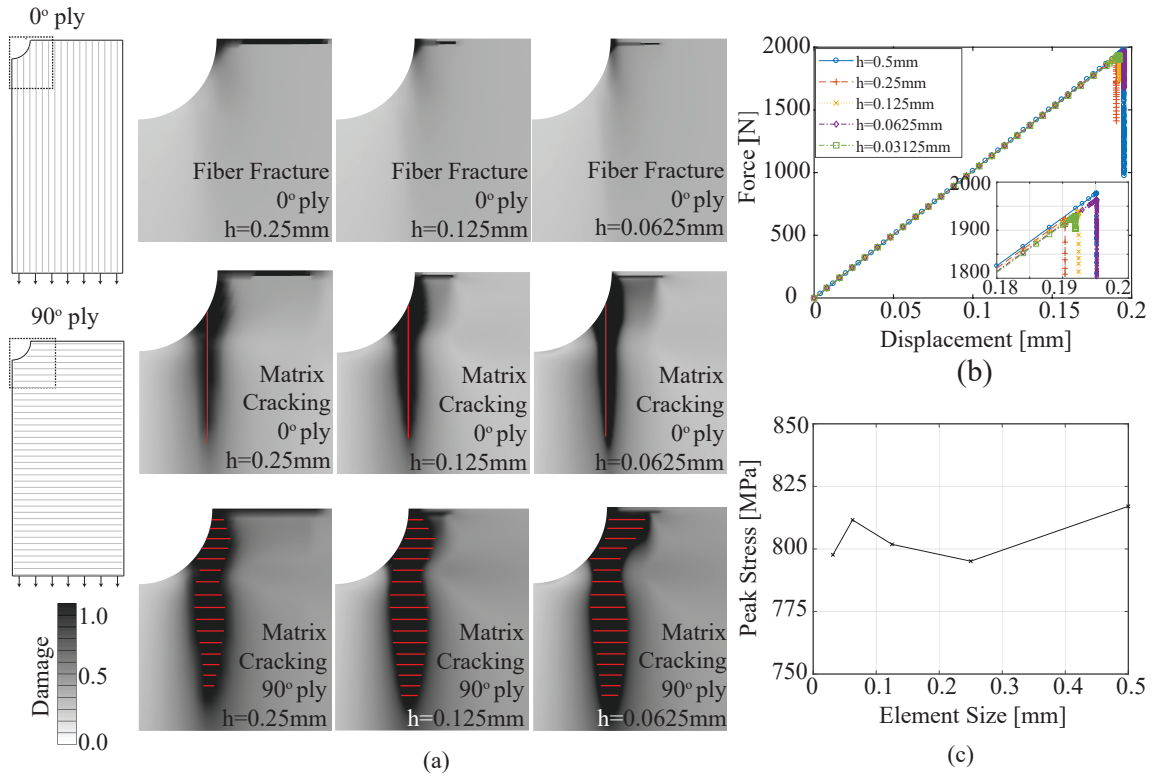

Figure 2.11: (a). Damage contours at different ply with three mesh densities in open-hole cross-ply $[0/90]_S$ laminates. (b) Force-displacement responses. (c) Peak strength as a function of element size.

material microstructure, which is bridged to continuum representation of damage at the structural scale based on homogenization approach. The proposed formulation achieves mesh size objectivity by employing the concept of macroscale element size-dependent microstructure volume. The mesh size objective formulation is achieved in an "effective" manner through analytical formulae that scales the reduced order model coefficients as a function of the macroscale element size. The capabilities of the proposed multiscale approach has been demonstrated in the context of 3-D laminated composite specimen configurations subjected to tensile loading. Numerical studies point to mesh size independence, as well as accurate treatment of simultaneous presence and growth of multiple mechanisms of failure including matrix damage and fiber fracture.

2.6 Appendix

The general equations are derived for the scaling of the coefficient tensors. In the case of a single failure path subjected to mode I loading, the only nonzero component of the separation coefficients

is the normal one $\boldsymbol{\delta} = \{\delta_N, 0, 0\}^T$. The corresponding homogenized strain tensor is expressed as:

$$\bar{\boldsymbol{\epsilon}} = \hat{\epsilon}_N \mathbf{n} \otimes \mathbf{n} + \hat{\epsilon}_{S_1} \mathbf{s}_1 \otimes \mathbf{s}_1 + \hat{\epsilon}_{S_2} \mathbf{s}_2 \otimes \mathbf{s}_2 \tag{2.50}$$

where $\mathbf{n}$, $\mathbf{s}_1$ and $\mathbf{s}_2$ are basis vectors of local coordinates along with the failure path. The tensor components are all expressed in the local coordinates.

With $\Re_\xi = \Re(\Theta_\xi, S_\xi; \mathbf{C}, \mathbf{D}_\xi, \mathbf{Z}_\xi)$ defined by microstructure with size scale ratio ξ, the weak equilibrium equation (Eq. 2.14) and the macroscopic constitutive relationship (Eq. 2.21) are:

$$[(1-\omega)\,\mathbf{K} + \mathbf{D}_\xi] \cdot \boldsymbol{\delta} - \mathbf{C} : \bar{\boldsymbol{\epsilon}} = \mathbf{0} \tag{2.51}$$

$$\bar{\boldsymbol{\sigma}} = \bar{\mathbf{L}} : \bar{\boldsymbol{\epsilon}} + \mathbf{Z}_\xi \cdot \boldsymbol{\delta} \tag{2.52}$$

Substituting the form of the mode I separation coefficient vector and the macro strain state yields (in the indicial notation):

$$[(1-\omega)\,K_{i1} + (D_\xi)_{i1}]\,\delta_N - (C_{i11}\hat{\epsilon}_N + C_{i22}\hat{\epsilon}_{S_1} + C_{i33}\hat{\epsilon}_{S_2}) = 0 \tag{2.53}$$

$$\hat{\sigma}_{ij} = \bar{L}_{ij11}\hat{\epsilon}_N + \bar{L}_{ij22}\hat{\epsilon}_{S_1} + \bar{L}_{ij33}\hat{\epsilon}_{S_1} + (Z_\xi)_{ij1}\delta_N \tag{2.54}$$

Since $K_{21} = 0$, $K_{31} = 0$ and setting $i = 2, 3$ in Eq. 2.53, $\hat{\epsilon}_{S_1}$ and $\hat{\epsilon}_{S_2}$ are expressed in terms of $\hat{\epsilon}_N$ and δ_N:

$$\hat{\epsilon}_{S_1} = \nu_1 \hat{\epsilon}_N + \mu_1(\xi)\delta_N \tag{2.55}$$

$$\hat{\epsilon}_{S_2} = \nu_2 \hat{\epsilon}_N + \mu_2(\xi)\delta_N \tag{2.56}$$

where ν_1, ν_2, $\mu_1(\xi)$ and $\mu_2(\xi)$ are:

$$\nu_1 = -\frac{C_{211}C_{333} - C_{311}C_{233}}{C_{222}C_{333} - C_{322}C_{233}} \tag{2.57}$$

$$\nu_2 = -\frac{C_{211}C_{322} - C_{311}C_{222}}{C_{233}C_{322} - C_{333}C_{222}} \tag{2.58}$$

$$\mu_1(\xi) = \frac{(D_\xi)_{21}C_{333} - (D_\xi)_{31}C_{233}}{C_{222}C_{333} - C_{322}C_{233}} \tag{2.59}$$

$$\mu_2(\xi) = \frac{(D_\xi)_{21} C_{322} - (D_\xi)_{31} C_{222}}{C_{233} C_{322} - C_{333} C_{222}} \tag{2.60}$$

Substituting Eqs. 2.55 - 2.60 into Eqs. 2.53 and 2.54 yield:

$$\left[(1-\omega)\, K_{11} + D_{\xi n}\right] \delta_N - C_n \hat{\epsilon}_N = 0 \tag{2.61}$$

$$\hat{\sigma}_{11} = E_n \hat{\epsilon}_N + Z_{\xi n} \delta_N \tag{2.62}$$

$$\hat{\sigma}_{22} = E_{s_1} \hat{\epsilon}_N + Z_{\xi s_1} \delta_N \tag{2.63}$$

$$\hat{\sigma}_{33} = E_{s_2} \hat{\epsilon}_N + Z_{\xi s_2} \delta_N \tag{2.64}$$

Each coefficient can be written as:

$$D_{\xi n} = (D_\xi)_{11} - C_{122}\mu_1(\xi) - C_{133}\mu_2(\xi) \tag{2.65}$$

$$C_n = -C_{111} - C_{122}\nu_1 - C_{133}\nu_2 \tag{2.66}$$

$$E_n = \bar{L}_{1111} - \bar{L}_{1122}\nu_1 - \bar{L}_{1133}\nu_2 \tag{2.67}$$

$$E_{s_1} = \bar{L}_{2211} - \bar{L}_{2222}\nu_1 - \bar{L}_{2233}\nu_2 \tag{2.68}$$

$$E_{s_2} = \bar{L}_{3311} - \bar{L}_{3322}\nu_1 - \bar{L}_{3333}\nu_2 \tag{2.69}$$

$$Z_{\xi n} = (Z_\xi)_{111} - \bar{L}_{1122}\mu_1(\xi) - \bar{L}_{1133}\mu_2(\xi) \tag{2.70}$$

$$Z_{\xi s_1} = (Z_\xi)_{221} - \bar{L}_{2222}\mu_1(\xi) - \bar{L}_{2233}\mu_2(\xi) \tag{2.71}$$

$$Z_{\xi s_2} = (Z_\xi)_{331} - \bar{L}_{3322}\mu_1(\xi) - \bar{L}_{3333}\mu_2(\xi) \tag{2.72}$$

Taking the derivative of Eq. 2.62 and using Eq. 2.61, the softening slope of the normal stress-strain relationship $E^s_\xi = \partial\hat{\sigma}_{11}/\partial\hat{\epsilon}_N$ is obtained as:

$$E^s_\xi = E_n + \frac{Z_{\xi n} C_n}{A_n + D_{\xi n}} \tag{2.73}$$

where $A_n = \partial t_N / \partial \delta_N$, representing the approximately linear softening of traction-separation relations denoted as $t_N = (1-\omega) K_{11} \delta_N$. Setting $\xi = 1$ and denoting the corresponding values of $D_{\xi n}$, $Z_{\xi n}$ and E^s_ξ as D_n, Z_n and E^s, respectively:

$$E^s = E_n + \frac{Z_n C_n}{A_n + D_n} \tag{2.74}$$

For the purpose of mesh size objectivity as explained in the main text above and as shown in Fig. 2.2, the relationship between E^s_ξ and E^s becomes:

$$E^s \frac{h(l-h)}{l} = \frac{E_n\, E^s_\xi}{E_n/(l-h) + E^s_\xi/h} \tag{2.75}$$

and by substituting the scaling ratio $\xi = l/h$, we obtain:

$$E^s_\xi = \frac{E_n E^s}{\xi E_n + (1-\xi)E^s} \tag{2.76}$$

Considering the forms $D_{\xi n} = \eta_N D_n$ and $Z_{\xi n} = \eta_N Z_n$ for the adjustment of the coefficient tensors in mode I, the scaling parameter η_N can be obtained by substituting Eqs. 2.73, 2.74 into 2.76:

$$\eta_N = \frac{\xi A_n}{A_n + (1-\xi)(D_n E_n + Z_n C_n)E_n^{-1}} \tag{2.77}$$

In the above expressions, ν_1, ν_2, $\mu_1(\xi)$ and $\mu_2(\xi)$ are introduced to account for the strain triaxiality. In the examples provided in this manuscript, the differences were found to be small.

Next, we extend the derivation of the residual stiffness correction along the same lines. In this case, we set $D_{\xi n} = \eta_N D_n$ and $Z_{\xi n} = \eta_N \eta^r_N Z_n$, where $\widetilde{\eta}_N$ and η^r_N respectively stand for the scaling parameters for crack localization and residual stiffness in the normal direction. The softening slope of the normal stress-strain relationship then becomes:

$$E^s_\xi = E_n + \frac{\widetilde{\eta}_N \eta^r_N Z_n C_n}{A_n + \eta_N D_n} \tag{2.78}$$

At the onset of complete loss of cohesion (i.e., $A_n = 0$), the scaled normal residual stiffness $\hat{E}^r_n$ is expressed as:

$$\hat{E}^r_n(\eta^r) = E_n + \eta^r_N \frac{Z_n C_n}{D_n} \tag{2.79}$$

Let E^r_n denote the value of $\hat{E}^r_n$ when $\eta^r = 1$. If we set the correction factor k^r_N for normal residual stiffness: $k^r_N = \hat{E}^r_n / E^r_n$, η^r_N is expressed as:

$$\eta^r_N = -(1-k^r_N)\frac{D_n E_n}{Z_n C_n} + k^r_N \tag{2.80}$$

Similarly, setting $\xi = 1$ enables the normal softening slope to become:

$$E^s = E_n + \frac{\eta_N^r Z_n C_n}{A_n + D_n} \tag{2.81}$$

Substituting Eqs. 2.80, 2.78, 2.81 into Eq. 2.76, $\widetilde{\eta}_N$ is expressed as:

$$\widetilde{\eta}_N = \frac{\xi A_n}{A + k_N^r \left(1 - \xi\right) \left(D_n E_n + Z_n C_n\right) E_n^{-1}} \tag{2.82}$$

If k_N^r is set to vanish, we observe that $\widetilde{\eta}_N = \xi$.

In addition to the mode I condition discussed above, the scaling relationships are derived for mode II condition. In this case, the separation vector is first set to $\boldsymbol{\delta} = \{0, \delta_{S_1}, 0\}^T$. The corresponding homogenized strain tensor takes the form:

$$\bar{\boldsymbol{\epsilon}} = \begin{bmatrix} 0 & \hat{\gamma}_{ns_1} & \hat{\gamma}_{ns_2} \\ \gamma_{ns_1} & 0 & \hat{\gamma}_{s_1 s_2} \\ \hat{\gamma}_{ns_2} & \hat{\gamma}_{s_1 s_2} & 0 \end{bmatrix} \tag{2.83}$$

The weak equilibrium equation and macroscopic constitutive relationship become:

$$\left[\left(1 - \omega\right) K_{22} + \left(D_\xi\right)_{22}\right] \delta_{S_1} - C_{212} \hat{\gamma}_{ns_1} = 0 \tag{2.84}$$

$$\hat{\sigma}_{12} = \bar{L}_{1212} \hat{\gamma}_{ns_1} + \left(Z_\xi\right)_{122} \delta_{S_1} \tag{2.85}$$

It is important to note that C_{213}, C_{223}, $\bar{L}_{1213}$ and $\bar{L}_{1223}$ are neglected due to the observation that $C_{213} \ll C_{212}$, $C_{223} \ll C_{212}$, $\bar{L}_{1213} \ll \bar{L}_{1212}$, $\bar{L}_{1223} \ll \bar{L}_{1212}$. Considering the form: $\left(D_\xi\right)_{22} = \eta_{S_1} D_{22}$ and $\left(Z_\xi\right)_{122} = \eta_{S_1} Z_{122}$, the softening shear modulus $G_\xi^s = \partial \hat{\sigma}_{12} / \partial \hat{\gamma}_{ns_1}$ is computed by differentiating Eq. 2.85 and using Eq. 2.84:

$$G_\xi^s = \bar{L}_{1212} + \frac{\eta_{S_1} Z_{122} C_{212}}{A_{s1} + \eta_{S_1} D_{22}} \tag{2.86}$$

where, A_{s1} stands for the softening slope of traction-separation curve in shear direction. Similarly,

$\eta_{S_1} = 1$ is ensured when $\xi = 1$. the softening shear modulus therefore becomes:

$$G^s = \bar{L}_{1212} + \frac{Z_{122}C_{212}}{A_{s1} + \eta_{S_1} D_{22}} \tag{2.87}$$

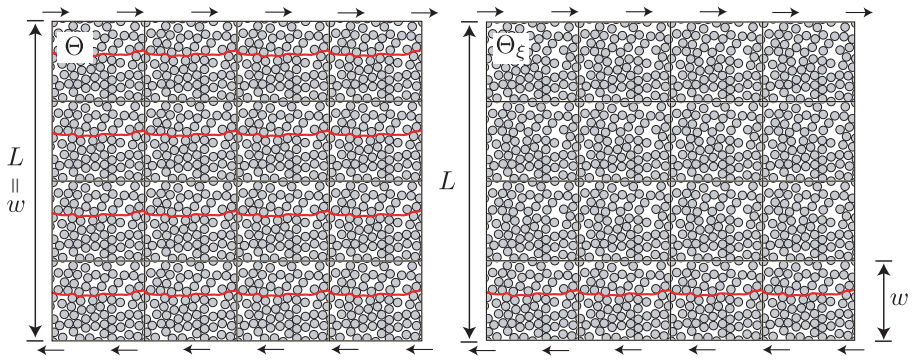

Figure 2.12: Scaling illustration under approximate simple shear load (a) domain without damage localization represented by repetition of reference microstructure (b) domain with damage localization

An approximate simple shear case is considered corresponding to mode II condition as shown in Figure 2.12. The relationship between G^s_ξ and G^s set to achieve mesh size objectivity is given as:

$$G^s \frac{h(l-h)}{l} = \frac{\bar{L}_{1212} G^s_\xi}{\bar{L}_{1212}/(l-h) + G^s_\xi/h} \tag{2.88}$$

By substituting Eqs. 2.86 and 2.87 to 2.88, scaling parameter η_{S_1} for mode II can be written as:

$$\eta_{S_1} = \frac{\xi A_{s1}}{A_{s1} + (1-\xi)(D_{22}\bar{L}_{1212} + Z_{122}C_{212})\bar{L}^{-1}_{1212}} \tag{2.89}$$

The residual stiffness correction in mode II follows the same scheme as discussed above for mode I. The scaling parameters $\widetilde{\eta}_{S_1}$ and $\eta^r_{S_1}$ corresponding to damage localization and residual stiffness correction are:

$$\widetilde{\eta}_{S_1} = \frac{\xi A_{s1}}{A_{s1} + k^r_{s1}\,(1-\xi)\,(D_{22}\bar{L}_{1212} + Z_{122}C_{212})\bar{L}^{-1}_{1212}} \tag{2.90}$$

$$\eta^r_{S_1} = -(1-k^r_{S_1})\frac{D_{22}\bar{L}_{1212}}{Z_{122}C_{212}} + k^r_{S_1} \tag{2.91}$$

In the orthogonal direction that excites mode II, the separation coefficient vector is set to $\boldsymbol{\delta} = \{0, 0, \delta_{S_2}\}^T$. The form of scaling relationships are exactly the same as above, only the components of the coefficient tensors are changed in the expressions of scaling parameters:

$$\eta_{S_2} = \frac{\xi A_{s2}}{A_{s2} + (1-\xi)(D_{33}\bar{L}_{1313} + Z_{133}C_{313})\bar{L}^{-1}_{1313}} \tag{2.92}$$

Extending to residual stiffness correction, scaling parameters $\widetilde{\eta}_{S_1}$ and $\eta^r_{S_1}$ corresponding to damage localization and residual stiffness correction are given as:

$$\widetilde{\eta}_{S_2} = \frac{\xi A_{s2}}{A_{s2} + k^r_{s2}\,(1-\xi)\,(D_{33}\bar{L}_{1313} + Z_{133}C_{313})\bar{L}^{-1}_{1313}} \tag{2.93}$$

$$\eta^r_{S_2} = -(1-k^r_{S_2})\frac{D_{33}\bar{L}_{1313}}{Z_{133}C_{313}} + k^r_{S_2} \tag{2.94}$$

Considering the case that the correction factors $k^r_{S_1}$ and $k^r_{S_2}$ vanish, we obtain the usual classical scaling relationship: $\widetilde{\eta}_{S_1} = \widetilde{\eta}_{S_2} = \xi$.

CHAPTER 3

MULTISCALE DISCRETE DAMAGE THEORY FOR FATIGUE

3.1 Introduction

This chapter extends the new proposed multiscale modeling MDDT to fatigue analysis of fiber-reinforced composite. One important topic still points to regularization for mesh-size objectivity. Mentioned in section 2.2.3, the analytical scaling relationship between coefficient tensors and macroscopic element size are derived based on assumption of linear or near-linear softening, however, many cyclic-sensitive constitutive laws (i.e., traction-separation) dissipate substantial fraction of the fracture energy during the hardening stage of the loading process [57, 68–71, 93, 123]. Some of the fatigue damage models do not employ a softening regime and idealize the entire degradation process during hardening [68–70, 93, 123]. Those models still exhibit mesh size sensitivity in the absence of a softening stage because the crack tip stress becomes singular and damage growth accelerates with increasing mesh density [71]. Therefore, dissipation via softening is essential to hold the assumption of cohesive fracture and effectiveness of regularization formulation. In this chapter, the non-additive scheme is employed for the following fatigue numerical experiments.

In order to accelerate fatigue life predictions, the MDDT approach is integrated with a multiple time scaling approach [68, 69]. The efficacy of the model is demonstrated in the context of unnotched and open-hole laminate configurations (0° ply and $[90^\circ/0^\circ]_S$ cross-ply) subjected to high-cycle fatigue loading. A parametric study is conducted to explain the difference of fatigue damage pattern in thermoplastic and thermoset composite laminates.

3.2 Non-additive Cyclic Sensitive Damage Evolution Law

This section provides the specific cohesive law used to idealize the progressive failure along a failure path subjected to cyclic loading. The proposed law is a variant of the constitutive model devised by Khoramishad et al. [124], who introduce two damage variables to describe the cycle-sensitive failure behavior. The traction-separation relationship is already shown in Eq. 2.32. The classical

bilinear form is adopted in this chapter, and the cohesive damage variable is expressed as:

$$\omega(\kappa) = \begin{cases} 0 & \kappa \leq \nu_c \\ \dfrac{\nu_u\left(\kappa - \nu_c\right)}{\kappa\left(\nu_u - \nu_c\right)} & \nu_c < \kappa \leq \nu_u \\ 1 & \kappa > \nu_u \end{cases} \tag{3.1}$$

where $\kappa(t) = \max\limits_{\tau\in[0,t]}\{\nu(\tau)\}$ is the history variable of equivalent separation ν, $\nu = \|\boldsymbol{\delta}\| = \sqrt{\delta_N^2 + \delta_{S_1}^2 + \delta_{S_2}^2}$, where δ_N satisfies $\delta_N \geq 0$ to eliminate the possibility of interpenetration. ν_c and ν_u respectively correspond to the values of the equivalent separation at the onset of the softening region and at ultimate failure. They are evaluated under mixed-mode conditions based on a quadratic damage initiation criterion [116] and using the B-K criterion [125]:

$$\nu_c = \delta_{c_{\mathrm{I}}}^f \delta_{c_{\mathrm{II}}}^f \sqrt{\frac{1+{\beta_m}^2}{(\delta_{c_{\mathrm{II}}}^f)^2 + \left(\beta_m \delta_{c_{\mathrm{I}}}^f\right)^2}} \tag{3.2}$$

$$\nu_u = \frac{2}{K\nu_c}\left[G_{\mathrm{I}c}^f + (G_{\mathrm{II}c}^f - G_{\mathrm{I}c}^f)\left(\frac{{\beta_m}^2}{1+{\beta_m}^2}\right)^{\eta_{\mathrm{BK}}}\right] \tag{3.3}$$

where β_m is the mixed-mode ratio defined as the ratio between tangential and normal separations, $\beta_m = \sqrt{\delta_{S_1}^2 + \delta_{S_2}^2}/\delta_N$. Degradation behavior under repetitive cyclic loading is modeled by introducing the fatigue damage variable $\omega_f \in [0,1]$. Unlike ω, which degrades the instantaneous secant stiffness, the fatigue damage variable acts on the critical separation at the onset of damage and the critical energy release rate:

$$\delta_{c_{\mathrm{I}}}^f = \delta_{c_{\mathrm{I}}}\left(1-\omega_f\right), \quad \delta_{c_{\mathrm{II}}}^f = \delta_{c_{\mathrm{II}}}\left(1-\omega_f\right) \tag{3.4}$$

$$G_{\mathrm{I}c}^f = G_{\mathrm{I}c}(1-\omega_f)^2, \quad G_{\mathrm{II}c}^f = G_{\mathrm{II}c}(1-\omega_f)^2 \tag{3.5}$$

where, $\delta_{c_{\mathrm{I}}}$, $\delta_{c_{\mathrm{II}}}$ are equivalent separations at the onset of the softening region, $G_{\mathrm{I}c}$ and $G_{\mathrm{II}c}$ are critical fracture energies under mode-I and mode-II conditions. Under pure mode I loading ($\beta_m = 0$), the critical and ultimate equivalent separations become $\nu_c = \delta_{c_{\mathrm{I}}}^f$ and $\nu_u = \delta_{u_{\mathrm{I}}}^f$, respectively. Similarly, pure mode II loading ($\beta_m = \infty$) results in critical and ultimate equivalent separations of $\nu_c = \delta_{c_{\mathrm{II}}}^f$ and $\nu_u = \delta_{u_{\mathrm{II}}}^f$, respectively. $\delta_{c_{\mathrm{I}}}^f$, $\delta_{c_{\mathrm{II}}}^f$, $G_{\mathrm{I}c}^f$ and $G_{\mathrm{II}c}^f$ are effectively the fracture parameters

of a cohesive interface that has been cyclically damaged by ω_f. Considering the bilinear form of the cohesive law: $t_u = K\delta_c$, $G_c = t_u\delta_u/2$, the fatigue degradation can also be regarded as reducing the peak traction t_u and ultimate equivalent separation δ_u: $t_u^f = t_u\,(1-\omega_f)$, $\delta_u^f = \delta_u\,(1-\omega_f)$. The stiffness and softening slope of the traction-separation relationship is not influenced by fatigue damage.

In order to account for the presence of fatigue damage variable, the history variable κ is expressed as:

$$\kappa(t) = \max_{\tau\in[0,t]}\left\{\frac{\nu(\tau)}{1-\omega_f(\tau)}\right\}(1-\omega_f(t)) \tag{3.6}$$

In the absence of cyclic degradation (i.e., $\omega_f = 0$), Eq. 3.6 degrades to its original definition.

With respect to the evolution law for fatigue damage, this work adopts separation-based form [71]:

$$\dot{\omega_f} = C\exp\left(\lambda\omega_f\right)\left(\frac{\nu}{\nu_u}\right)^{\beta_f}\frac{\langle\dot{\nu}\rangle_+}{\nu_u} \tag{3.7}$$

where λ is a material parameter, and $\langle\cdot\rangle_+ = [|\cdot| + (\cdot)]/\,2$ denotes the Macaulay brackets. In order to model fatigue damage evolution under mixed-mode conditions, the amplitude coefficient C and the power index β_f are respectively defined as functions of the mixed mode ratio (following the form of the B-K model [126]):

$$\ln C = \ln C_{\mathrm{II}} + [\ln C_{\mathrm{I}} - \ln C_{\mathrm{II}}](\frac{1}{1+\beta_m^2})^{m_c} \tag{3.8}$$

$$\beta_f = \beta_{f_{\mathrm{I}}} + (\beta_{f_{\mathrm{II}}} - \beta_{f_{\mathrm{I}}})(\frac{\beta_m^2}{1+\beta_m^2})^{m_{\beta_f}} \tag{3.9}$$

where $C = C_{\mathrm{I}}$, $\beta_f = \beta_{f_{\mathrm{I}}}$ indicate the material properties that control the fatigue damage evolution under pure mode I loading (i.e. $\beta_m = 0$), and $C = C_{\mathrm{II}}$, $\beta_f = \beta_{f_{\mathrm{II}}}$ under pure mode II (i.e., $\beta_m \to \infty$). Power indices m_c and m_{β_f} are additional parameters controlling damage evolution under mixed mode loading.

Figure 3.1 schematically illustrates a typical behavior of the cohesive law subjected to cyclic loading. For generality of demonstration, a separation-controlled variable amplitude loading is employed to generate the traction-separation curve. The figure illustrates that if the peak traction magnitude does not reach the instantaneous ultimate traction (i.e., t_u^f), the behavior is non-dissipative

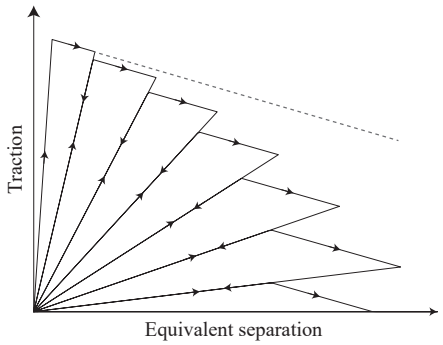

Figure 3.1: Traction-separation curve obtained by non-additive scheme under cyclic loading. Dash line represents the bilinear profile obtained under monotonic loading.

and t_u^f reduces under cyclic loading. The softening slope remains constant regardless of the value of t_u^f. The energy dissipation occurs only during the softening regime. This is crucial to regularization of MDDT model as it adjusts dissipated energy by regularizing the softening moduli of the homogenized stress-strain relationship.

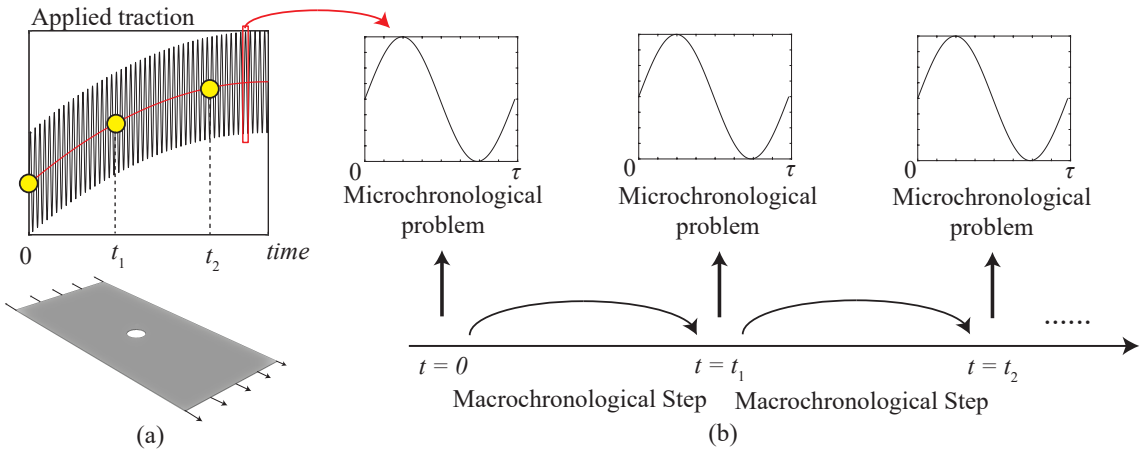

Figure 3.2: (a) Fatigue loading history, (b) Time domain decomposition in the temporal multiscale scheme.

3.3 Temporal Multiscale Scheme

Straightforward time integration of the governing equations of the MDDT model to characterize long-term damage evolution and failure is computationally prohibitive for high cycle fatigue. In such a *cycle-by-cycle* approach, each loading cycle is discretized into several increments and the

governing equations of the MDDT model is evaluated using a nonlinear solver (e.g., Newton-Raphson or others) for each increment of each cycle. Instead, we accelerate the simulations by adopting the multiple time scale life prediction methodology proposed in Ref. [68, 127]. In this regard, two problems are defined separated by the time scales they operate. The *microchronological* problem evaluates the response subjected to a single load cycle (summarized in Box A in the appendix). The *macrochronological* problem provides the long-term evolution of damage and equilibrium state. The governing system of equations are summarized in the appendix for brevity of this discussion.

The implementation of the multiple time scale approach is similar to the block-cycle modeling [67] and illustrated in Fig. 3.2. The micro- and macrochronological problems are evaluated in a tightly coupled fashion. At each macro-chronological increment, t_i, a microchronological problem is evaluated to compute the rate of fatigue damage evolution. The macrochronological time increments are adaptively set [69] based on maximum allowable damage accumulation ($\Delta\omega_p$) within a single increment. The coupling between the micro- and macrochronological problems is implemented using Python scripts that involve the appropriate problem in turn as shown in Fig. 3.2.

Following Ref. [69], the microchronological problem is evaluated in a quasi-linear fashion, where the damage accumulation is assumed to not affect the equilibrium state within a single load cycle. By this approach, fatigue damage accumulation within the microchoronologcal problem is expressed in cyclic form as:

$$\frac{\mathrm{d}\omega_f}{\mathrm{d}N} = \frac{C(1-\omega_f)^{1+\beta_f}}{1+\beta_f}\exp\left(\lambda\omega_f\right)\left[\left(\frac{\nu_{max}}{\nu_u}\right)^{\beta_f+1} - \left(\frac{\nu_{min}}{\nu_u}\right)^{\beta_f+1}\right] \tag{3.10}$$

where ν_{max} and ν_{min} are respectively maximum and minimum equivalent separation within the unit loading cycle. Load characteristic such as the R-ratio natually affects fatigue damage accumulation in the microchronological problem. This is evident in Eq. 3.10 due to the presence of ν_{max} and ν_{min} terms.

3.4 Numerical Verification

In this section, fatigue simulations using un-notched and open-hole laminate configurations are performed to verify the MDDT models in terms of (1) mesh-size objectivity and (2) capabilities in

capturing complex failure mechanisms.

Table 3.1: Elastic properties of matrix$^{(m)}$ and fiber$^{(f)}$

$E^{(m)}$ [GPa]	$\nu^{(m)}$	$E_1^{(f)}$ [GPa]	$E_2^{(f)}$ [GPa]	$G_{12}^{(f)}$[GPa]	$\nu_{12}^{(f)}$	$\nu_{23}^{(f)}$
3.55	0.35	263	13	27.5	0.32	0.20

The configuration and discretization of the reference microstructure employed for all numerical examples in this study are the same as Fig 2.3. In this chapter, besides the failure paths of matrix cracking and fiber fracture, delamination is also considered with the same morphology and fracture properties as matrix cracking but the orientation is different with respect to the ply lay up.

3.4.1 Unnotched Specimen

The unnotched numerical specimens subjected to cyclic loading are employed for verification of the MDDT model. The 90° unnotched numerical specimens are loaded under strain-controlled uni-axial tension and simple shear loading that respectively activate mode-I and mode-II dominant fracture in the matrix cracking failure path. The geometry, loading and discretization of the specimens are the same as Fig. 2.4a,b. The fracture parameters for the matrix cracking failure path is listed in Table 3.2. Compared to generic unidirectional carbon fiber reinforced thermoset composites, this example employs low mode-I and mode-II cohesive fracture energy release rates for the purposes of demonstration. More realistic material parameters are used in laminate analyses discussed in the next section. The loading amplitudes for uniaxial and simple shear loadings are respectively 1.02% and 2.5% total applied strain with R-ratio equals to 0 in both cases. In the uniaxial tension case, symmetry boundary conditions are applied at the three sides normal to x, y and z directions, respectively. In the shear case, the lateral side that is parallel to the failure path is fixed to ensure that the onset of mode-I failure is suppressed. The macroscopic domain is discretized with different mesh densities, where the corresponding length scale ratio is set to be $\xi = 1, 2, 4, 8, 16$ for verification of mesh-size objectivity. In the simple shear case, the coarsest discretization ($\xi = 1$) does not adequately resolve shear deformation and is not used. The boundary condition, the strategy to ensure damage localization, the element type are the same as the settings in section 2.4.1.1. Simulations using the temporal multiscale integration scheme as well as the reference direct cycle-by-cycle time

integration are conducted. In the reference simulations, the vast majority of the increments resolve the non-linear response in the loading or reloading regime. The fatigue damage tolerance parameter that adaptively controls macrochronological time step size is set to be 1% or 2% in the simulations that use the temporal multiscale scheme.

Table 3.2: Fracture parameters of matrix cracking for unnotched configuration

Cohesive Failure					
$G_{Ic}^{(m)}$	$G_{IIc}^{(m)}$	$t_{\text{uI}}^{(m)}$	$t_{\text{uII}}^{(m)}$	$K^{(m)}$	$\eta^{(m)}$
[MPa mm]	[MPa mm]	[MPa]	[MPa]	[MPa mm^{-1}]	
0.03	0.045	60	90	6×10^7	1
Fatigue damage evolution					
$C_{\text{I}}^{(m)}$	$C_{\text{II}}^{(m)}$	$\beta_{f_{\text{I}}}^{(m)}$	$\beta_{f_{\text{II}}}^{(m)}$	$m_c^{(m)}, m_{\beta_f}^{(m)}$	$\lambda^{(m)}$
2×10^{-3}	1×10^{-3}	0.1	0.1	1	0.1

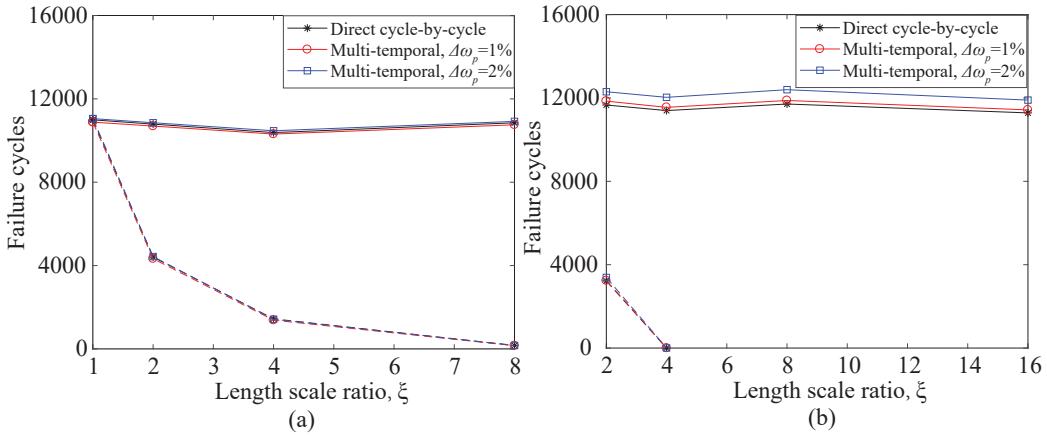

Figure 3.3: Fatigue life vs. length scale ratio (i.e. $\xi = l/h$) obtained by direct cycle-by-cycle scheme and temporal multiscale scheme with 1% and 2% tolerance for adaptive macrochronological time stepping strategy under (a) uniaxial and (b) shear loading. Solid lines show results with regularization, while dash lines indicate unregularized model.

Figures 3.3a and b show the predicted fatigue life for different mesh sizes under tensile and shear loading conditions, respectively. In this example, fatigue life refers to the number of load cycles, where the load carrying capacity of the structure vanishes (i.e., damage in the matrix crack failure path, $\omega^{(m)} = 1$). The solid curves indicate predicted fatigue life when the regularization approach is employed, whereas the dash curves are the results of the unregularized simulations. In all cases, the temporal multiscale scheme exhibits good agreement with the direct cycle-by-cycle scheme.

The corresponding average errors with step adaptivity tolerances of 1% and 2% are respectively less than 1.5% and 6% for all mesh size discretizations in both uniaxial and shear loaded cases. In contrast, the computational cost of the multiscale time integration scheme is significantly less than the reference scheme. The temporal multiscale scheme requires a total of 90 (normal) and 75 (shear) resolved cycles on average for tolerance of 1%, and 46 (normal) and 39 (shear) resolved cycles on average for tolerance of 2%, compared to 10,753 (normal) and 11,512 (shear) cycles resolved in the direct cycle-by-cycle scheme. A tradeoff exists between prediction accuracy and computational efficiency when choosing the tolerance: smaller value leads to higher accuracy but requires more macro-chronological time steps that reduces the efficiency of the approach. Because 2% tolerance has higher computational efficiency and also keeps reasonable accuracy, the open-hole simulations performed in this manuscript employ the temporal multiscale time integration algorithm with 2% tolerance.

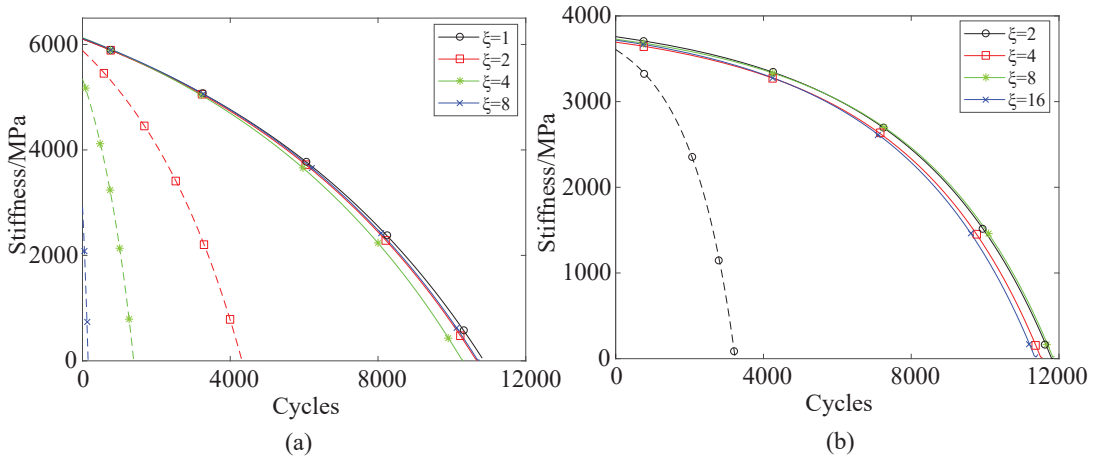

Figure 3.4: Residual stiffness vs. cycles obtained by the temporal multiscale scheme with 1% tolerance under (a) uniaxial and (b) shear loading. Solid lines show the results with regularization, while dash lines indicate the unregularized model.

3.4.2 Analysis of Open-hole Unidirectional Specimens

In this section, the capabilities of the MDDT model are demonstrated in predicting stable crack growth under fatigue loading conditions in a mesh size objective manner. The analysis is performed in the context of an open-hole 0° unidirectional tape. Figure 3.5 illustrates the geometry, loading and boundary conditions, and discretizations used in this study. The overall width, length and thickness of the specimen are 20mm, 28mm and 0.125mm, respectively. The hole radius is 3.175mm. 1/8

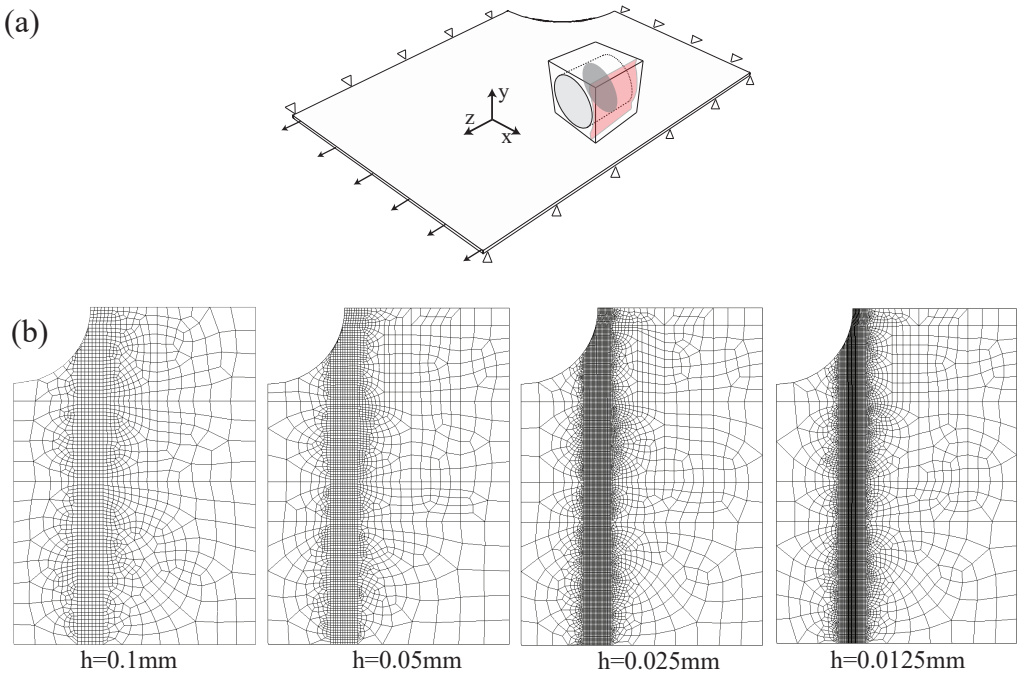

Figure 3.5: (a) Geometry, boundary and loading conditions, and the MDDT model configuration for open-hole 0° ply single lamina analysis. (b) Different mesh discretizations using the size of h=0.1mm, 0.05mm, 0.025mm, 0.0125mm.

of the specimen is discretized with symmetry boundary conditions applied at the three directions, leveraging symmetries of the specimen. As shown in Fig. 3.5b, the parts of the specimen, where the potential crack propagation is expected, is discretized with elements aligned with fiber direction to eliminate mesh bias effect. Different mesh sizes of 0.1mm, 0.05mm, 0.025mm, 0.0125mm within the potential crack propagation region of the specimen were used in order to verify mesh-size consistency. In the thickness direction, the ply is discretized using one element.

Table 3.3 lists the fracture properties for both failure paths of transverse matrix cracking and fiber fracture, which are consistent with generic unidirectionally carbon fiber reinforced thermoset composites. The parameters for fatigue damage evolution are selected within a reasonable range that the corresponding crack propagation rate is of the same order as experiments described in Ref. [59]. The analysis presented herein is focused on verification of mesh size objectivity. A formal calibration/validation study of a particular composite (See [68, 93]) is outside the scope of the current manuscript, and will be the emphasis of future studies.

Force-controlled uniaxial cyclic loading with an amplitude of 482 MPa (80% of static strength)

is applied to the specimen along z-direction with R-ratio equal to 0. The temporal multiscale scheme with 2% fatigue-damage tolerance for adaptive macro-chronological time stepping strategy is employed for the open-hole configurations.

Table 3.3: Fracture parameters for open-hole configuration

Cohesive failure for matrix cracking [128, 129]					
$G_{Ic}^{(m)}$	$G_{IIc}^{(m)}$	$t_{\mathrm{uI}}^{(m)}$	$t_{\mathrm{uII}}^{(m)}$	$K^{(m)}$	$\eta^{(m)}$
[MPa mm]	[MPa mm]	[MPa]	[MPa]	[MPa mm^{-1}]	
0.2	1	60	90	6×10^7	1
Fatigue damage evolution for matrix cracking and delamination					
$C_{\mathrm{I}}^{(m)}$	$C_{\mathrm{II}}^{(m)}$	$\beta_{f_{\mathrm{I}}}^{(m)}$	$\beta_{f_{\mathrm{II}}}^{(m)}$	$m_c^{(m)}$,$m_{\beta_f}^{(m)}$	$\lambda^{(m)}$
1×10^{-2}	1×10^{-4}	0.1	0.1	1	0.1

Cohesive failure & fatigue damage evolution for fiber fracture							
$G_{\mathrm{Ic}}^{(f)}$,$G_{\mathrm{IIc}}^{(f)}$ [MPa mm]	$t_{\mathrm{uI}}^{(f)}$, $t_{\mathrm{uII}}^{(f)}$ [MPa]	$K^{(f)}$ [MPa mm^{-1}]	$\eta^{(f)}$	$C_{\mathrm{I}}^{(f)}$,$C_{\mathrm{II}}^{(f)}$	$\beta_{f_{\mathrm{I}}}^{(f)}$,$\beta_{f_{\mathrm{II}}}^{(f)}$	$m_c^{(f)}$,$m_{\beta_f}^{(f)}$	$\lambda^{(f)}$
12	4000	4×10^9	1	10^{-7}	0.1	1	0.1

Figure 3.6 shows the contours of shear stress σ_{xz} captured at the first cycle, 30,000 cycles and 300,000 cycles which are predicted using the regularized MDDT model. The macroscopic crack is displayed by light colored elements (shown as red in the electronic version of the manuscript) which have reached completed damage state ($\omega^{(m)} = 1$). A single dominant splitting crack initiates at the hole brim at the first cycle and grows aligned with the fiber (vertical) direction under subsequent cyclic loading. No fiber damage is observed in this case. The fracture process zone ($0 < \omega^{(m)} < 1$) is represented by the white straight line ahead of the splitting crack and results in low shear stress around 90 MPa as splitting crack is mode-II dominant. The length of the fracture process zone becomes shorter with increasing crack length, because the stress concentration at the crack tip reduces as the split grows. The patterns of crack propagation and fracture process zone are both mesh-size consistent. Figure 3.7 displays the cyclic evolution of crack propagation and stiffness as a function of load cycles. Without regularization, the splitting crack propagation and stiffness loss drastically accelerates with decreasing macroscopic element size. For the regularized MDDT model, the initial crack growth occurs faster compared to the non-regularized cases. This is because, the regularized MDDT model is referenced to the case with the element size (i.e. damage

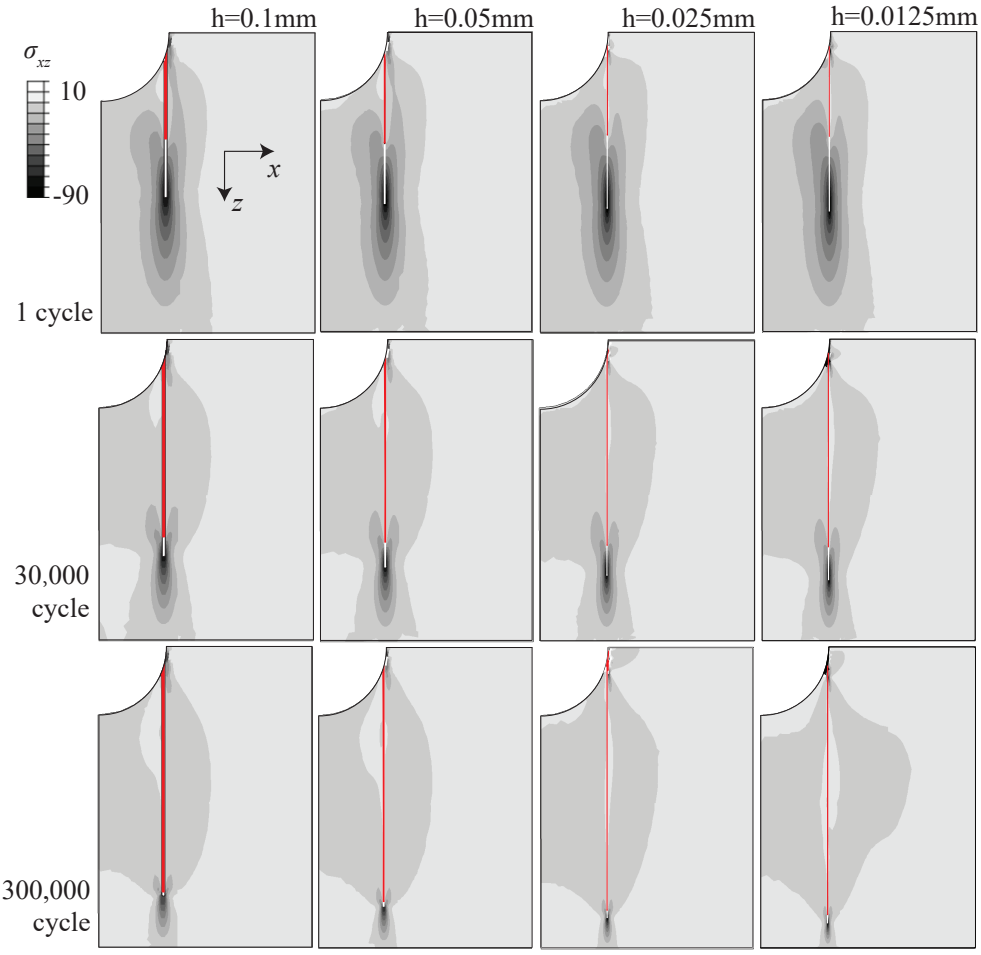

Figure 3.6: Shear stress contour σ_{xz} captured at the first cycle, 3×10^4 cycles and 3×10^5 cycles for 0° ply single lamina with mesh densities of h=0.1mm, 0.05mm, 0.025mm, 0.0125mm.

localization width) of $h = l = 0.01$mm, which is significantly finer than the finest mesh employed in this study. In addition, the results of the regularized MDDT model exhibits mesh-size consistent crack propagation rates and stiffness evolution. The crack growth and stiffness evolution curves also demonstrate converging trends with higher mesh densities. This indicates that the discrepancy between the regularized curves can be largely attributed to mesh resolution effects rather than spurious mesh size sensitivity.

3.4.3 Analysis of Cross-ply Open-hole Specimens

The capabilities of the proposed multiscale model are further assessed in a composite specimen configuration that exhibits diffuse damage, cracking and multiple failure mechanisms. We consider an open-hole $[90^\circ/0^\circ]_S$ cross-ply laminate configuration subjected to tensile fatigue loading. Fig-

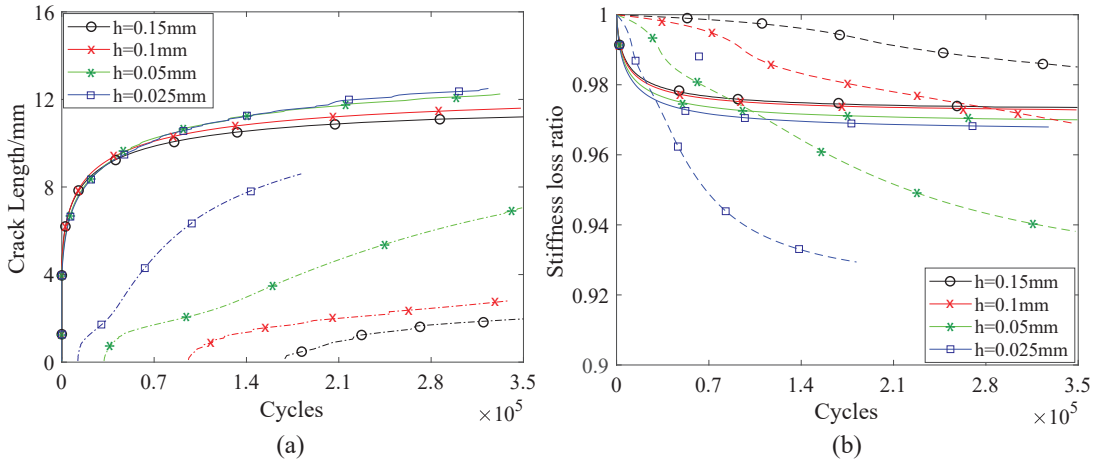

Figure 3.7: (a) Splitting crack extension and (b) residual stiffness loss ratio as a function of cycle number for 0° lamina. Solid and dash lines respectively denote the results obtained by regularized and non-regularized models.

ure 3.8 illustrates the geometry, loading and boundary conditions, and discretizations used in this case. Similar to the previous example, 1/8 of the specimen is modeled leveraging the symmetries in the laminate and geometry. Model parameters shown in Tables 3.1 and 3.3 are employed. Force-controlled uniaxial cyclic loading of 313 MPa (90% of static strength) is applied to the specimen along the z-direction with R-ratio equal to 0. Previous experimental observations reveal the presence of delamination that affects fatigue damage progression in carbon-fiber reinforced thermoset resins [59, 130, 131]. In order to better capture the kinematics of delamination propagation, delamination is modeled by inserting an additional thin layer of macroscopic elements in between the 90° and 0° plies, in which the associated microstructure is embedded with delamination failure path, shown in Fig. 6.2b. The microstructure employed for delamination layer elements is identical to the ply layers, except for the difference of failure path orientations between delamination and transverse matrix crack (See Fig. 6.2a,b). The thickness of the delamination layer is set to be 10 microns (8% ply thickness). MDDT regularization procedure ensures that the fracture energy consistency is satisfied regardless of the thickness of the delamination layer. The potential crack propagation region is discretized using the element sizes of 0.15mm, 0.1mm, 0.05mm in order to verify mesh-size objectivity (see Fig. 3.8b). As demonstrated in the simulations below, transverse matrix cracks within the 90° ply are bridged by fibers within 0° ply, and the damage does not fully localize. In the absence of damage localization, fracture energy associated with transverse matrix cracking in

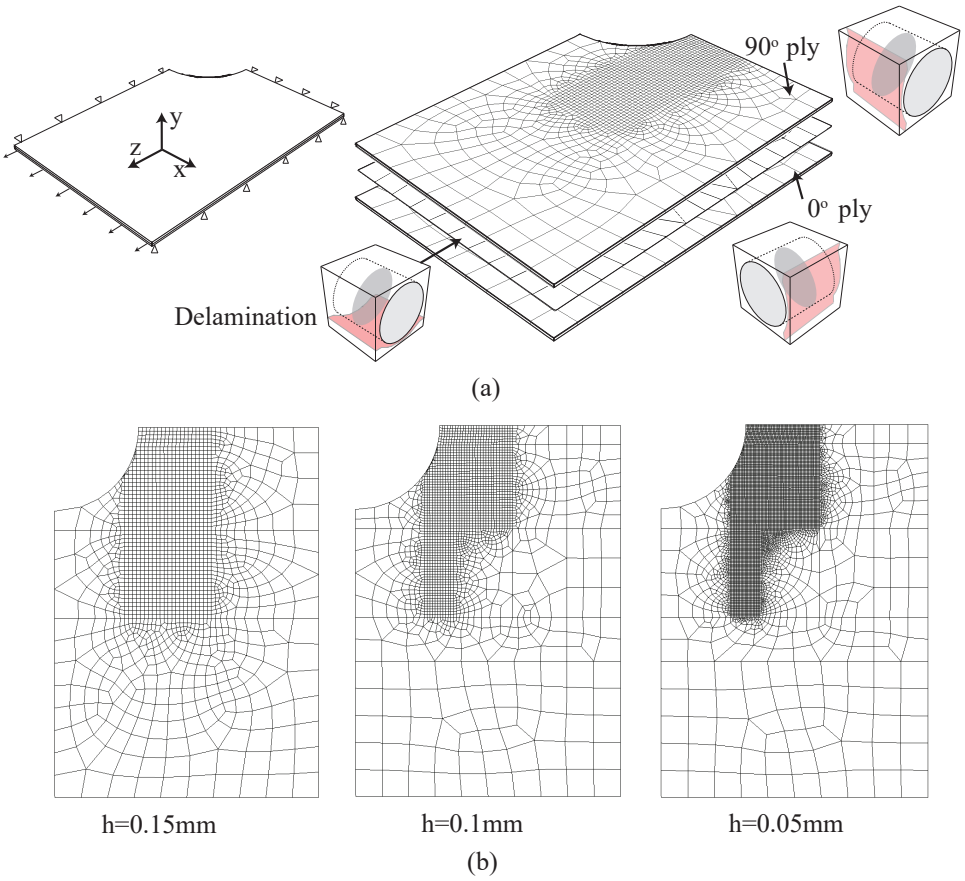

Figure 3.8: (a) Geometry, boundary and loading conditions for the open-hole $[90°/0°]_S$ cross-ply laminates, as well as microstructure configuration for each ply and delamination modeling. (b) Different mesh densities with h=0.15mm, 0.05mm, 0.025mm for discretization.

the $90°$ ply is mesh-size independent without the need for regularization. Applying regularization would result in an unphysical increase of fracture energy with mesh refinement, which suppresses this failure mode when fine meshes are used. In what follows, we therefore do not employ the regularization scheme for $90°$ transverse matrix cracks.

Figure 3.9 shows the damage contours for transverse matrix cracking in the $90°$ ply shown as dark region (black color in the electronic version), for splitting crack in the $0°$ ply shown as the light grey region (light blue color in the electronic version), and for delamination shown as medium grey (red color in the electronic version). Delamination contours are shown in both $90°$ and $0°$ plies. The figure shows the results using different mesh densities captured after the first load cycle, 160,000 cycles and 320,000 cycles. The first cycle of loading results in a substantial amount of damage near the hole that consist of a diffuse region of transverse matrix cracking in the $90°$ ply, a dominant split

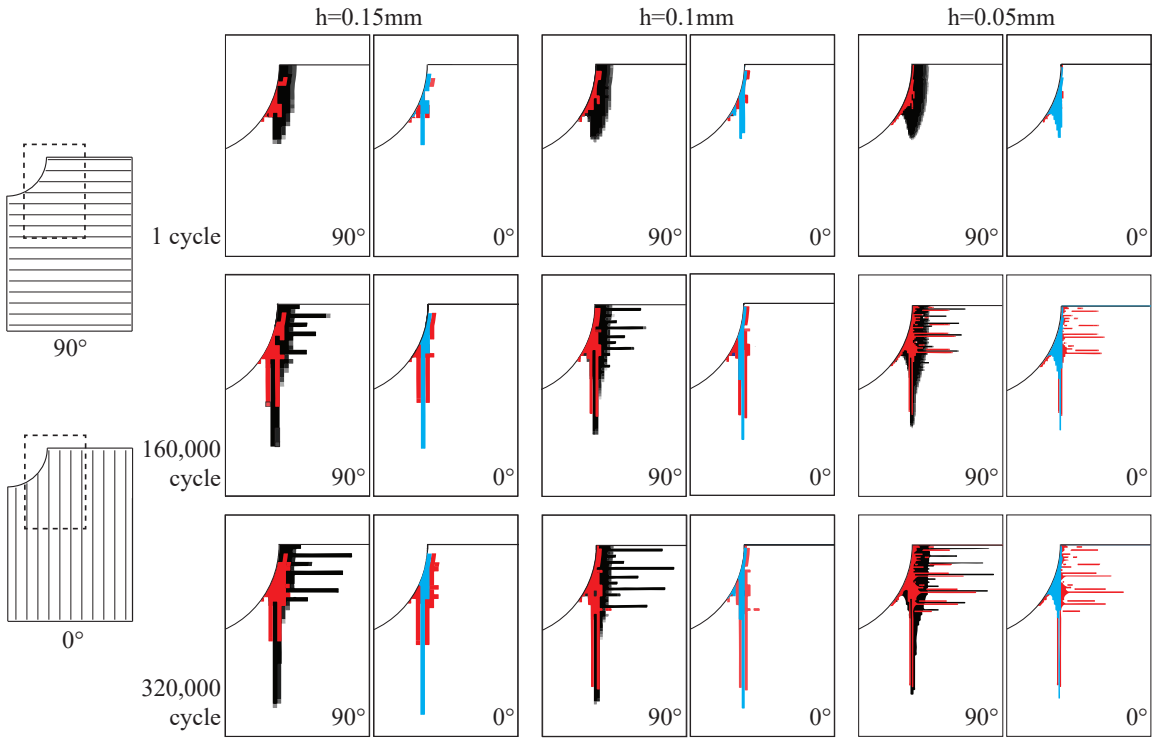

Figure 3.9: Transverse matrix crackings (black) in 90°, splitting crack (light blue) in 0° ply, as well as delamination (red) captured at the first cycle, 160,000 cycles and 320,000 cycles for different mesh sizes of h=0.15mm, 0.1mm, 0.05mm.

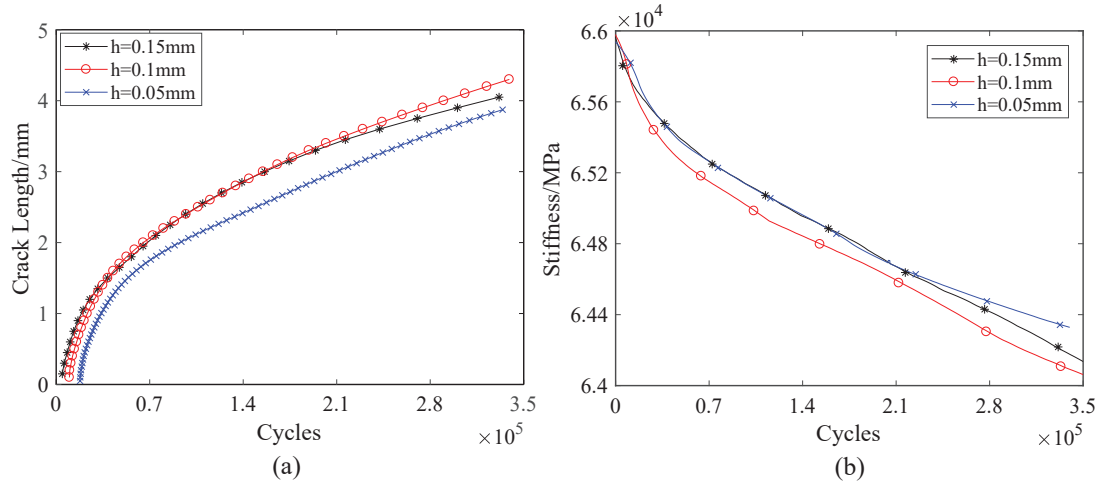

Figure 3.10: (a) Splitting crack propagation, and (b) residual stiffness as a function of cycle numbers for $[90°/0°]_S$ laminates.

in the 0° ply with length in the order of the hole radius, and some delamination. The level of damage observed is expected as the loading amplitude is large (90% of the static strength of the specimen). While significant damage is observed at the end of the first load near the hole, none of the failure

paths reach full fracture state within the specimen (i.e., corresponding damage variable reaching unity). Subsequent cycling results in stable growth of all three damage mechanisms. Distinct, yet diffuse transverse matrix cracks begin to grow in the 90° ply but arrested by the splitting crack. Delamination growth occurs around the growing split and the transverse cracks. A small amount of fiber damage also occurs near the hole (not shown in figure) and grows slowly compared with the matrix damage. The general feature of damage contours conform well with the X-ray tomography of the damage in the high cycle fatigue cases of Refs. [59, 130, 131], which employ similar laminate configurations. No significant difference in crack extension patterns appear when different meshes are used in the simulations.

Figure 3.10 shows the growth of the dominant splitting crack as a function of load cycles, as well as the evolution of specimen stiffness. Crack growth is considered to initiate when full damage in the "transverse matrix crack" failure path is reached in the first element along the split. The crack growth process follows a short incubation period. During the incubation period, damage growth does not fully localize (as shown in top rows of Fig. 3.9), and the regularization is not effective. This manifests itself in the differences in crack growth initiation cycles shown in Fig. 3.10a. The number of cycles during incubation are respectively 4,577 cycles, 9,911 cycles and 17,864 cycles for the simulations with coarse (h=0.15mm), medium (0.1mm) and fine (0.05mm) meshes. The cycles to initiation constitutes a small portion of the structural life and the errors do not affect the overall life prediction significantly. A reasonable overall mesh-size consistency is observed in both splitting crack growth and stiffness evolution curves.

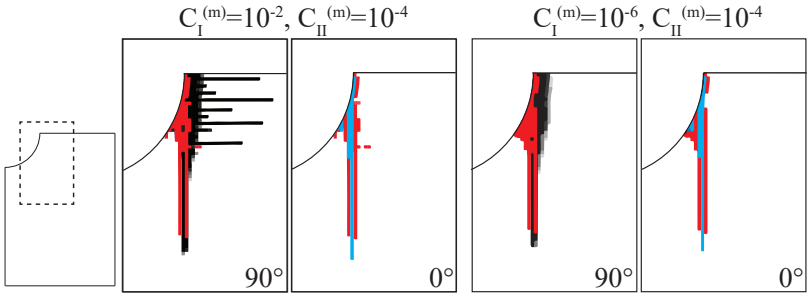

Figure 3.11: Transverse matrix crackings (black) in 90°, splitting crack (light blue) in 0° ply and delamination (red) captured at 320,000 cycles compared between $C_{\mathrm{I}}^{(m)} = 0.01$, $C_{\mathrm{II}}^{(m)} = 10^{-4}$ and $C_{\mathrm{I}}^{(m)} = 10^{-6}$, $C_{\mathrm{II}}^{(m)} = 10^{-4}$.

A parametric study is further conducted on the relative fatigue sensitivity of mode-I and mode-

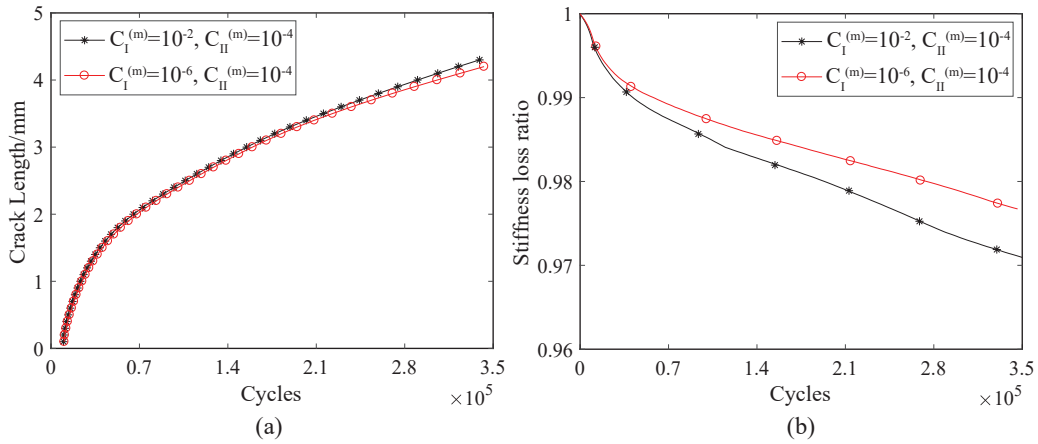

Figure 3.12: (a) Splitting crack propagation, and (b) residual stiffness as a function of cycle numbers for $[90°/0°]_S$ laminates compared between $C_{\mathrm{I}}^{(m)} = 0.01$, $C_{\mathrm{II}}^{(m)} = 10^{-4}$ and $C_{\mathrm{I}}^{(m)} = 10^{-6}$, $C_{\mathrm{II}}^{(m)} = 10^{-4}$.

II damage growth rates, and its consequences on specimen level damage evolution in the context of open-hole cross-ply laminate configurations. In this manuscript, the mode sensitivity is demonstrated by varying the fatigue amplitude parameters (i.e. $C_{\mathrm{I}}^{(m)}$ and $C_{\mathrm{II}}^{(m)}$), which affect the fatigue behavior, but not the static response. Other parameters such as the cohesive strength are expected to show similar influences. In this case, the amplitude parameter $C_{\mathrm{I}}^{(m)}$ that controls fatigue evolution (of "transverse matrix cracking" and "delamination" fatigue paths) under mode-I condition is reduced from 10^{-2} to 10^{-6}, while $C_{\mathrm{II}}^{(m)}$ and the rest of the parameters remain the same. This choice of the parameter effectively reduces the sensitivity of cyclic propagation of mode-I crack. The structural mesh is discretized with the element size of h=0.1mm. Figure 3.11 makes the comparison of predicted damage contours between $C_{\mathrm{I}}^{(m)} = 10^{-2}$ and $C_{\mathrm{I}}^{(m)} = 10^{-6}$ at 320,000 cycles. The splitting crack in the $0°$ ply, the interlaminar damage in the delamination layer, as well as the diffuse damage in $90°$ ply for $C_{\mathrm{I}}^{(m)} = 10^{-6}$ remain unchanged, but no discrete transverse cracks are observed. As shown in Fig. 3.12, the absence of transverse cracks does not have a significant influence on splitting crack extension, but reduces the stiffness loss steadily as the cyclic loading continues.

The differences in behavior is further illustrated by studying mode-I and mode-II fatigue damage evolution. Figure 3.13a compares the pure-mode fatigue damage evolution rate $\mathrm{d}\omega_f/\mathrm{d}t$ as a function of dimensionless equivalent separation ν/ν_u between $C_{\mathrm{I}}^{(m)} = 10^{-6}$ and $C_{\mathrm{I}}^{(m)} = 10^{-2}$. The figure

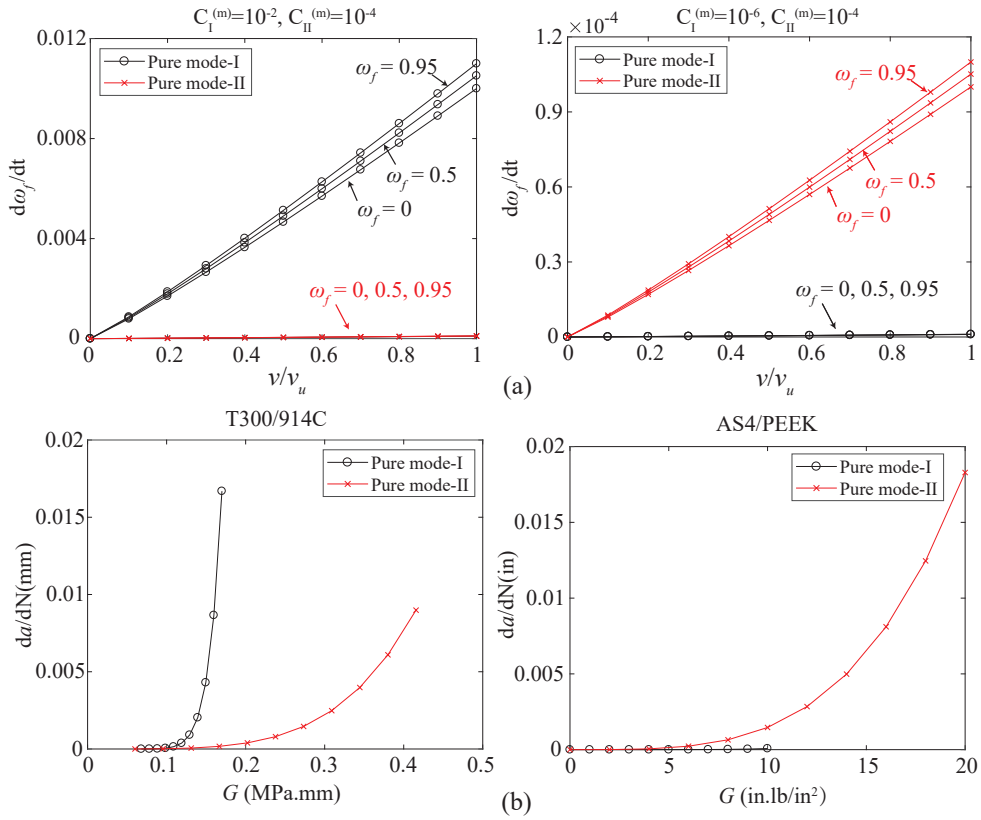

Figure 3.13: Pure mode fatigue damage evolution rate $\mathrm{d}\omega_f/\mathrm{d}t$ vs. dimensionless equivalent separation ν/ν_u for $C_{\mathrm{I}}^{(m)} = 0.01$, $C_{\mathrm{II}}^{(m)} = 10^{-4}$ (left) and $C_{\mathrm{I}}^{(m)} = 10^{-6}$, $C_{\mathrm{II}}^{(m)} = 10^{-4}$ (right) (b) Crack propagation rate $\mathrm{d}a/\mathrm{d}N$ vs. strain-energy release rate G for fiber-epoxy T300/914C (left) and AS4/PEEK (right) composites.

plots Eqs. 3.7, 3.8, 3.9 with the respective material parameters. In the case of $C_I^{(m)} = 10^{-6}$, the pure mode-I fatigue degradation is orders of magnitude smaller than mode-II failure, whereas the opposite conclusion is reached for the case of $C_{\mathrm{I}}^{(m)} = 10^{-2}$. Noting that the transverse and the splitting cracks are respectively mode-I and mode-II dominated, setting $C_{\mathrm{I}}^{(m)} = 10^{-6}$ results in a much smaller transverse crack growth rate compared to the splitting crack. Conversely, setting $C_{\mathrm{I}}^{(m)} = 10^{-2}$ enhances transverse crack propagation and more interaction with the growing splitting crack

The two distinctly different behaviors have also been observed in experiments that use similar laminate configurations but different types of materials for matrix constituents. According to the experiments conducted by Spearing et al. [130], T300/914C laminates subjected to high-fatigue cyclic loading shows long extension of transverse cracks, which are almost negligible in AS4/PEEK

laminates observed by Wang et al. [132]. Figure 3.13b shows the typical fatigue crack growth rate curves for T300/914C and AS4/PEEK composite systems. The curves are generated by assuming that the fatigue crack propagation follows the Paris law with parameters calibrated using double cantilever beam and end notch flexure tests [133, 134]. The switch between mode I and mode II fatigue sensitivity observed for the thermoset and thermoplastic systems and the experimentally observed damage propagation behavior are qualitatively in agreement with the trends shown in the parametric study.

3.5 Conclusion

This chapter integrates temporal multiscale modeling and an adaptive time step selection strategy to MDDT model and achieves high computational efficiency. The investigation also shows that energy regularization based on element size could be ineffective for fatigue damage accumulation unless specific forms of fatigue damage evolution laws are considered. In particular, fatigue damage laws must (a) include softening behavior to eliminate stress state singularities at the crack tip and (b) dissipate fatigue fracture energy in the softening regime for effective energy regularization. The numerical experiments using single lamina and open-hole laminate configurations subjected to high-fatigue tensile loading verify the mesh-size insensitivity in terms of damage growth, crack propagation as well as specimen stiffness evolution. For cross-ply laminates, simultaneous growth of splitting, delamination and transverse matrix cracks, and their growing patterns predicted by the proposed model agree well with experimental results. Furthermore, differences between the fatigue damage growth patterns observed in some thermoset and thermoplastic resins is explained based on the relative fatigue resistances against mode I and mode II fatigue crack growth.

3.6 Appendix

Figure 3.14 provides the summary of the system of equations for microchronological and macrochronological problems. The equations of the two scale problems have the same form, but the response fields are expressed in terms of different time scale coordinates. t represents macrochronological time resolving the whole structure life, where $t \in [0, t_{\mathrm{f}}]$. τ stands for microchorological time coordinates defined within the unit cyclic loading, where $\tau \in [0, \tau_0]$. The response field in macrochronological problem is homogenized using fixed-point operator: $\widetilde{\phi}(t) = \phi(t, \tau_0)$ [68]. In this work, the

fixed point is chosen at the end of microchronological step.

Microchronological problem ($\tau \in [0, \tau_0]$)

Given: macroscopic strain $\bar{\boldsymbol{\epsilon}}(t, \tau)$, coicide with microchronological time t; cohesive law and associated parameters;

Compute: microchronogical separation $\boldsymbol{\delta}^{(\alpha)}(t, \tau)$, microchronogical stress $\bar{\boldsymbol{\sigma}}(\mathbf{x}, t, \tau)$

Equilibrium equation:

$$\nabla \cdot \bar{\boldsymbol{\sigma}}(\mathbf{x}, t, \tau) + \mathbf{b}(\mathbf{x}) = 0$$

Microstructural equlibrium equation:

$$\mathbf{t}^{(\alpha)}(t, \tau) - \mathbf{C}^{(\alpha)} : \bar{\boldsymbol{\epsilon}}(t, \tau) + \sum_{\beta=1}^{m} \mathbf{D}^{(\alpha\beta)} \cdot \boldsymbol{\delta}^{(\beta)}(t, \tau) = \mathbf{0}$$

Cohesive behavior:

$$\mathbf{t}^{(\alpha)}(t, \tau) = [1 - \omega^{(\alpha)}(t, \tau)]\mathbf{K}^{(\alpha)} \cdot \boldsymbol{\delta}^{(\alpha)}(t, \tau)$$

Constitutive relationship:

$$\bar{\boldsymbol{\sigma}}(t, \tau) = \bar{\mathbf{L}} : \bar{\boldsymbol{\epsilon}}(t, \tau) + \sum_{\alpha=1}^{m} \mathbf{Z}^{(\alpha)} \cdot \boldsymbol{\delta}^{(\alpha)}(t, \tau)$$

Macrochronological problem ($t \in [0, t_{\mathrm{f}}]$)

Given: macroscopic strain $\bar{\boldsymbol{\epsilon}}(t)$; cohesive law and associated parameters;

Compute: temporal homogenized separation $\widetilde{\boldsymbol{\delta}}^{(\alpha)}(t)$, temporal homogenized stress $\widetilde{\bar{\boldsymbol{\sigma}}}(\mathbf{x}, t)$

Equilibrium equation:

$$\nabla \cdot \widetilde{\bar{\boldsymbol{\sigma}}}(\mathbf{x}, t) + \mathbf{b}(\mathbf{x}); \quad \mathbf{x} \in \Omega; \quad \tau \in [0, \tau_0]$$

Microstructural equlibrium equation:

$$\widetilde{\mathbf{t}}^{(\alpha)}(t) - \mathbf{C}^{(\alpha)} : \widetilde{\bar{\boldsymbol{\epsilon}}}(t) + \sum_{\beta=1}^{m} \mathbf{D}^{(\alpha\beta)} \cdot \widetilde{\boldsymbol{\delta}}^{(\beta)}(t) = \mathbf{0}$$

Cohesive law:

$$\widetilde{\mathbf{t}}^{(\alpha)}(t) = [1 - \widetilde{\omega}^{(\alpha)}(t)]\mathbf{K}^{(\alpha)} \cdot \widetilde{\boldsymbol{\delta}}^{(\alpha)}(t)$$

Constitutive relationship:

$$\widetilde{\bar{\boldsymbol{\sigma}}}(t) = \bar{\mathbf{L}} : \widetilde{\bar{\boldsymbol{\epsilon}}}(t) + \sum_{\alpha=1}^{m} \mathbf{Z}^{(\alpha)} \cdot \widetilde{\boldsymbol{\delta}}^{(\alpha)}(t)$$

Figure 3.14: Summary of microchronological and macrochronological problems based on temporal multiscale scheme.

Temporal local periodicity is not feasible in the microchronological problem due to the presence of irreversible damage condition. Therefore, almost periodicity is introduced for fatigue damage by allowing small value change within the microchronological time domain [68]. The derivative of temporal homogenized fatigue damage in the macrochronological problem is then expressed as follows according to the chain rule:

$$\widetilde{\omega}_{f,t}^{(\alpha)}(t) = f(\boldsymbol{\delta}^{(\alpha)}, \dot{\boldsymbol{\delta}}^{(\alpha)}) + \dot{\omega}_{f-\mathrm{ap}}^{(\alpha)}(t) \tag{3.11}$$

where $f(\boldsymbol{\delta}^{(\alpha)}, \dot{\boldsymbol{\delta}}^{(\alpha)})$ stands for partial derivative of damage with respect to the coarse time scale t, $\dot{\omega}_{f-\mathrm{ap}}^{(\alpha)}(t)$ is the almost periodicity variable expressed as:

$$\dot{\omega}_{f-\mathrm{ap}}^{(\alpha)}(t) = \frac{1}{\tau_0}(\omega_f^{(\alpha)}(t, \tau_0) - \omega_f^{(\alpha)}(t, 0)) \tag{3.12}$$

In adaptive macrochronological time stepping strategy, the time increment $\Delta t_i = t_{i+1} - t_i$ at

the i^{th} macrochronological step is determined by:

$$\Delta t_i = \frac{\Delta \omega_p}{\|\boldsymbol{\omega}'_f(t_i)\|_\infty} \tag{3.13}$$

where $\boldsymbol{\omega}'_f(t_i)$ is the vector consisting of $\dot{\omega}^{(\alpha)}_{f-\mathrm{ap}}(t)$, which is evaluated in the current micro-chronological load cycle associated with all the failure path at all integration points within the macroscopic discretized domain. $\Delta\omega_p$ stands for the tolerance parameter for allowable damage accumulation across the macro-chronological time step.

CHAPTER 4

ADAPTIVE MULTISCALE DISCRETE DAMAGE THEORY FOR RE-ORIENTED CRACK

4.1 Introduction

The idea of predefining and embedding failure paths with fixed orientations in the microstructure was shown to be effective for modeling failure mechanisms, where the crack directions are known a-priori such as splitting crack or transverse matrix cracking in the previous numerical examples. The orientations of such cracks are dictated by the direction of the lamination. However, such a strategy is not ideal for modeling cracks, for which the propagation direction is determined by the local stress state and the relative microstructure configuration. A straightforward approach is to pre-define a large number of potential failure paths with different orientations to cover possible cracking scenarios. The direction of crack propagation then naturally arises during the multiscale analysis as the direction of the failure path that fails first from among the finite choices of failure path orientations. This approach requires a high number of failure paths to be deployed to capture the failure behavior accurately (i.e., $m \gg 1$, m stands for total number of basis for all the failure paths). Since the resulting nonlinear system is dense, the computational cost of evaluating it is $O\left(m^3\right)$ [135], reducing the potential benefits of model order reduction. Another possible approach is to dynamically construct the reduced order model on the fly during the multiscale analysis, where a failure path is embedded in the microstructure model when a failure criterion is met. While this idea results in ROMs with small m, it requires a separate ROM construction (i.e., computation of influence functions and coefficient tensors) for each material point in the macroscopic domain, which is also computationally expensive.

This chapter proposes a different strategy by adaptively selecting the coarse basis approximation of failure at the microscale as opposed to predefining the cohesive surfaces, and leverage rotational invariances in the microstructure to very efficiently calculate the reduced-order model during the multiscale analysis. The performance as well as the restrictions of the model are assessed in the context of numerical microscale specimens subjected to multi-axial loading by comparing model predictions to direct numerical simulations. The proposed approach is then employed to model re-

oriented crack propagation in notched concrete beams under four point bending, and delamination migration in fiber-reinforced cross-ply composite laminates. These two cases have been experimentally investigated in Ref. [136, 137].

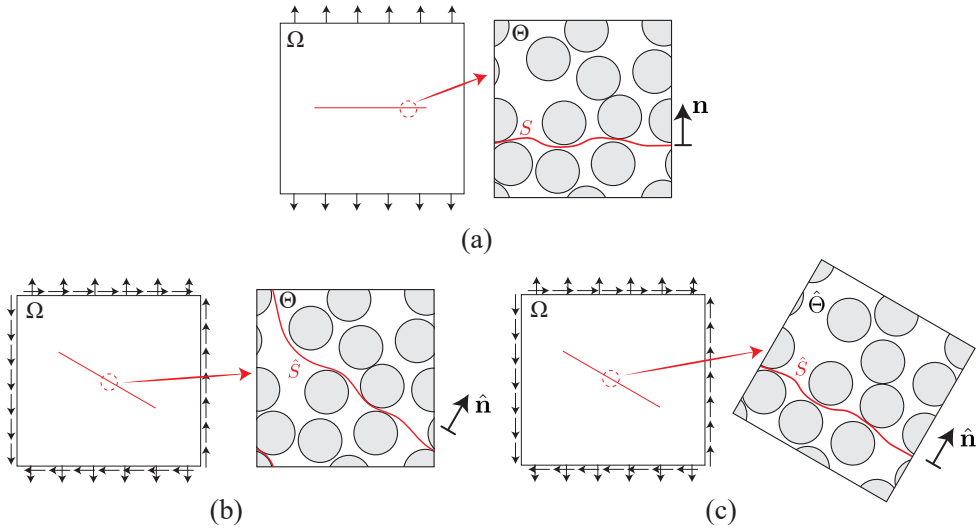

Figure 4.1: Schematic illustration of different multiscale modeling strategies: (a) The microstructure and a predefined failure path; (b) the same microstructure with rotated failure path orientation; and (c) the rotated microstructure and the failure path adopted in this manuscript.

4.2 Adaptivity of Potential Failure Path

4.2.1 Effective Rotation of Microstructure

The adaptive methodology for a specific subset of microcracks under the effects of load orientation is schematically illustrated in Fig. 4.1. Consider a reduced order model $\Re_{\Theta,S} = \{\mathbf{C}, \mathbf{D}, \mathbf{Z}\}$ of a microstructure, Θ, that induces a failure path, S with known orientation, $\mathbf{n}$ as shown in Fig. 4.1a. The failure path is considered to be aligned with a plane of statistical isotropy (i.e., the probability distributions describing the geometry are rotationally invariant, and that the microstructure is periodic, such as a hexagonal close-packed microstructure). It is then trivial to show that another ROM defined over the same microstructure but with a different failure path, $\hat{\Re}_{\Theta,\hat{S}} = \{\hat{\mathbf{C}}, \hat{\mathbf{D}}, \hat{\mathbf{Z}}\}$ shown in Fig. 4.1b is identical to the original model that undergoes a rigid body rotation, $\hat{\Re}_{\hat{\Theta},\hat{S}} = \{\hat{\mathbf{C}}, \hat{\mathbf{D}}, \hat{\mathbf{Z}}\}$ shown in Fig. 4.1c. The periodic boundary conditions are not affected by this rigid body rotation. The result implies that provided that a "reference" model with a known crack orientation is available, the reduced order model with any orientation with respect to the invariant plane could be

constructed by simple tensor rotation operations. The transformation relationships are expressed as:

$$\begin{aligned} \hat{C}_{ijk} &= R_{mi}R_{nj}R_{rk}C_{mnr} \\ \hat{D}_{ij} = R_{mi}R_{nj}D_{mn} \quad \hat{Z}_{ijk} &= R_{mi}R_{nj}R_{rk}Z_{mnr} \end{aligned} \tag{4.1}$$

where $\mathbf{R}$ represents the transformation tensor under rotation. In random heterogeneous materials, such as isotropic concrete or particulate composites, the transformation tensor requires three Euler angles to describe the rotation. Since this manuscript focuses on long continuous fiber-reinforced composites, such a strategy is applicable to the matrix failure path whose crack plane is presumed to be parallel to the fiber direction (z-direction in Fig. 4.1). The transformation tensor can be then expressed as the angle of microstructural rotation θ in the transverse plane:

$$[\mathbf{R}(\theta)] = [\cos(\theta), -\sin(\theta), 0; \sin(\theta), \cos(\theta), 0; 0, 0, 1] \tag{4.2}$$

4.2.2 Identification of Crack Orientation

The identification criterion for crack nucleation and its orientation is proposed based on cohesive states in the failure path embedded in the microstructure after rotation. The simple traction-separation relationship in Eq. 2.32 and classic bilinear law (see Eq. 3.1) are adopted in this chapter. Before nucleation (i.e. $\kappa < \nu_c$), the traction variable $\mathbf{t}$ in the potential failure path is expressed as a function of the rotation angle θ based on Eqs. 2.14 and 3.1:

$$\mathbf{t}(\theta) = \mathbf{K} \cdot [\mathbf{K} + \hat{\mathbf{D}}(\theta)]^{-1} \cdot \hat{\mathbf{C}}(\theta) : \bar{\boldsymbol{\epsilon}} \tag{4.3}$$

As shown in Fig. 4.2a, the traction state for different failure path orientations form an ellipsoid in the traction (t_N-t_T) space, where t_T represents the magnitude of the tangential traction: $t_T = \sqrt{t_{S1}^2 + t_{S2}^2}$. The crack initiation envelop is defined by quadratic failure initiation criterion:

$$g = \left(\frac{\langle t_N \rangle}{t_{u_{\mathrm{I}}}}\right)^2 + \left(\frac{t_{S1}}{t_{u_{\mathrm{II}}}}\right)^2 + \left(\frac{t_{S2}}{t_{u_{\mathrm{II}}}}\right)^2 - 1 = 0 \tag{4.4}$$

which represents the peak strength as a function of mode-mixity. The intercept with horizontal and vertical axis respectively indicates pure mode-I condition: $t_N = t_{u_{\mathrm{I}}}$ and pure mode-II condition:

$t_T = t_{u\mathrm{II}}$. The encompassed region within the failure envelop defines the admissible traction states. The crack nucleates when the traction variable satisfies the failure criterion, denoted by the contact point between the traction curve and the initiation envelop. The failure path orientation at the contact point yields the nucleation direction θ_c, which satisfies:

$$\begin{cases} \mathbf{t}(\theta_c) = \mathbf{K} \cdot [\mathbf{K} + \hat{\mathbf{D}}(\theta_c)]^{-1} \cdot \hat{\mathbf{C}}(\theta_c) : \bar{\boldsymbol{\epsilon}} \\ g\big(t_N(\theta_c), t_T(\theta_c)\big) = 0 \end{cases} \tag{4.5}$$

while $g\big(t_N(\theta), t_T(\theta)\big) < 0$ if $\theta \neq \theta_c$.

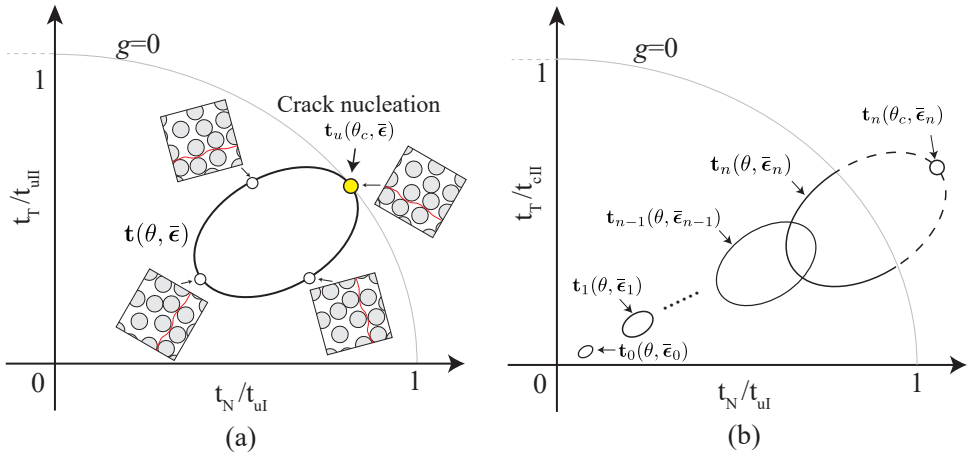

Figure 4.2: Schematic illustration of identification criterion for nucleation direction in the normal-tangential traction space: (a) Nucleation direction θ_c denoted by the contact point between the traction state (black curve) and failure envelop $g = 0$ (light grey curve); (b) Nucleation direction defined in the trial state (black dash curve) which maximizes the criterion function g under discretized loading.

In the numerical implementation of this methodology using an incremental scheme, identification of the exact contact point is not always possible. Consider that the microstructure is subjected to the macroscopic strain $\bar{\boldsymbol{\epsilon}}_n$ at time t_n within a discretized loading history $\{\bar{\boldsymbol{\epsilon}}_0, \bar{\boldsymbol{\epsilon}}_1, \ldots \bar{\boldsymbol{\epsilon}}_n \ \ldots\}$. At t_n, a trial traction curve is defined that crosses into the initiation envelop, indicating that the softening stage is reached for a certain range of failure path orientations (indicated by the dashed portion of the curve in Fig. 4.2b). Since the traction curve in the previous increment remains within the initiation envelop, the failure path orientation needs to be identified at the current increment. Here, the nucleation direction is approximated by the failure path orientation that maximizes the criterion

function g, which is computed by the elastic trial traction $\hat{\mathbf{t}}$. The trial traction is evaluated based on Eq. 4.3, assuming that the cohesive state is in hardening stage. The expression of the nucleation direction is:

$$\theta_c = \arg\max_{\theta} g\big(\hat{\mathbf{t}}(\theta)\big) \tag{4.6}$$

4.2.3 Numerical Implementation

The procedure for evaluation of the reduced order microscale problem consists of the following steps:

At initialization, assign the indicator $\mathrm{NUCLEATED} \leftarrow 0$ at each quadrature point indicating that the crack is not initiated. Assign the reduced order model at each quadrature point to be the reference reduced order model: $\Re^{\mathrm{curr}} \leftarrow \Re_{\Theta,S}$.

During the multiscale simulation at a given increment, n at an arbitrary quadrature point, the macroscopic update procedure is as follows:

1. Update the homogenized strain: $\bar{\boldsymbol{\epsilon}}_n = \bar{\boldsymbol{\epsilon}}_{n-1} + \Delta\bar{\boldsymbol{\epsilon}}$.

2. If $\mathrm{NUCLEATED} = 0$:

   2a. Solve the optimization problem:

   $$\min_{\theta} -g\big(\hat{\mathbf{t}}(\theta)\big),\ \theta \in [0, \pi] \tag{4.7}$$

   where the trial traction variable is:

   $$\hat{\mathbf{t}}(\theta) = \mathbf{K} \cdot [\mathbf{K} + \hat{\mathbf{D}}(\theta)]^{-1} \cdot \hat{\mathbf{C}}(\theta) : \bar{\boldsymbol{\epsilon}}_n \tag{4.8}$$

   The trial failure path orientation is computed as the outcome of the optimization problem:

   $$\hat{\theta} = \arg\max_{\theta} g\big(\hat{\mathbf{t}}(\theta)\big) \tag{4.9}$$

   2b. If $g\big(\hat{\mathbf{t}}(\hat{\theta})\big) \geq 0$, the crack is initiated.

   2b.1 Assign the indicator $\mathrm{NUCLEATED} \leftarrow 1$ and the nucleation orientation $\theta_c \leftarrow \hat{\theta}$.

   2b.2 Compute trial rotation matrix $\hat{\mathbf{R}}$ using Eq. 4.2 with the nucleation orientation θ_c.

2b.3 Compute rotated reduced order model $\hat{\Re}_{\hat{\Theta},\hat{S}} = \{\hat{\mathbf{C}}, \hat{\mathbf{D}}, \hat{\mathbf{Z}}\}$ using the rotation transformation defined in Eq. 4.1.

2b.4 Assign $\Re^{\text{curr}} \leftarrow \hat{\Re}_{\hat{\Theta},\hat{S}}$

3. Compute reduced order traction variables $\mathbf{t}_n^{(\alpha)}$, separation variables $\boldsymbol{\delta}_n^{(\alpha)}$ and current damage state $\omega_n^{(\alpha)}$ by simultaneously solving Eqs. 2.14,2.9 and 3.1 using $\Re^{\text{curr}}$.

4. Update the macroscopic stress $\bar{\boldsymbol{\sigma}}_n$ using Eq. 2.21.

At step 2a, the optimization problem in Eq. 4.7 is solved using the golden section search approach [138]. It is a robust gradient-free numerical method for finding the minimum of an one-dimensional convex function on the specified interval by successively narrowing the range of the parameter (i.e., θ) using the golden ratio. At step 3, the governing system of equations in the reduced-order model (Eqs. 2.14,2.32 and 3.1) is evaluated using the Newton-Raphson method.

4.3 Unit Cell Analysis

A series of unit cell analyses is performed to verify the adaptive MDDT model in capturing the failure behavior at the microscopic scale under multiaxial loading conditions. The microstructure configuration is shown in Fig. 4.3a. The fiber volume fraction is 28 %, and the fiber is aligned with the z direction. The hexagonal fiber arrangement ensures that the microstructure is rotationally invariant in the transverse (x-y) plane. The reference failure path for matrix cracking resides within the matrix constituent and wraps around the fiber. The average unit normal $\mathbf{n}$ of the failure path is parallel to the y-axis in the global coordinates. Elastic properties of the isotropic matrix and transversely isotropic fiber, and the fracture properties of matrix cracking failure path are listed in Table 4.1.

The macroscopic specimen and its boundary conditions are displayed in Fig. 4.3c. The specimen is restrained in fiber (z) direction in order to approximate plane strain conditions. In the following examples, three different monotonic strain-controlled loadings are applied in the transverse plane x-y.

1. Combined tensile and simple shear loading: $\bar{\gamma}_{xy} = 2\bar{\epsilon}_{yy} > 0$.

2. Simple shear loading: $\bar{\gamma}_{xy} > 0$.

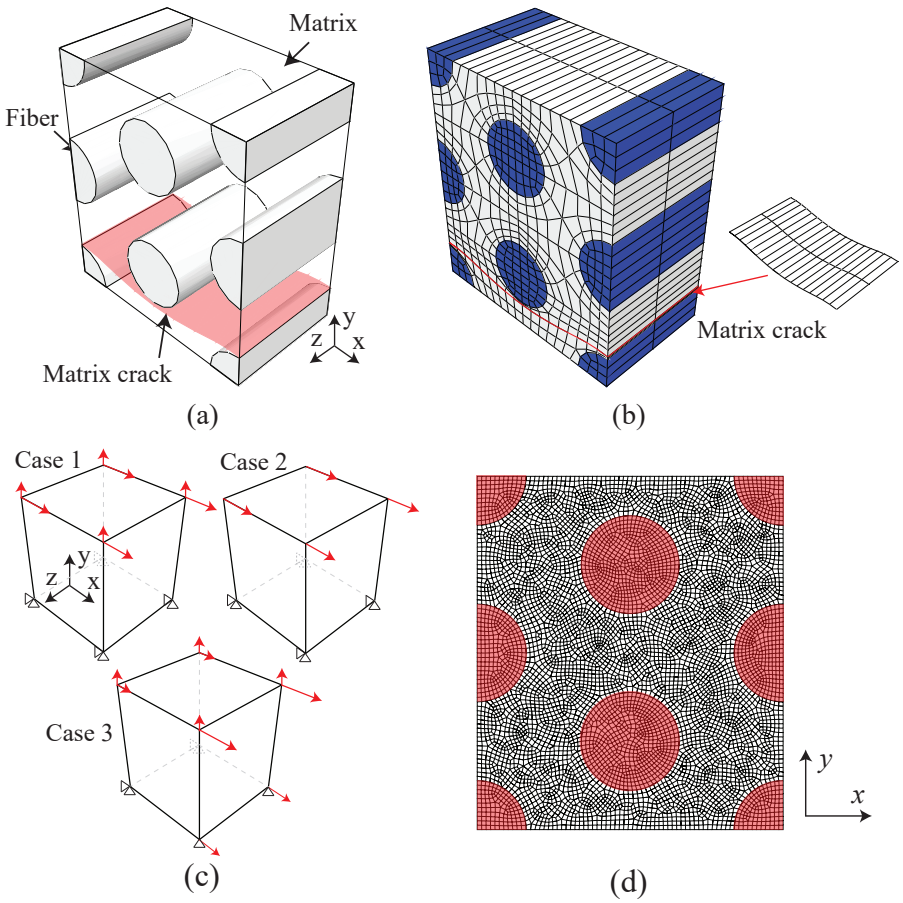

Figure 4.3: (a) The hexagonal microstructure embedded with the failure path for matrix cracking. (b) Discretizations of the microstructure and failure path. (c) The macroscopic domain as well as the loading and boundary conditions for the unit cell tests using MDDT model. (d) Geometry and discretization of the 2D specimen for direct numerical simulations.

3. Combined biaxial tensile and simple shear loading: $\bar{\gamma}_{xy} = \bar{\epsilon}_{yy} = 0.625\bar{\epsilon}_{xx} > 0$.

The accuracy characteristics of the proposed model are compared with the reference direct numerical simulations (DNS) which resolve the microstructure and employ cohesive zone modeling (CZM) to track nucleation and propagation of the cracks. Because modeling 3D CZM is computationally expensive, the specimen for DNS is considered to be two-dimensional under plane strain condition. Two hexagonal unit cells form the domain for visual clarity of crack formation. The periodic boundary conditions are respectively applied to the DNS specimen for the three loading

cases as shown in the following equations:

$$\begin{aligned}\mathbf{u}(x, L_y, z) - \mathbf{u}(x, 0, z) &= (\bar{\gamma}_{xy}\mathbf{i} + \bar{\epsilon}_{yy}\mathbf{j})\, L_y \\ \mathbf{u}(0, y, z) - \mathbf{u}(L_x, y, z) &= \bar{\gamma}_{xy} L_x \mathbf{j}\end{aligned} \tag{4.10}$$

$$\begin{aligned}\mathbf{u}(x, L_y, z) - \mathbf{u}(x, 0, z) &= \bar{\gamma}_{xy} L_y \mathbf{i} \\ \mathbf{u}(0, y, z) - \mathbf{u}(L_x, y, z) &= \bar{\gamma}_{xy} L_x \mathbf{j}\end{aligned} \tag{4.11}$$

$$\begin{aligned}\mathbf{u}(x, L_y, z) - \mathbf{u}(x, 0, z) &= (\bar{\gamma}_{xy}\mathbf{i} + \bar{\epsilon}_{yy}\mathbf{j})\, L_y \\ \mathbf{u}(0, y, z) - \mathbf{u}(L_x, y, z) &= (\bar{\epsilon}_{xx} + \bar{\gamma}_{xy}\mathbf{j})\, L_x\end{aligned} \tag{4.12}$$

where L_x, L_y, L_z respectively stand for the edge length at x, y, z directions, $0 \leq x \leq L_x$, $0 \leq y \leq L_y$, $0 \leq z \leq L_z$, $\mathbf{i}, \mathbf{j}$ are unit vectors consistent with global coordinate directions. The DNS domain is discretized with 4-noded bilinear quadrilateral elements (Fig. 4.3d). COH2D4 elements from ABAQUS cohesive element library are inserted to each face of every element within the matrix phase and the matrix-fiber interface. As the results below indicate, we do not observe a significant artificial compliance effect in the response due to the presence of cohesive elements along all solid element edges. The cohesive stiffness is set to 6×10^4 GPa/mm.

The simulations are run on an Intel Xeon Gold 6130 workstation with 16 cores, 2.10 GHz and 192 GB RAM. The proposed model uses single core for the simulations and the wallclock time for computation is 3s, orders of magnitude faster compared to DNS, which spends respectively 13,901s, 99,729s, 10,387s for the three cases using 16 cores with parallel computing.

The orientation of the reference failure path is set as $\theta = 0$. Positive θ represents counter-clockwise rotation of the microstructure. Figure 4.4 shows the comparison of the simulation results as computed using the DNS and the proposed multiscale simulations. The crack orientations (i.e. nucleation direction) obtained by the adaptive MDDT model are respectively $150^\circ, 135^\circ, 120^\circ$ under the three loading cases. The first column of the figure shows the crack patterns predicted by DNS. In each case, a distinct crack forms within the microstructure, along with some additional damage that occurs prior to the onset of the dominant microcrack. The second column of the figure shows the traces of the dominant microcrack as the cohesive elements that has undergone full decohesion. The overall crack orientations observed in DNS show good agreement with the MDDT model pre-

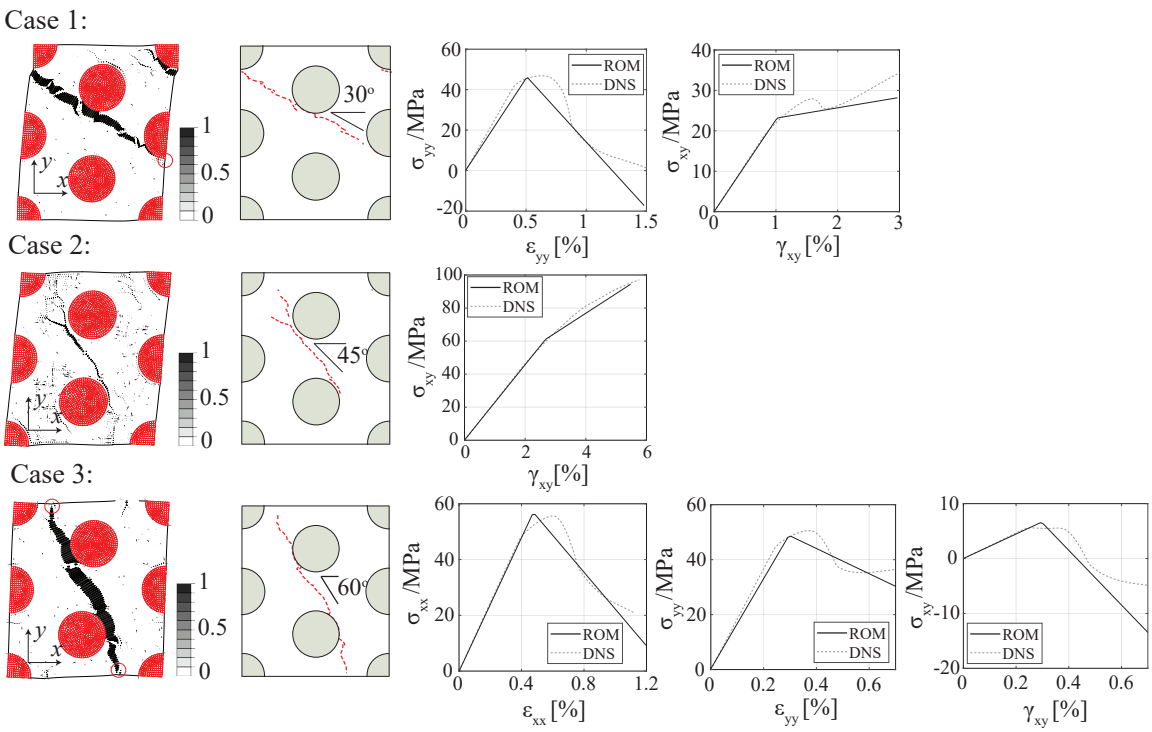

Figure 4.4: Damage contours and crack paths in direct micro-mechanical numerical simulations, and comparison of stress-strain responses between MDDT model and direct numerical simulation under the strain loading conditions of case (1): $\bar{\gamma}_{xy} = 2\bar{\epsilon}_{yy} = 3\%$, case (2): $\bar{\gamma}_{xy} = 6\%$, and case (3) $\bar{\gamma}_{xy} = \bar{\epsilon}_{yy} = 0.625\bar{\epsilon}_{xx} = 0.7\%$.

dictions. Figure 4.4 also displays the comparison of overall stress-strain responses between adaptive MDDT and DNS. A reasonable overall agreement is observed between the proposed reduced order model and the DNS from the aspects of peak strength and the trends of stress evolution after the peak strength. The overall shear stress-strain curves for Case 2 predicted by both the multiscale and the DNS simulations do not show a softening behavior due to the imposed boundary conditions. The boundary effects associated with periodicity constraints also cause some stress oscillations in the DNS simulations. Crack propagation is slightly disrupted when the dominant crack reaches the domain boundaries. An increase in tangent stiffness accompanied by a slight shift of the crack (circled in Fig. 4.4) as it propagates across the domain boundary. Furthermore, the proximity to fiber along the path of the microcrack results in some fluctuation of the slope of the overall stress-strain behavior in the DNS. These effects are not resolved in the multiscale model, as the MDDT model presumes uniform damage evolution within the failure path. A higher order MDDT model that resolves the crack growth within the microstructure could provide a more accurate match with

the DNS. This could be achieved by considering multiple reduced order basis functions per failure path. This extension is nontrivial since separation field continuity along the failure path may need to be satisfied, and hence beyond the scope of this chapter.

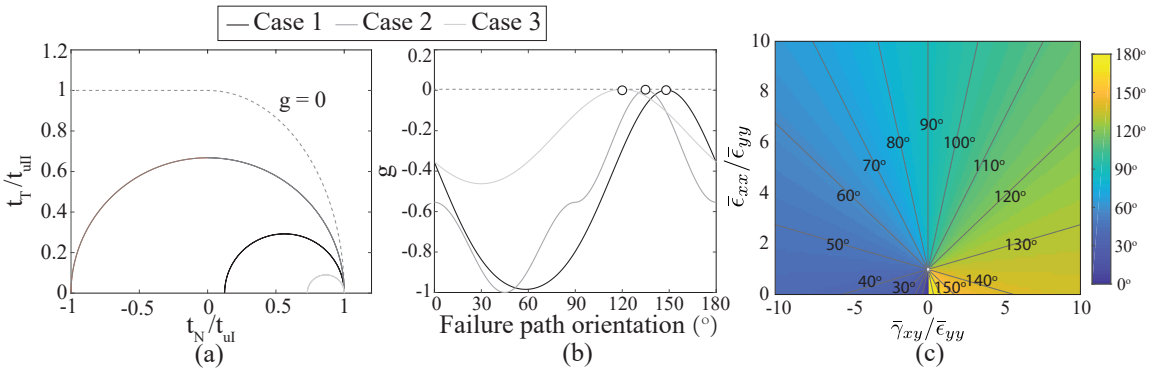

Figure 4.5: (a) The traction states in t_N-t_T space when reaching the initiation envelop under the strain loading conditions in the transverse plane. (b) The corresponding criterion function as a function of traction states at a given orientation. (c) Contours of crack orientation under multi-axial strain loading conditions within the transverse plane.

Table 4.1: Material properties of the composite constituents

Elastic properties of matrix$^{(m)}$ and fiber$^{(f)}$						
$E^{(m)}$	$\nu^{(m)}$	$E_1^{(f)}$	$E_2^{(f)}$	$G_{12}^{(f)}$	$G_{13}^{(f)}$	$\nu_{31}^{(f)}$
[GPa]		[GPa]	[GPa]	[GPa]	[GPa]	
4.67	0.34	280	17	5.67	30	0.3
Fracture parameters of matrix cracking for unit cell analysis						
G_{Ic}	G_{IIc}	t_{uI}	t_{uII}	K	η	
[MPa mm]	[MPa mm]	[MPa]	[MPa]	[MPa mm^{-1}]		
0.006	0.06	60	90	6×10^7	2.1	

4.3.1 Crack Orientation and Failure Mode Analysis

This section presents the effect of multiaxial strain-controlled loading on the orientation of the crack and the associated fracture mode. Here, the definition of crack nucleation orientation is adopted based on Eq. 4.5 (See Fig. 4.2a). Figure 4.5a,b shows the initiation conditions under three load configurations, Cases 1 to 3 as described above. In Fig. 4.5a, the critical traction states as a function of microcrack orientation at the point of failure initiation are shown by the elliptic curves in the traction space. Under pure shear or shear-tensile loading, the traction curves reach the initiation

envelop (shown as the $g = 0$ isocontour) at the horizontal axis, indicating that the interface is in pure mode-I condition. Figure 4.5b shows the criterion function as a function of traction states at a given orientation. For a given loading condition, the critical orientation at which microcrack forms corresponds to the orientation where the criterion function reaches 0. In Cases 1 to 3, the critical orientation is unique and equals to $150°, 135°, 120°$, respectively.

Next, the mode of failure and microcrack orientation is further investigated under more general loading conditions. Figure 4.5c displays the overall crack orientation pattern as a function of multiaxial loading in the transverse plane (x-y plane). The x-axis of the contour stands for the ratio between shear and tensile strain component $\bar{\gamma}_{xy}/\bar{\epsilon}_{yy}$, while y-axis stands for the ratio between the two normal strain components $\bar{\epsilon}_{xx}/\bar{\epsilon}_{yy}$ (with $\bar{\epsilon}_{yy} > 0$). The contours in the figure are the isolines of crack orientation in $\bar{\gamma}_{xy}/\bar{\epsilon}_{yy}$ - $\bar{\epsilon}_{xx}/\bar{\epsilon}_{yy}$ space, satisfying $\bar{\epsilon}_{xx} - \bar{\epsilon}_{yy} + 2\cot 2\theta_c\, \bar{\gamma}_{xy} = 0$. The isolines set out from the point $\bar{\epsilon}_{xx} = \bar{\epsilon}_{yy}$, representing the pure hydrostatic state where the failure initiates at all directions at once. It is easy to verify that the isoline of crack orientation overlaps with the direction of maximum macroscopic principal stress, consistent with the classical failure criterion for brittle or quasi-brittle materials (see e.g. [76, 82]). In addition, all cracks represented in Fig. 4.5c initiate under mode-I conditions.

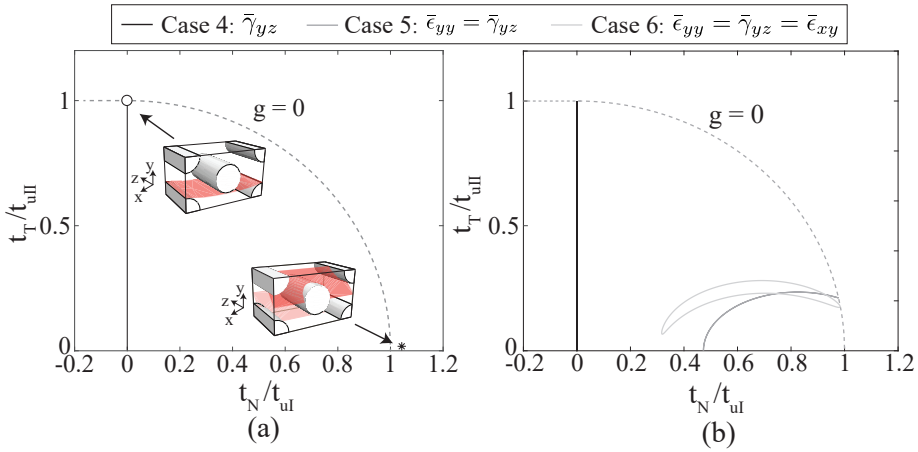

Figure 4.6: The traction states in t_N-t_T space (a) for the matrix failure paths parallel to fiber and $45°$ across the fiber under in-plane shear loading ($\bar{\gamma}_{yz}$) (b) for the matrix failure paths parallel to the fiber under combined tensile and in-plane shear loading.

Next, the failure initiation is investigated when the loading is not within the transverse plane. Figure 4.6a displays the traction state (denoted by solid line) for the failure initiation within the failure path parallel to the fiber (denoted as in-plane failure path) under the in-plane shear loading

(case 4: $\bar{\gamma}_{yz} > 0$). The traction reaches the initiation envelop under pure mode-II at the orientation of $\theta_c = 0^\circ$ (denoted by circle mark). Another traction state (denoted by star mark) is shown in Fig. 4.6a under the same loading but within the failure path which is 45° across the fiber (denoted as out-of-plane failure path), consistent with direction of maximum macroscopic principal stress. The traction is outside the initiation envelope under approximate mode-I condition, indicating that the mode-I crack initiates prior to the in-plane failure path which initiates under mode-II condition. It is also important to note that mode-I out-of-plane fracture occurs only slightly before a possible mode-II in-plane fracture. This indicates that both of the failure states are possible depending on the microscopic geometry and failure properties associated with mode-I and mode-II fracture. These two mechanisms have been experimentally observed and well known. The crack parallel to the fiber is a splitting crack which is commonly seen in the notched laminates subjected to tensile loading [139]. The crack crossed by the fiber indicates shear matrix cracks, which have been observed in the off-axis laminates under tension [140]. The cross-fiber fracture plane associated with the mode-I failure (star mark in Fig. 4.6) is not rotationally invariant, and therefore the adaptive strategy can only accurately capture the mode II in plane fracture case. A hybrid strategy is necessary to track both failure modes, where the adaptive strategy is used to track in-plane failure modes, whereas additional paths are a-priori inserted to capture behavior in non-invariant orientations.

Figure 4.6b displays the traction states within a in-plane failure path under the loadings of Cases 4-6. In Case 5, the combination of $\bar{\epsilon}_{yy}$ and $\bar{\gamma}_{yz}$ results in mixed-mode failure but the same nucleation direction as Case 4, $\theta_c = 0^\circ$. Case 6 represents a more complex situation as $\bar{\gamma}_{xy}$ is involved, in which the crack nucleates at tilted direction ($\theta_c = 158^\circ$) under mixed-mode condition.

4.4 Four-point Bending Beam Analysis

The proposed model is further verified by predicting the crack propagation in notched concrete beam specimens with four-point constraints. The numerical results are compared with the experiments described in Ref. [136]. Figure 4.7a shows the particle microstructure configuration employed for concrete. Statistical isotropy is ensured for the rotational plane within the microstructure in the three dimensional space. The volume fraction of aggregate particles is 32% and the radius of spherical idealized particles is 5 mm. The modulus of the aggregate and the cement are respectively 50 GPa and 34 GPa, and their Poisson's ratio are 0.2. The resulting homogenized modulus (38 GPa) and

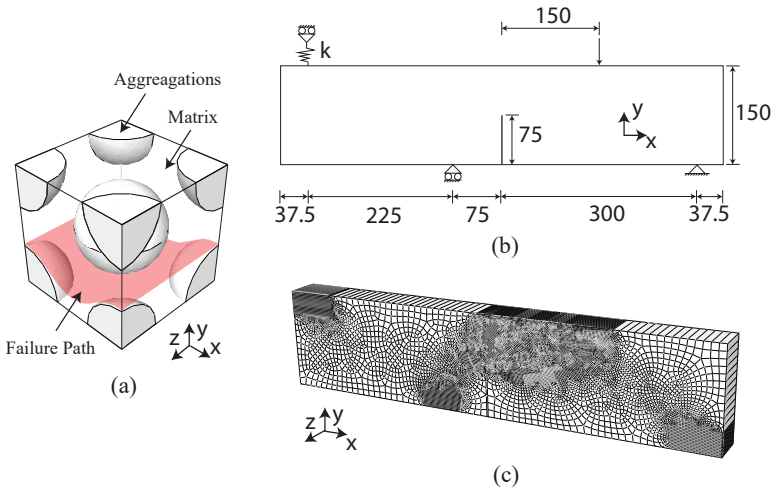

Figure 4.7: (a) Microstructure configuration of concrete material (b) Geometry and boundary conditions of four-points bending specimen test. (c) Numerical model and mesh discretizations.

Poisson's ratio (0.2) are consistent with the concrete properties in Ref. [136]. The tensile strength and fracture energy of the cement cracking failure path embedded in the particle microstructure are respectively 0.4 MPa and 0.06 MPa·mm for both mode-I and mode-II. Figure 4.7b shows the specimen geometry and boundary conditions. The thickness of the specimen in z-direction is 50 mm. A displacement-controlled loading is applied at the top (Fig. 4.7b). The numerical specimens are respectively restrained by two types of boundary conditions (named type-1 and type-2) which result in different crack trajectories. The vertical spring stiffness imposed at top left position is respectively set to be $k = 0$ (free boundary) and $k = \infty$ (vertical displacement restrained) for type-1 and type-2 boundary conditions. The rest of boundary conditions are the same in the two cases. Because no external loading is added along the out-of-plane direction (z direction), the particulate microstructure is considered to perform effective rotation only in x-y plane. Figure 4.7c displays the mesh discretization, wherein 8-noded tri-linear hexahedral elements are employed for discretization with reduced integration and hourglass control.

The numerical results of both type-1 and type-2 boundary conditions are shown in Fig. 4.8, wherein Fig. 4.8a displays the completely cracked elements (with damage variable $\omega = 1$) in the domain obtained by the proposed model. The macrocrack propagations in type-1 and 2 cases respectively reveal the direction towards 67° and 36° with respect to horizontal and overlap with experimental crack path envelop. Figure 4.8b displays the corresponding element-wise microscopic

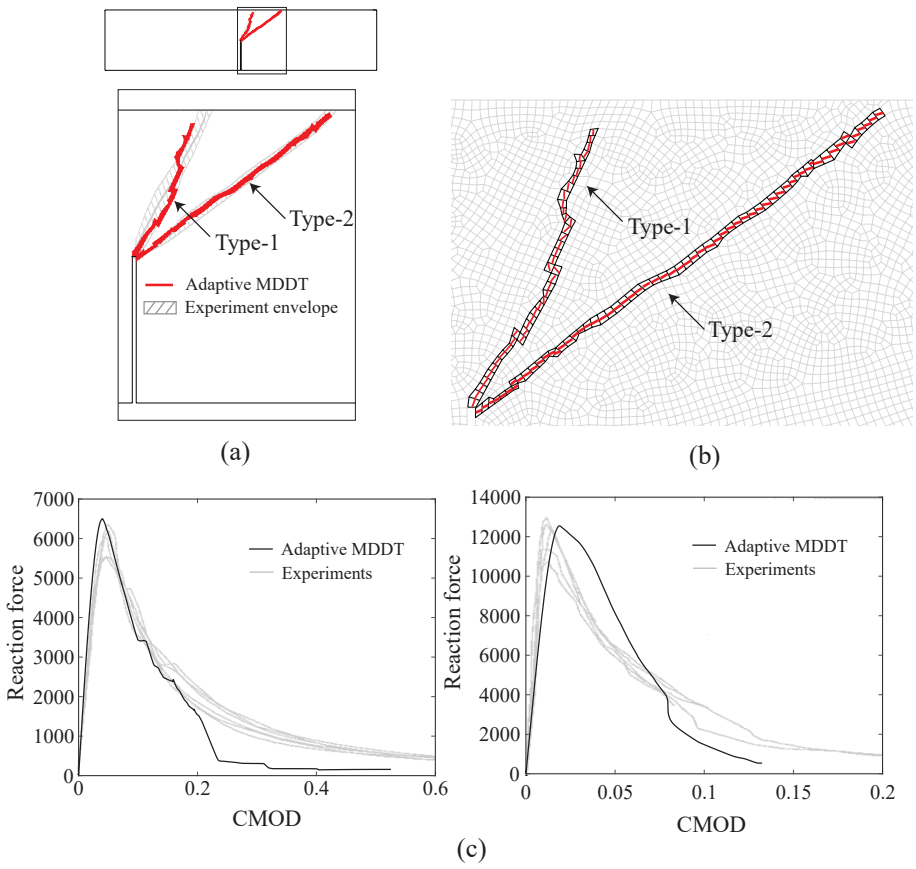

Figure 4.8: (a) Macrosopic crack path of type-1 and type-2 boundary conditions. (b) Element-wise microcrack orientation (denoted by direction of red line) for type-1,2 cases. (c) CMOD vs. reaction force at loading position for type-1 (left) and type-2 (right) cases.

crack orientation, denoted by direction of red lines within the mesh discretization. There is clearly an overall consistency of microcrack orientation with the trend of macrocrack propagation direction. Some deviations occur for type-2 case as crack growth approaches the top edge, wherein the mesh alignment obstructs macrocrack from following the microcrack orientation in a smaller angle (10° - 20°) with respect to horizontal. Figure 4.8c,d respectively show the responses of CMOD (i.e. crack mouth opening displacement) vs. reaction force at loading position for type-1 and type-2 case. Type-1 displays a very reasonable match with experiment results until a sudden drop of force response, which indicates the crack propagation near the top edge of the specimen. There is an overall agreement between type-2 case and experiments as well, also with a force drop as crack approaches the top of the specimen.

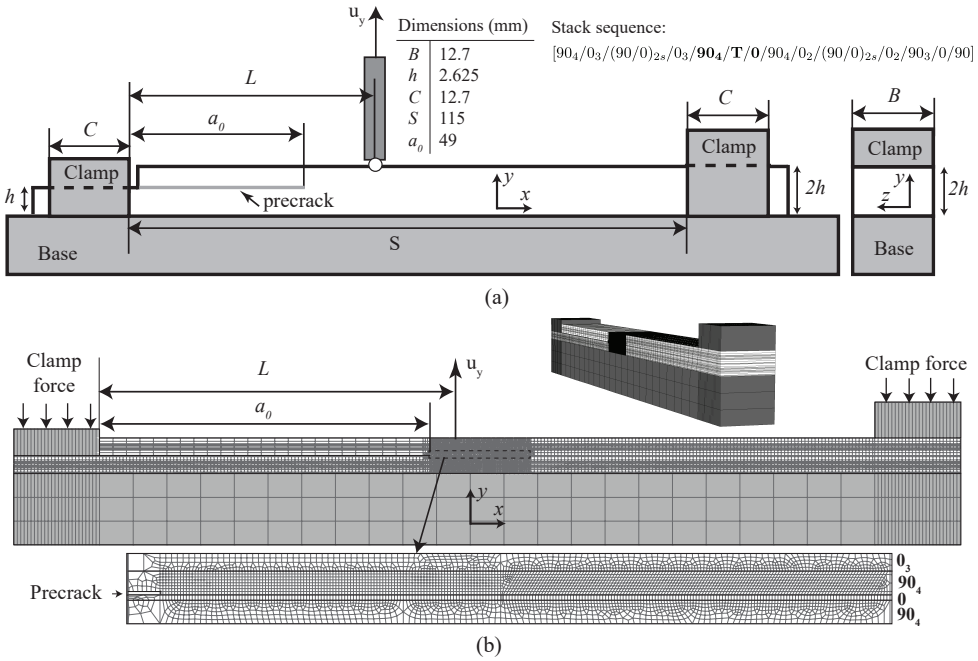

Figure 4.9: (a) Geometry sketch of cross-ply tape laminates in the delamination migration test. (b) Numerical model and mesh discretizations. Inset figure displays the structured mesh discretization for potential delamination propagation.

Table 4.2: Homogenized elastic moduli of the composite and fracture properties used in the delamination migration model

$E_{11} = E_{22}$	E_{33}	$G_{12} = G_{13}$	G_{23}	$\nu_{12} = \nu_{13}$	ν_{23}
[GPa]	[GPa]	[GPa]	[GPa]		
9	156	2.99	5.08	0.49	0.32
Fracture parameters of matrix cracking for unit cell analysis [128, 129]					
G_{Ic}	G_{IIc}	t_{uI}	t_{uII}	K	η
[MPa mm]	[MPa mm]	[MPa]	[MPa]	[MPa mm^{-1}]	
0.2	1	60	90	6×10^7	2.1

4.5 Delamination Migration Modeling

4.5.1 Numerical Model

The capabilities of the proposed reduced order multiscale model is further investigated in the context of delamination migration modeling using cross-ply laminates configuration and validated with a series of experiments [137]. The cross-ply specimens employed in this section were experimentally investigated in Ref. [137]. All constituent properties are identical to those used in the previous

section and listed in Table 4.1. Hexgonal packed microstructure with fiber volume fraction of 55% is employed in this section. The corresponding homogenized stiffness is consistent with IM7/8552 carbon fiber-epoxy composite [82, 141] and shown in Table 4.2, along with the fracture properties employed for both intralaminar matrix cracking and delamination. Depending on the processing conditions, lamina interfaces could be more resin-rich and exhibit homogenized fracture properties that differ from intralaminar matrix cracking [142]. In this study, we assume that the fracture properties within the lamina and at the interfaces are taken to be the same [143]. Figure 4.9a displays the test configuration and the ply layup. The span length, width and thickness of the specimen are 115mm, 12.7mm, 5.25mm, respectively. A precrack (denoted by **T** for teflon in the layup shown in Fig. 4.9) is inserted between $90_4/0$ interface and its length a is 49mm. The specimens are subjected to vertical displacement-controlled loading applied at four different positions at the top surface, represented by the load offsets $L/a = 1, 1.1, 1.2, 1.3$, where L is the distance from the loading position to the left tip. The specimen is clamped to the fixture at both ends.

Figure 4.9b shows the finite element mesh of the specimen (i.e., the macroscopic domain) and the fixture. 8-noded tri-linear hexahedral elements with reduced integration and hourglass control are employed for the discretization. The plies with different orientations are modeled as separate layers of elements. In the z-direction (through the plane), the ply is discretized with one layer of elements. The delamination growth and potential migration region ($\ldots 90_4/\mathrm{T}/0\ldots$) is discretized by a structured mesh. The precrack is embedded in 90°_4 ply, as shown in Fig. 4.9b. The thickness of the pre-crack is set to 6 μm, which is the same as the teflon insert thickness. A row of elements of the same width as the precrack are placed ahead of the precrack to ensure that delamination propagation would proceed without mesh effects. Within the rest of the central 90° ply block, element edges are oriented 60° to the horizontal (x) direction to minimize mesh bias effect as the migration is expected to occur approximately at this angle [137]. The effect of mesh orientation is further discussed below. The numerical modeling of the fixture is the same in Ref. [76]. Constraints are applied to the two ends of the specimen via rigid contact condition with friction between clamp fixture, base plate and the specimen. A clamping force of 1,700N is added on the fixture via two reference nodes whose displacements are coupled with the top nodes on the fixture. The clamping force is applied in the initial step before adding the vertical load at the load offset positions. The stiffness of the fixture is 6.8 GPa and its Poisson's ratio is 0.34. The friction coefficient is set to 0.2. The displacement at the

bottom of the base plate is fixed at all directions.

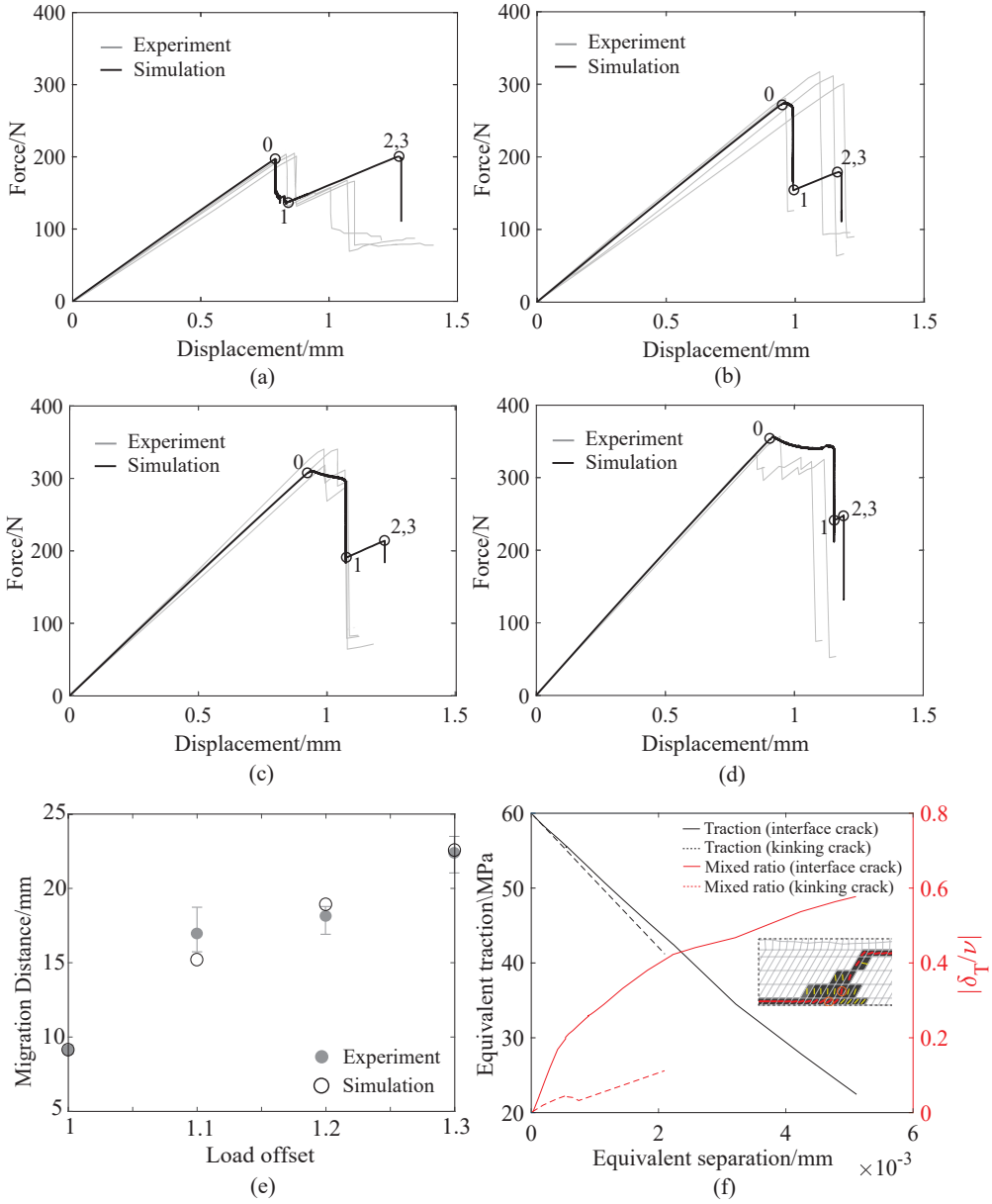

Figure 4.10: Force displacement curves for different load offsets (a) $L/a = 1$, (b) $L/a = 1.1$, (c) $L/a = 1.2$, (d) $L/a = 1.3$. (e) Migration distance vs. load offset. (f) Equivalent traction (solid lines) and mode mixity (dash lines) as a function of equivalent separation extracted from the elements in interface crack and kinking crack for $L/a = 1.1$. The location of the elements are indicated in the inset damage contour.

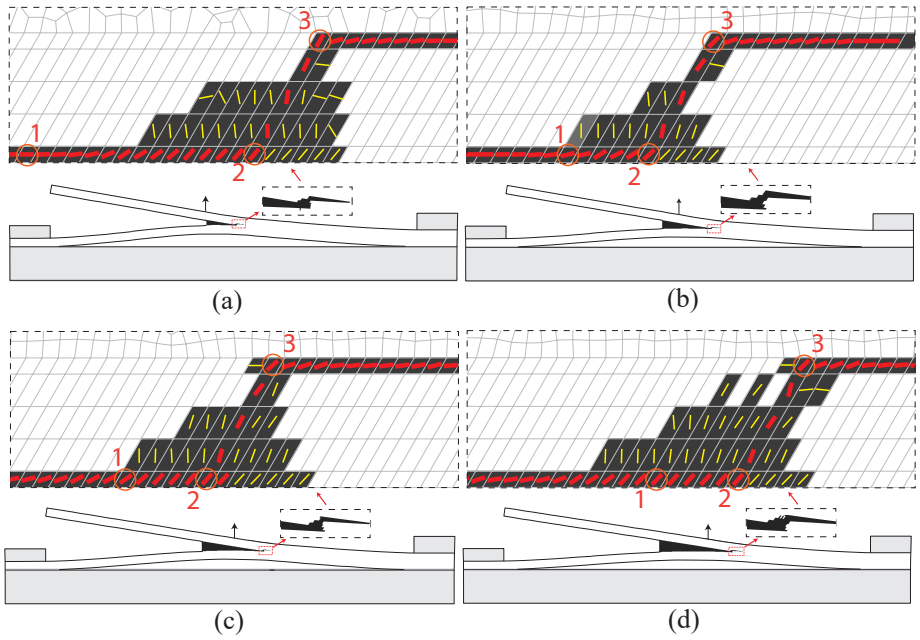

Figure 4.11: Damage contours of delamination and kinking failure around the migration location for the load offset (a) $L/a = 1$, (b) $L/a = 1.1$, (c) $L/a = 1.2$, (d) $L/a = 1.3$. The crack orientation is marked by lines within the elements, wherein thin yellow ones stands for micro crack ($0 < \omega < 1$) and thick red ones for complete crack ($\omega = 1$).

4.5.2 The Results for Different Load Offsets

Figure 4.10a-d show the force-displacement responses predicted for different load offsets and compared with experimental observations. The beginning of the first unstable event (denoted by circle 0) represents the onset of delamination propagation, which continues as the specimen unloads. The stiffness and the peak strength have overall reasonable agreements with the experimental results. The second loading stage is associated with the migration event. Figure 4.11 shows the damage contours at the end of the simulations for each load case. A thin yellow line in an element indicates that the failure path within the microstructure has been set (i.e., initiation criterion has been met), and the failure path has undergone partial damage ($0 < \omega < 1$). Elements with a red line indicates that complete debonding has occurred ($\omega = 1$). The line orientation indicates microcrack direction. Figure 4.11 also displays the corresponding position of the crack tip for the beginning (circle 1) and ending point (circle 3) of the second loading stage in the load-displacement curve. During the unstable propagation stage associated with the first load drop (between circle 0 and 1), the delamination propagates along the $90°/0°$ ply interface without change in the microcrack orientation. The second

loading stage (between circles 1 and 2) is associated with the formation of a process zone around the crack tip, as evidenced by the presence of partially damaged microcracks. At this stage, the dominant crack also progressively changes direction and respectively aligns with approximately 50 degree angle for the cases of $L/a = 1, 1.2, 1.3$ and 45 degree angle for $L/a = 1.1$ at the location of circle 2. The model predicts a rather sudden migration event with insignificant change in load (from circle 2 to 3), which is followed by the second unstable event. Delamination propagation at the upper $90^\circ/0^\circ$ ply interface occurs during the second load drop. As shown in Fig. 4.11, the microcracks reorient to align with the ply interface prior to the propagation of the migrated delamination. The analysis of the initiation as well as the traction-separation conditions that form the dominant crack indicates that the fracture process is largely mode I.

The features of the predicted force-displacement curve are in agreement with experimental observations in the case of $L/a = 1$ (See Fig. 4.10a and [137]). The larger load offset cases do not show a second loading stage, where the entire process occurs under unstable conditions. The simulations also show a progressively smaller stable reload region, which nearly disappears when $L/a = 1.3$. A possible explanation of this discrepancy is that fixing the crack orientation at the onset of interface failure overconstrains the material at the fracture process zone. While the subscale (i.e., unresolved) damage events at the fracture process zone are more aligned with the proposed criterion, load redistribution may result in a further realignment prior to percolation. Some theories adjust crack orientation even after nucleation [82, 144, 145], but enhancement of the current methodology to account for such an effect is nontrivial and outside the scope of this chapter.

Figure 4.10e shows the distance from the precrack tip to the onset of migration crack (i.e. migration distance) as a function of load offsets. The increasing trend of migration distance with normalized load offset agrees well with the experiments. The shifting of the migration distance as a function of load offset (or more specifically, L) has been explained by the shift in the location in the specimen, where the shear stress ahead of the crack tip changes sign [76, 137]. During the delamination propagation stage, the shear stress is positive and the microcracks tend to form with a downward trend. This action is resisted by the 0° ply below the crack, and the delamination precrack extends horizontally. The magnitude of the shear stress reduces with the crack growth. As shown in Fig. 4.5c, the microcracks turn progressively in the clockwise direction with a reduction in shear stress and kink upwards when the shear stress becomes negative. The simulations confirm the

change in sign of shear stress at onset of the migration process, which agrees well with observations made in Ref. [137, 146]. Experiments also indicate a gradual kinking of the macrocrack (a smooth transition to the migration crack) before the migration event. In the current numerical simulations, mesh bias effects do not permit a gradual crack reorientation, but this propensity manifests itself as the formation of the fracture process zone near the migration location. While the extent of the process zone is exacerbated by the numerical effects of mesh bias and due to setting of the microcrack orientation at failure onset, presence of a fracture process zone has been observed experimentally in Ref. [146] as well. Those delamination tests show multiple migration attempts that fail to crack through the lamina before the migration event.

Figure 4.10f extracts the equivalent traction (denoted as $\|\mathbf{t}\| = \sqrt{t_N^2 + t_{S1}^2 + t_{S2}^2}$) and mixed-mode ratio (denoted by $|\delta_T/\nu|$) resolved in the softening stage as a function of equivalent separation (ν) from the elements respectively within the interface crack and the kinking crack near the migration location in the $L/a = 1.1$ case. The curves of mixed mode ratio show that the interface crack (denoted by dash line) nucleates under mode-I condition but gradually involves mode-II fracture in the softening stage, while there is not much shear deformation in the kinking crack (denoted by dash line). The feature is consistent with fractography observations in Ref. [137].

4.5.3 The Effect of Mesh Discretization

The influence of mesh alignment on the migration behavior is also investigated. Figure 4.12a shows the result of $L/a = 1.1$ using a fully structured mesh with vertical mesh alignment. We observe that there is initiated damage with reorientation (denoted by yellow lines) in the 90° ply but the mesh alignment prevents the migration event and the delamination continuously propagates along the initial interface. Another simulation case employs the mesh edge orientation of 45° with respect to the x direction. The damage pattern, microcrack orientations and the force-displacement response (See Fig. 4.12g) are similar to those obtained with the 60° mesh. The dominant crack reorients at 45° before complete migration crack occurs. The migration distance is 15.05mm, very close to the 15.19mm predicted by the mesh with 60° alignment.

A mesh size convergence study for kinking failure is also performed. Additional simulations with element sizes of 4mm, 3mm, 2mm in both x and y directions are performed with the load offset $L/a = 1.1$. The mesh edge orientation is set to 60° with respect to the x direction. Mesh

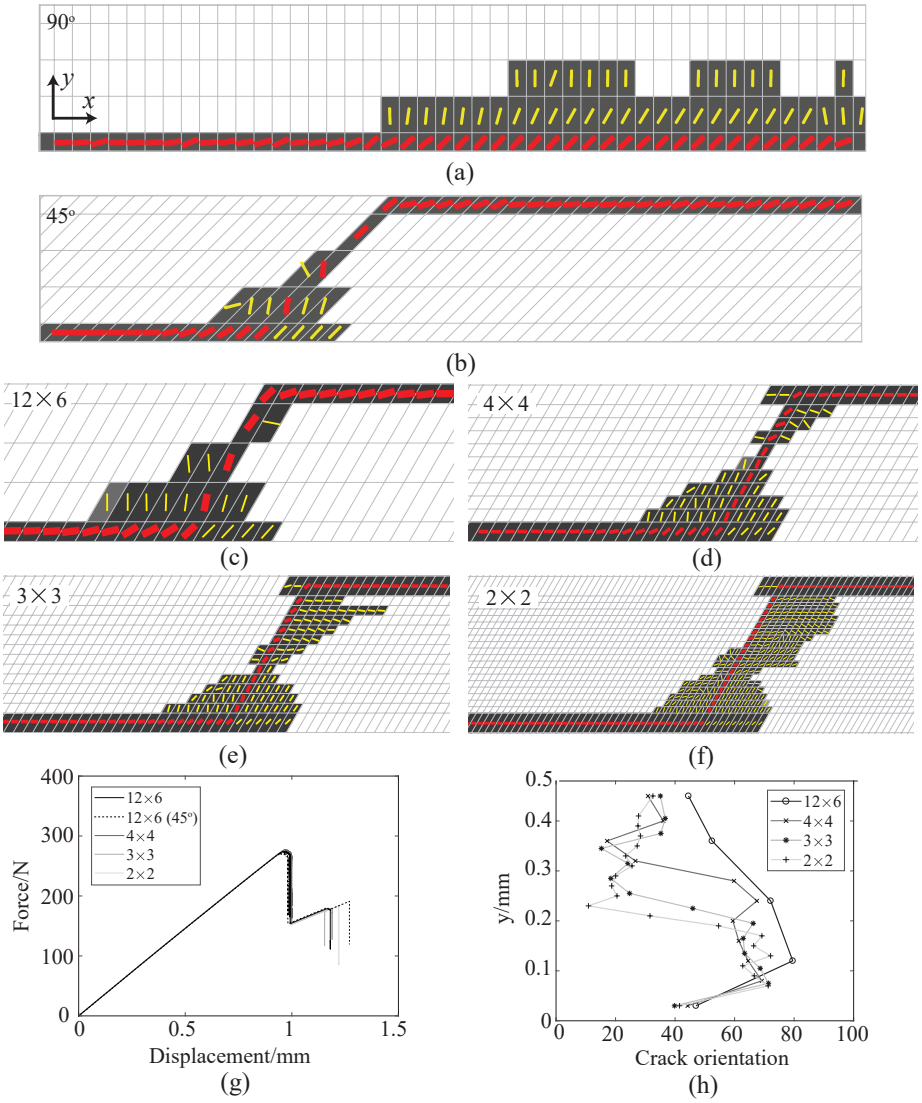

Figure 4.12: Damage contours at the migration location for the load offset of $L/a = 1.1$ with different mesh alignment: (a) $90°$, (b) $45°$, and different sizes of mesh discretizations: (c) $6\text{mm} \times 12\text{mm}$, (d) $4\text{mm} \times 4\text{mm}$, (e) $3\text{mm} \times 3\text{mm}$, (f) $2\text{mm} \times 2\text{mm}$. (g) The force-displacement responses of different mesh sizes and alignment. (h) The crack orientation along the kinking crack ($\omega = 1$) from the bottom interface (y=0.03mm) to the top interface (y=0.45mm) across the 90_4 ply for different mesh sizes.

size regularization is performed using the procedure explained in Ref [25]. Figures 4.12c-f show the damage contours and the crack orientation for different mesh densities. Displaying the same part of the specimen, the contours show that the migration locations have almost no change with the mesh size. The orientation of the complete kinking failure is around $60°$ near the initial interface and gradually becomes near horizontal when it approaches the second interface. It is more clearly

shown in Fig. 4.12f that the orientation converges around 20° to 30° as the mesh size decreases. Figure 4.12g displays the force-displacement responses for different mesh densities, which shows good agreement with each other except for the slight discrepancies of the peak points for the second unstable event.

4.6 Conclusion

This chapter introduces the idea of rotating the microstructure to capture correct microcrack orientation by adaptively selecting the basis approximation, leveraging rotational invariance of microstructure along the rotational plane. As the number of basis for failure path is not changed during the rotation, it achieves higher computational efficiency than embedding multiple failure path in the fixed-oriented microstructure for modeling re-oriented crack propagation. The basis approximation based on a new dynamic crack nucleation and orientation criterion. The nucleation is identified according to the relationship of traction state and crack initiation envelop as a function of microstructure orientation. It is important to note that the crack can also possibly nucleate out of rotational plane. A typical example is that microstructure can either undergo mode II splitting cracks or mode I matrix cracks under pure shear loading and the initiation strength of both failure mechanisms are similar. In this case, the microstructure configuration dictates the prevailing of those failure mechanisms, highlighting the multiscale nature of the problem.

The proposed idea is integrated into MDDT model and validated in the context of four-points bending test using concrete beam and delamination migration test using cross-ply laminates. The outcomes show good qualitative and quantitative agreements with experimental results.

CHAPTER 5

MULTISCALE MODELING FOR SHEAR NON-LINEARITY

5.1 Introduction

This chapter includes the visco-plasticity theory to eigenstrain-based homogenization model (EHM) for describing the shear non-linearity effect in the matrix phase of composite materials. The formulation of Eqs. 2.14, 2.21 are extended by incorporating phase eigenstrain (i.e. visco-plasticity flow) as described in Ref. [50, 51, 147, 148]. EHM combines asymptotic expansion method with transformation field analysis (TFA) to model multiscale inelastic response. However, it is well-known that the nonlinear response obtained by TFA can be overly stiff compared to direct numerical simulation [149, 150], as TFA cannot correctly represent the stress redistribution in the region with stress inhomogeneity. The previous studies typically employ the following two categories of alleviating strategies. One of them is to construct an enhanced approximation of eigenstrain field, by either dynamics partitioning scheme, which subdivides the phase domain into several parts using data-driven algorithm, such as k-means clustering [151, 152], Ward's clustering method [153], or by increasing the order of approximation basis (i.e. using non-linear basis function [49]). This chapter shows a convergence study with respect to number of partitions in the matrix phase using piecewise constant basis function in the context of unnotched specimen and compares the results to direct numerical simulations. Another class of studies focuses on regularizing the influence functions, which, within classic eigenstrain theory, is generated using matrix and fiber elasticity. Those regularization are proposed by either using instantaneous tangential stiffness of stress-strain relationship in yielded matrix [150, 154, 155], or enforcing eigenstrain compatibility [149]. This chapter investigates the potential of regularization strategy using instantaneous tangential stiffness.

5.2 Formulations

5.2.1 Integration of Phase Eigenstrain

Consider the microstructure with periodicity setting in Fig. 2.1. Besides the presence of potential brittle or quasi-brittle fracture, the effect of shear nonlinearity is considered within the matrix phase and it is modeled by viscoplasticity theory. The viscoplasticity flow can be considered as inelastic

strain (or eigenstrain) in the multiscale formulation, and its rate form can be defined by Perzyna formulation:

$$\dot{\boldsymbol{\mu}} = \frac{\langle f(\boldsymbol{\sigma}, \mathbf{p}) \rangle}{\eta} \frac{\partial f(\boldsymbol{\sigma}, \mathbf{p})}{\partial \boldsymbol{\sigma}} \tag{5.1}$$

where η stands for the viscosity parameter, $f(\boldsymbol{\sigma}, \mathbf{p})$ stands for yield surface expressed as a function of stress $\boldsymbol{\sigma}$ and plastic internal state variable $\mathbf{p}$. With addition of inelastic strain $\boldsymbol{\mu}$, the microscopic displacement field in Eq. 2.2 can be expressed as:

$$\mathbf{u}^1(\mathbf{x}, \mathbf{y}, t) = \mathbf{H}(\mathbf{y}) : \boldsymbol{\epsilon}^0(\mathbf{x}, t) + \sum_{a=1}^{n} (\mathbf{h}_a * \boldsymbol{\delta}_a)_{S_a} + (\mathbf{h}_{ph} * \boldsymbol{\mu})_{\Theta} \tag{5.2}$$

where $(\cdot * \cdot)_{\Theta}$ denotes the convolution operation over the microstructure domain, whose integral expression is indicated in Eq. 2.3. $\mathbf{h}_{\mathrm{ph}}$ is the phase influence function and it is numerically evaluated based on constituent elasticity (See Ref. [51]). The strain field expression in Eq. 2.4 can be then adjusted as:

$$\boldsymbol{\epsilon}(\mathbf{x}, \mathbf{y}, t) = \mathbf{A}(\mathbf{y})\boldsymbol{\epsilon}^0 + \sum_{a=1}^{n} (\mathbf{g}_a * \boldsymbol{\delta}_a)_{S_a} + (\mathbf{g}_{\mathrm{ph}} * \boldsymbol{\mu}^0)_{\Theta} \tag{5.3}$$

where $\mathbf{g}_{\mathrm{ph}}$ is the phase polarization influence function, defined as $\mathbf{g}_{\mathrm{ph}} = \nabla^s_{\mathbf{y}} \mathbf{h}_{\mathrm{ph}}$.

The inelastic strain field and stress fields can be approximated using reduced-order basis functions:

$$\boldsymbol{\mu}^0(\mathbf{x}, \mathbf{y}, t) = \sum_{\gamma=1}^{q} N^{(\gamma)}_{\mathrm{ph}}(\mathbf{y}) \boldsymbol{\mu}^{(\gamma)}(\mathbf{x}, t) \tag{5.4}$$

$$\boldsymbol{\sigma}^0(\mathbf{x}, \mathbf{y}, t) = \sum_{\gamma=1}^{q} N^{(\gamma)}_{\mathrm{ph}}(\mathbf{y}) \boldsymbol{\sigma}^{(\gamma)}(\mathbf{x}, t) \tag{5.5}$$

where q is the total number of basis for the reduced-order approximation. $\boldsymbol{\mu}^{(\gamma)}$ and $\boldsymbol{\sigma}^{(\gamma)}$ are non-local inelastic strain and stress coefficients. Similar to Eq. 2.12, the coefficients can be inversely computed as:

$$\boldsymbol{\mu}^{(\zeta)}(\mathbf{x}, t) = \int_{\Theta} \phi^{(\zeta)}(\hat{\mathbf{y}}) \, \boldsymbol{\mu}(\mathbf{x}, \hat{\mathbf{y}}, t) \, d\hat{\mathbf{y}} \tag{5.6}$$

$$\boldsymbol{\sigma}^{(\zeta)}(\mathbf{x}, t) = \int_{\Theta} \phi^{(\zeta)}(\hat{\mathbf{y}}) \, \boldsymbol{\sigma}(\mathbf{x}, \hat{\mathbf{y}}, t) \, d\hat{\mathbf{y}} \tag{5.7}$$

where the nonlocal weight function satisfies the constraints of positivity and normality, as well as orthonormality with the shape function.

Substituting the decomposition of inelastic strain Eq. 5.4 to Eq. 5.3, premultiplying the resulting equation with non-local weight function, integrating over the microstructure domain and taking time derivative yield:

$$\dot{\boldsymbol{\epsilon}}^{(\zeta)}(\mathbf{x},t)-\sum_{\gamma=1}^{q}\mathbf{P}^{(\gamma\zeta)}:\dot{\boldsymbol{\mu}}^{(\gamma)}(\mathbf{x},t)=\mathbf{A}^{(\zeta)}:\dot{\bar{\boldsymbol{\epsilon}}}(\mathbf{x},t) \tag{5.8}$$

where $\mathbf{P}^{(\gamma\zeta)}$ and $\mathbf{A}^{(\zeta)}$ are coefficient tensors representing the contribution of inelastic strain and the concentration of overall strain . Their expressions are:

$$\mathbf{P}^{(\gamma\zeta)}=\int_{\Theta}\int_{\Theta}\phi^{(\zeta)}N_{\mathrm{ph}}^{(\gamma)}\mathbf{g}(\mathbf{y},\hat{\mathbf{y}})d\hat{\mathbf{y}}d\mathbf{y} \tag{5.9}$$

$$\mathbf{A}^{(\zeta)}=\int_{\Theta}\phi^{(\zeta)}\mathbf{A}(\mathbf{y})d\mathbf{y} \tag{5.10}$$

Combining Eq. 5.8 and the constitutive equation $\dot{\boldsymbol{\sigma}}^{(\zeta)}=\mathbf{L}^{(\zeta)}\left(\dot{\boldsymbol{\epsilon}}^{(\zeta)}-\dot{\boldsymbol{\mu}}^{(\zeta)}\right)$ with considering the contribution of separation, and taking time derivative result in the following equation:

$$\mathbf{M}^{(\zeta)}:\dot{\boldsymbol{\sigma}}^{(\zeta)}=\sum_{\gamma=1}^{q}\left[\mathbf{P}^{(\gamma\zeta)}-\delta^{(\gamma\zeta)}\mathbf{I}\right]:\dot{\boldsymbol{\mu}}^{(\gamma)}+\mathbf{A}^{(\zeta)}:\dot{\bar{\boldsymbol{\epsilon}}}+\sum_{\gamma=1}^{m}\mathbf{R}^{(\gamma\alpha)}\cdot\dot{\boldsymbol{\delta}}^{(\alpha)} \tag{5.11}$$

where $\mathbf{M}^{(\zeta)}=[\mathbf{L}^{(\zeta)}]^{-1}$, the coefficient tensor $\mathbf{R}^{(\gamma\alpha)}$, $\alpha=1,2\ldots m$ is expressed as:

$$\mathbf{R}^{(\gamma\alpha)}=\int_{\Theta}\int_{S^{\alpha}}\phi^{(\gamma)}N^{(\alpha)}\mathbf{g}(\mathbf{y},\hat{\mathbf{y}})d\hat{\mathbf{y}}d\mathbf{y} \tag{5.12}$$

Modifying Eq. 2.14 according to Eq. 5.3 yields:

$$\dot{\mathbf{t}}^{(\alpha)}(\mathbf{x},t)-\mathbf{C}^{(\alpha)}:\dot{\bar{\boldsymbol{\epsilon}}}(\mathbf{x},t)+\sum_{\beta=1}^{m}\mathbf{D}^{(\alpha\beta)}\cdot\dot{\boldsymbol{\delta}}^{(\beta)}(\mathbf{x},t)+\sum_{\zeta=1}^{q}\mathbf{F}^{(\alpha\zeta)}:\dot{\boldsymbol{\mu}}^{(\zeta)}=\mathbf{0} \tag{5.13}$$

where the coefficient tensor $\mathbf{F}^{(\alpha\zeta)}$ is expressed as:

$$\mathbf{F}^{(\alpha\zeta)}=\frac{1}{S_{\alpha}}\int_{S_{\alpha}}\int_{\Theta}\mathbf{g}(\mathbf{y},\hat{\mathbf{y}}):\mathbf{L}(\mathbf{y}):\left[\mathbf{P}^{(\gamma\zeta)}-\delta^{(\gamma\zeta)}\mathbf{I}\right]d\hat{\mathbf{y}}d\mathbf{y} \tag{5.14}$$

Similarly to partition of failure path in Eq. 5.15, the microstructure domain can be partition into

nonoverlapping subdomain denoted by $\Theta^{(\gamma)}$. The piecewise function is chosen for the shape and weight functions:

$$N_{\mathrm{ph}}^{(\gamma)}\left(\hat{\mathbf{y}}\right)=\begin{cases}1 & \text{if } \hat{\mathbf{y}}\in\Theta^{(\gamma)}\\ 0 & \text{elsewhere}\end{cases}\qquad \phi^{(\gamma)}\left(\hat{\mathbf{y}}\right)=\begin{cases}1/|\Theta^{(\gamma)}| & \text{if } \hat{\mathbf{y}}\in\Theta^{(\gamma)}\\ 0 & \text{elsewhere}\end{cases} \tag{5.15}$$

When the piecewise function is employed for approximation basis of stress field, the homogenized stress can be computed as:

$$\bar{\boldsymbol{\sigma}}=\sum_{\gamma=1}^{q}\frac{|\Theta^{(\gamma)}|}{|\Theta|}\boldsymbol{\sigma}^{(\gamma)} \tag{5.16}$$

The algebraic nonlinear system of equations including Eq. 5.1, 5.11, 5.13 constitute the reduced-order viscoplasticity microscale problem, wherein the macroscale strain is the forcing function. In the following analysis, the brittle fracture in the failure path is ignored (i.e. $\boldsymbol{\delta}^{\alpha}=0$). Only the stresses in each part are considered as unknown variables.

5.2.2 Regularization based on instantaneous tangent stiffness

The over-stiff response has been observed when the matrix undergoes viscoplasticity and the embedded fiber is still elastic, because the yield stress of fiber is commonly order of magnitude higher than matrix. This is due to inaccurate approximation of inelastic strain field and can be regularized by correction of the coefficient tensors. The regularization is similar to Refs. [150, 156] and adopts instantaneous tangent stiffness to recompute the coefficient tensor $\mathbf{P}^{(\gamma\zeta)}$ instead of integrating phase polarization influence function $\mathbf{g}_{\mathrm{ph}}$ over the microstructure domain (see Eq. 5.9). The instantaneous tangent stiffness $\tilde{\mathbf{L}}^{(\zeta)}$ is expressed within the rate form of stress-strain relationship:

$$\dot{\boldsymbol{\sigma}}^{(\zeta)}=\tilde{\mathbf{L}}^{(\zeta)}:\dot{\boldsymbol{\epsilon}}^{(\zeta)} \tag{5.17}$$

In this case, the influence function problem is described as the rate form of microstructural equilibrium with periodic boundary condition:

$$\nabla_{,y}\cdot\left[\tilde{\mathbf{L}}(\mathbf{y}):\tilde{\mathbf{A}}(\mathbf{y})\right]=0,\quad \mathbf{y}\in\Theta \tag{5.18}$$

The influence function $\tilde{\mathbf{A}}(\mathbf{y})$ is solved in Eq. 5.18 and employed in the rate form of localization

rule:

$$\dot{\boldsymbol{\epsilon}}\left(\mathbf{x},\mathbf{y},t\right)=\tilde{\mathbf{A}}(\mathbf{y}):\dot{\boldsymbol{\epsilon}}^{0}\left(\mathbf{x},t\right) \tag{5.19}$$

Apply reduced-order basis approximation to the field of strain rate $\dot{\boldsymbol{\epsilon}}\left(\mathbf{x},\mathbf{y},t\right)$, the approximated strain rate in each part is expressed as:

$$\dot{\boldsymbol{\epsilon}}^{(\zeta)}\left(\mathbf{x},t\right)=\tilde{\mathbf{A}}^{(\zeta)}:\dot{\tilde{\boldsymbol{\epsilon}}}\left(\mathbf{x},t\right) \tag{5.20}$$

where $\tilde{\mathbf{A}}(\mathbf{y})$ is:

$$\tilde{\mathbf{A}}^{(\zeta)}=\int_{\Theta}\phi^{(\zeta)}\tilde{\mathbf{A}}(\mathbf{y})d\mathbf{y} \tag{5.21}$$

Substitute Eq. 5.20 to the constitutive equation $\dot{\boldsymbol{\sigma}}^{(\zeta)}=\mathbf{L}^{(\zeta)}:\left(\dot{\boldsymbol{\epsilon}}^{(\zeta)}-\dot{\boldsymbol{\mu}}^{(\zeta)}\right)$ results in:

$$\dot{\boldsymbol{\mu}}^{(\zeta)}=\left(\mathbf{I}-\mathbf{M}^{(\zeta)}:\tilde{\mathbf{L}}^{(\zeta)}\right):\tilde{\mathbf{A}}^{(\zeta)}:\dot{\tilde{\boldsymbol{\epsilon}}} \tag{5.22}$$

By associating Eq. 5.22 with Eq. 5.11 and ignoring the separation term, the regularized coefficient tensor $\tilde{\mathbf{P}}^{(\gamma\zeta)}$ can be obtained in terms of:

$$\tilde{\mathbf{A}}^{(\zeta)}-\mathbf{A}^{(\zeta)}=\sum_{\gamma}\tilde{\mathbf{P}}^{(\gamma\zeta)}\left(\mathbf{I}-\mathbf{M}^{(\gamma)}:\tilde{\mathbf{L}}^{(\gamma)}\right):\tilde{\mathbf{A}}^{(\gamma)} \tag{5.23}$$

$\tilde{\mathbf{P}}^{(\gamma\zeta)}$ is indetermined with only Eq. 5.23 because the number of equation (equals to partition number q) is less than the number of unknown (q^2). Additional constraints need to be considered. One solution is to enforce matrix phase with single partition indexed by q, while fiber can be partitioned to more than one part, indexed by $1,2\ldots q-1$. Considering that fiber parts are all elastic, there is:

$$\mathbf{I}-\mathbf{M}^{(\zeta)}:\tilde{\mathbf{L}}^{(\zeta)}=0,\quad\zeta=1,2\ldots q-1 \tag{5.24}$$

Sbustituting Eq. 5.24 to Eq. 5.23, $\tilde{\mathbf{P}}^{(\zeta q)}$ can be expressed by:

$$\tilde{\mathbf{P}}^{(q\zeta)}=\left(\tilde{\mathbf{A}}^{(\zeta)}-\mathbf{A}^{(\zeta)}\right):\left[\tilde{\mathbf{A}}^{(q)}\right]^{-1}:\left(\mathbf{I}-\mathbf{M}^{(q)}:\tilde{\mathbf{L}}^{(q)}\right)^{-1},\quad\zeta=1,2\ldots q-1 \tag{5.25}$$

Considering elastic fiber with $\dot{\boldsymbol{\mu}}^{(\zeta)}=0,\zeta=1,2\ldots q-1$, the regularized governing equation

Eq. 5.11 becomes:

$$\mathbf{M}^{(\zeta)} : \dot{\boldsymbol{\sigma}}^{(\zeta)} = \left[\tilde{\mathbf{P}}^{(q\zeta)} - \delta^{(q\zeta)}\mathbf{I}\right] : \dot{\boldsymbol{\mu}}^{(q)} + \mathbf{A}^{(\zeta)} : \dot{\bar{\boldsymbol{\epsilon}}}, \quad \zeta = 1, 2 \dots q \tag{5.26}$$

5.3 Numerical Implementation

5.3.1 Coefficient Tensor Regularization

The regularization in section 5.2.2 initiates from acquring the instantaneous tangential stiffness $\tilde{\mathbf{L}}$ from rate form of stress-strain relationship in matrix phase. Ref. [154, 155] provided a straightforward method to approximate $\tilde{\mathbf{L}}$ with assuming its isotropy:

$$\tilde{\mathbf{L}} = 2\tilde{G}\mathbf{I}^{\mathrm{dev}} + 3K\mathbf{I}^{\mathrm{vol}} \tag{5.27}$$

where $\tilde{G}$ is the tangent shear modulus influenced by viscoplasticity, while bulk modulus K is intact. $\mathbf{I}^{\mathrm{vol}}$ and $\mathbf{I}^{\mathrm{dev}}$ are respectively given by:

$$\mathbf{I}^{\mathrm{vol}} = \frac{1}{3}\mathbf{I}_2 \otimes \mathbf{I}_2, \quad \mathbf{I}^{\mathrm{dev}} = \mathbf{I}_4 - \mathbf{I}^{\mathrm{vol}} \tag{5.28}$$

where $\mathbf{I}_2, \mathbf{I}_4$ are respectively second and fourth order identity tensor. Under the condition of J2 viscoplasticity, tangent shear modulus at the current increment is computed from the previous state:

$$\tilde{G} =_t \tilde{G} \exp\left(-3G\Delta t/\eta\right) \tag{5.29}$$

where G is the elastic shear modulus.

5.3.2 Macroscopic Stress Update

The governing equations Eqs. 5.26, 5.13 can be solved incrementally. The homogenized strain increment $\Delta\bar{\boldsymbol{\epsilon}}$ and the stresses in each part ${}_t\boldsymbol{\sigma}^{(\zeta)}$ at the previous increment are given for solving the equation. The left subscript denotes the incremental step, i.e., ${}_t(\cdot)$ and ${}_{t+\Delta t}(\cdot)$ stands for the variables at the previous and current increments, respectively. For simplicity, subscript ${}_{t+\Delta t}(\cdot)$ is omitted for simplicity. The variables related to quasi-brittle events in failure path is ignored in the following numerical examples (i.e. $\boldsymbol{\delta}^{\alpha} = 0$). The stresses in each part constitute the state variables:

$\mathbf{d} = \{\boldsymbol{\sigma}^{(1)}, \boldsymbol{\sigma}^{(2)} \cdots \boldsymbol{\sigma}^{(q)}\}$, and the nonlinear equation system at time increment $t + \Delta t$ is expressed as:

$$\boldsymbol{\Phi}(\mathbf{d}) = \{\boldsymbol{\Phi}^{(1)}, \boldsymbol{\Phi}^{(2)} \cdots \boldsymbol{\Phi}^{(q)}\} \tag{5.30}$$

where:

$$\Phi^{(\zeta)}(\mathbf{d}) = \mathbf{M}^{(\zeta)} : \boldsymbol{\sigma}^{(\zeta)} - \Delta t \sum_{\gamma=1}^{n} \left[\tilde{\mathbf{P}}^{(\gamma\zeta)} - \delta^{(\gamma\zeta)}\mathbf{I}\right] : \dot{\boldsymbol{\mu}}^{(\zeta)} \left(\boldsymbol{\sigma}^{(\zeta)}\right) - \mathbf{Q}^{(\zeta)} \tag{5.31}$$

where $\mathbf{Q}^{(\zeta)}$ are constant term in the equation, expressed as:

$$\mathbf{Q}^{(\zeta)} = \sum_{\zeta=1}^{n} \mathbf{M}^{(\zeta)} : {}_t\boldsymbol{\sigma}^{(\zeta)} + \mathbf{A}^{(\zeta)} : \Delta\bar{\boldsymbol{\epsilon}} \tag{5.32}$$

The jacobian of non-linear system is expressed as:

$$\frac{\mathrm{d}\boldsymbol{\Phi}}{\mathrm{d}\mathbf{d}} = \begin{cases} \mathbf{M}^{(\zeta)} - \Delta t \left[\mathbf{P}^{(\eta\zeta)} - \mathbf{I}\right] : \dfrac{\partial \dot{\boldsymbol{\mu}}^{(\eta)}}{\partial \boldsymbol{\sigma}^{(\eta)}} & \text{if } \zeta = \eta \\ -\Delta t \mathbf{P}^{(\eta\zeta)} : \dfrac{\partial \dot{\boldsymbol{\mu}}^{(\eta)}}{\partial \boldsymbol{\sigma}^{(\eta)}} & \text{if } \zeta \neq \eta \end{cases}, \tag{5.33}$$

in which the derivative $\dfrac{\partial \dot{\boldsymbol{\mu}}}{\partial \boldsymbol{\sigma}}$ depends on the form of visco-plasticity model. In this chapter, J2 viscoplasticity is considered for the matrix phase. The constitutive relationship is defined by the following equations:

$$\dot{\boldsymbol{\mu}} = \begin{cases} \dfrac{\langle f \rangle}{\eta} \dfrac{df}{d\boldsymbol{\sigma}} & \text{if } f > 0 \\ 0 & \text{if } f \leq 0 \end{cases}, \quad f = \sigma_v - \sqrt{\frac{3}{2}}\sigma_Y \tag{5.34}$$

where σ_v stands for Von-mises stress, σ_Y stands for yield stress, f represents yield function. The superscript for part index is omitted for brevity.

5.3.3 Implementation procedure

Based on the definition above, the solution procedure for solving viscoplasticity process consists of the following step:

At initialization, assign the indicator $\mathrm{INELAS} \leftarrow 0$ at each integration point. Assign $\tilde{G}$ with elastic shear modulus in matrix phase. During the multiscale simulation at a given increment, $t+\Delta t$, the updated procedure is as follows:

1. Update homogenized strain: $\bar{\boldsymbol{\epsilon}} = {}_t\bar{\boldsymbol{\epsilon}} + \Delta\bar{\boldsymbol{\epsilon}}$;

2. Regularize coefficient tensor $\tilde{\mathbf{P}}^{(q\zeta)}$:

2a. If $\mathrm{INELAS} = 1$: Initialize tangent shear modulus $\tilde{G}$ by Eq. 5.29 using previous tangent shear modulus ${}_t\tilde{G}$. If $\mathrm{INELAS} = 0$: directly assign $\tilde{G} \leftarrow_t \tilde{G}$;

2b. Compute tangential stiffness tensor $\tilde{\mathbf{L}}$ using Eq. 5.27;

2c. Compute concentration coefficient tensor $\tilde{\mathbf{A}}^{(\zeta)}$ using Eq. 5.18 and 5.21;

2d. Compute regularized coefficient tensor $\tilde{\mathbf{P}}^{(q\zeta)}$ based on Eq. 5.25;

2. Initialize the unknown stresses in each part ${}^0\mathbf{d} = {}_t\mathbf{d}$;

4. Loop until convergence;

4a. Compute the system residual: ${}^k\partial\boldsymbol{\Psi}({}^k\mathbf{d})$;

4b. Check convergence: $\| {}^k\partial\boldsymbol{\Psi} \| \leq tol$;

4c. If convergence: Exit loop;

4d. Compute system Jacobian: ${}^k(\partial\boldsymbol{\Psi}/\partial\mathbf{d})$;

4e. Update unknown coefficients: ${}^{k+1}\mathbf{d} = {}^k\mathbf{d} - {}^k(\partial\boldsymbol{\Psi}/\partial\mathbf{d})^{-1}\,{}^k\boldsymbol{\Psi}$;

4f. $k \leftarrow k + 1$

5. Update the macroscopic stress $\bar{\boldsymbol{\sigma}}$ based on Eq. 5.16.

6. If matrix inelastic strain rate $\dot{\boldsymbol{\mu}}^{(q)} > 0$: assign $\mathrm{INELAS} = 1$; else: assign $\mathrm{INELAS} = 0$.

5.4 Unit Cell Test

Consider the same three-dimensional unit cell specimen and square-packed composite microstructure as shown in Fig. 2.4. For simplicity, both fiber and matrix material are considered to be isotropic, which are respectively $E_f = 9.67$GPa, $\nu_f = 0.34$ and $E_m = 4.67$GPa, $\nu_m = 0.34$. The yield stress for matrix phase is 60 MPa. The fiber is considered to be pure elastic. The crack nucleation within the failure path is not considered in the following tests.

5.4.1 Partition Convergence Test

The convergence of non-linear response with respect to partition number is firstly investigated. A tensile loading at y direction is applied to the specimen. The viscosity parameter of matrix phase is $\eta = 100$. Fig. 5.1 shows the different mesh discretizations and partition scheme of three-dimensional microstructure for computing the influence functions and coefficient tensors. The mesh

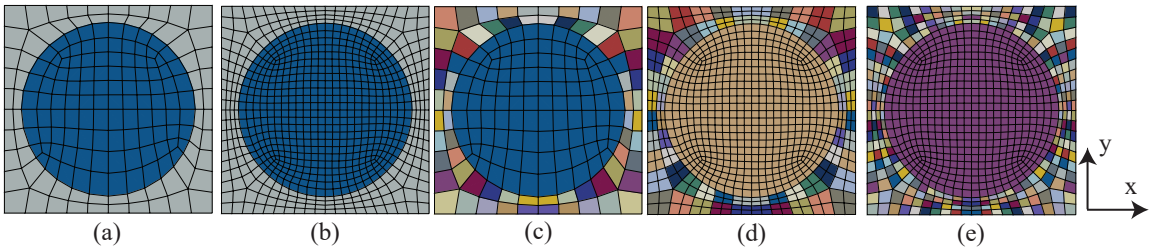

Figure 5.1: Different partitions for matrix in the microstructure: (a) 2 parts with coarse mesh, (b) 2 parts with fine mesh, (c) 35 parts with coarse mesh, (d) 35 parts with fine mesh, (e) 137 parts with fine mesh.

density is categorized into coarse and fine ones. The matrix phase is respectively partitioned into 1, 34 and 136 parts, while the whole fiber is considered as one integral part. There is no partition in the z-direction. For the microstructure with 35 and 137 partitions (See Fig. 5.1c,d,e), the domains for the same part appear to be symmetry along the central y-z plane. For 35 parts with coarse mesh (Fig. 5.1c) and 137 parts with fine mesh (Fig. 5.1e), the matrix phase within the half part of specimen is partitioned element by element. No regularization is applied for the coefficient tensors in those tests.

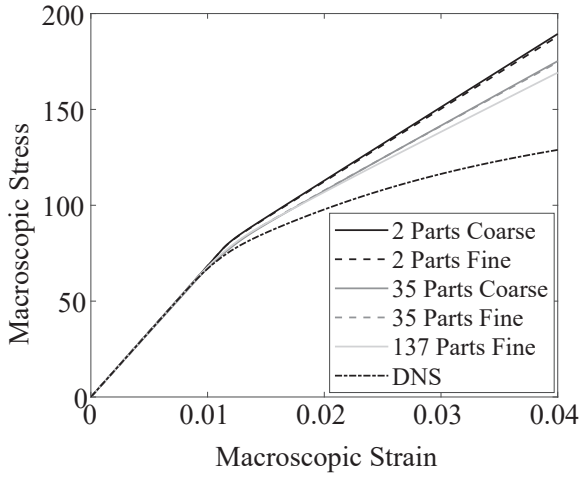

Figure 5.2: Macroscopic stress-strain curves of reduced order model based on different partitions and mesh discretizations of microstructure.

Figure 5.2 shows the corresponding macroscopic stress-strain response for different microstructure discretizations and partitions. The results are compared to DNS result which adopts the coarse mesh partitions. It is obvious that microstructure mesh discretization has little influence on the overall response. The tangential stiffness of non-linear response is reduced with the increased number

of partitions. However, the reduction amplitude from 35 parts to 137 parts is really small and it still exists a significant discrepancy between the DNS result using the coarse mesh partitions (DNS result exhibit softer behavior using finer mesh). The results indicate that only adopting the strategy of increasing partitions is not adequate for resolving the over-stiff non-linear response.

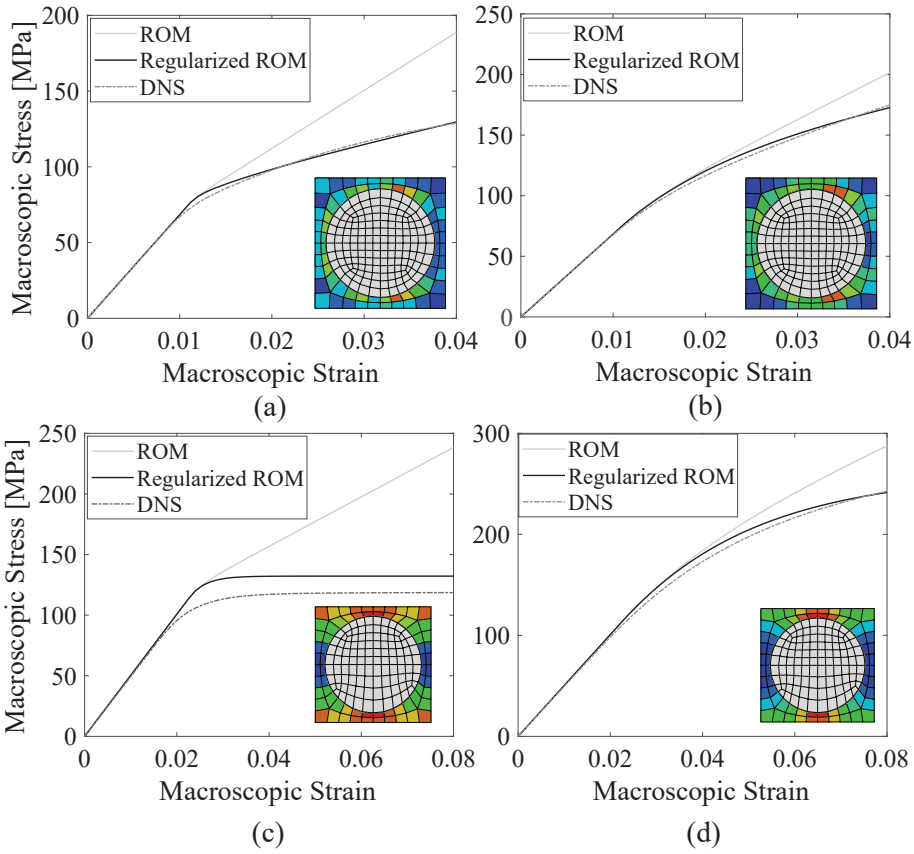

Figure 5.3: Macroscopic stress-strain curves of reduced order model with regularization compared to DNS and unregularized results. (a) $\eta = 100$, tensile loading, (b) $\eta = 1000$, shear loading, (c) $\eta = 100$, shear loading, (d) $\eta = 1000$, shear loading. The inset contours represent the matrix von-mises stress for DNS results, which are amplified in Fig. 5.4.

5.4.2 ROM With Regularization

In this section, the results are generated using the reduced-order model with regularization demonstrated in section 5.2.2. The specimen is respectively applied with tensile loading at y direction and shear load in y-z plane. The viscosity parameters are respectively set to be $\eta = 100, 1000$. The evolution of inelastic strain with higher viscosity becomes slower in terms of loading and the transition from elasticity to plasticity limit will be longer. All of reduced-order models with or

without regularization use dual partitions scheme. Figure 5.3 displays the macroscopic stress-strain responses for different sets of viscosity and loading scenarios. For Fig. 5.3a,b,d, the formulations with regularization achieves good agreement with DNS results. In Fig. 5.3c, the discrepancy mainly results from the approximation of overall yield limit in matrix phase, which is out of capabilities of regularization. The regularization can only affect the tangent stiffness after yielding which shows good agreement with DNS results. The discrepancies of yield limit approximation in tensile loading cases (Fig. 5.3a,b) are not so obvious, largely because their non-uniformity of stress field are less significant than shear loading cases, indicated by the Von-Mises stress contours in Fig. 5.4. In this case, multiple partitions of matrix phase is required in the regularization scheme to resolve the non-uniformity, but it also requires additional constraints for $\tilde{\mathbf{P}}^{(\gamma\zeta)}$, because the number of equations in Eq. 5.23 for solving $\tilde{\mathbf{P}}^{(\gamma\zeta)}$ is not enough for more parts.

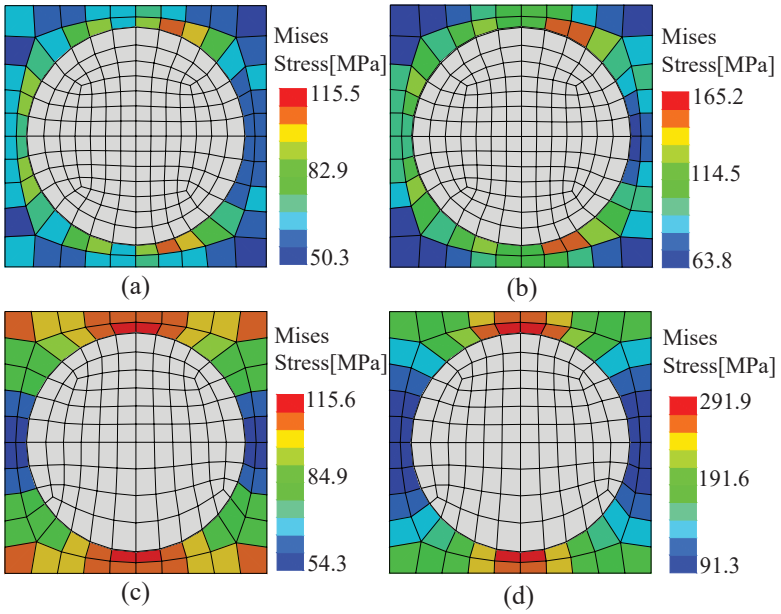

Figure 5.4: Von-mises stress contours in matrix phase for DNS results (a) $\eta = 100$, tensile loading, (b) $\eta = 1000$, shear loading, (c) $\eta = 100$, shear loading, (d) $\eta = 1000$, shear loading. The stress contour in fiber part is not shown for clarification.

5.5 Conclusion

This chapter integrates viscoplasticity theory into homogenization-based multiscale model and respectively investigate the potentials of using partitioning scheme and coefficient tensor regularization for resolving the well-known over-stiff non-linear response. The convergence study with re-

spect to partition numbers in matrix phase indicates that the over-stiff response cannot be alleviated by solely increasing the partition number. The regularization in terms of approximating instantaneous tangent stiffness is adopted and achieve good agreement with DNS results. But the correction of coefficient tensor is currently limited to two-partition scheme, therefore not applicable to approximate the yield limit with fine accuracy. A better strategy lies in combination of the two methods and is expected to be developed.

CHAPTER 6

INVERSE CHARACTERIZATION OF IN-SITU COMPOSITE PROPERTIES

6.1 Introduction

This chapter investigates inverse characterization of in-situ elastic properties of composite constituent materials based on microscopic displacement measurements. The characterization follows an optimization procedure, in which the discrepancy between observed and simulated localized displacements are minimized to arrive at the constituent properties. As evidenced by nano-indentation tests, the matrix properties are considered to exhibit spatial variability that is parametrically described by function forms. The parameters of these functions are cast as the unknowns in the optimization. A focus of this study is accounting for and alleviating the effect of measurement noise, which can severely corrupt the parameter identification process [157]. This study provides formulations for the inverse optimization and the output parameters are shown to be statistical consistent by using the statistical inference [158, 159]. The prerequisites for the consistency with respect to continuity of risk measures and identifiability of model parameters are demonstrated in the proposed problem setting. The effectiveness of the proposed characterization method is evaluated by a series of numerical tests on microscopic continuous fiber-reinforced composite specimen subjected to compressive loading in the transverse direction. The synthetic displacements are assumed to be measured at the fiber centroids mimicking the data from template matching technique [107]. Numerical analysis demonstrate the effect of measurement noise on the fidelity of identified properties, and study conditions for which the effect of noise could be alleviated.

6.2 Inverse characterization methodology

6.2.1 Problem statement

Consider a long fiber reinforced composite specimen at the mesoscale with the domain, Ω, parameterized by the position coordinate vector, $\mathbf{y}$. The specimen is subjected to loading, $F(\mathbf{y})$, applied in the transverse plane (i.e. y_1-y_2 plane shown in Fig. 6.1). The domain includes m randomly positioned fibers within the domain. The elastic constants of each fiber are taken to be spatially constant, and fiber-to-fiber property variability is taken to be negligible. The elastic properties of the matrix

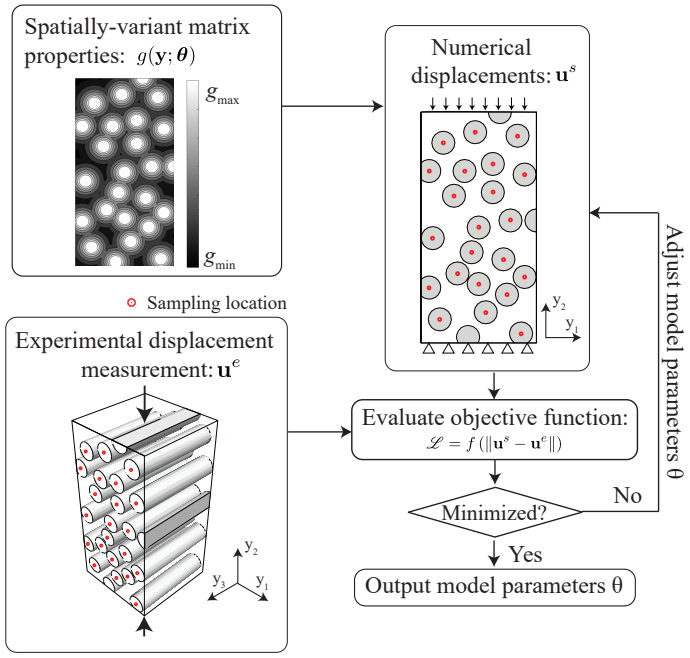

Figure 6.1: Schematic illustration of characterization for in-situ microscopic epoxy resin properties using optimization approach.

are taken to exhibit deterministic spatial variability dictated by the manufacturing processes. Potential stochastic variability in the material properties is taken to be small relative to deterministic variability. Under the action of the mechanical loading, the composite specimen elastically deforms. A discrete set of displacement measurements are collected on the specimen surface parallel to the transverse plane: $\mathbf{u}^{\text{exp}} = \{\mathbf{u}_i^{\text{exp}} \big| i = 1, 2\}$, where n denotes the total number of available displacement observations. Each displacement measurement, $\mathbf{u}_i^{\text{exp}}$ could be the displacement vector at a discrete spatial position in the specimen (i.e., $\mathbf{u}_i^{\text{exp}} = \mathbf{u}(\mathbf{y}_i) + \boldsymbol{\epsilon},\ \mathbf{y}_i \in \Omega$) or a generalized displacement (e.g., $\mathbf{u}_i^{\text{exp}} = \int_\Omega \nu_i(\mathbf{y}) \mathbf{u}_i^{\text{exp}}(\mathbf{y}) \mathrm{d}\Omega + \boldsymbol{\epsilon}$, where ν_i is a weight function). Each measurement data point, $\mathbf{u}_i^{\text{exp}}$ is considered to be noisy (with noise amplitude $\boldsymbol{\epsilon}$) due to inaccuracies in the measurement system. We can further generalize experimental data to be a set of observations from n_{exp} experiments. All n_{exp} experiments could be performed on the same specimen (e.g., load-unload-reload cycles with each load-up resulting in a different dataset due to the measurement noise and due to different load amplitude applied in each cycle); each experiment performed on a different specimen; or a combination thereof. We seek to estimate the spatially variable elastic properties of the material constituents based on this noisy displacement information.

Figure 6.1 schematically depicts the estimation approach, where material property estimation is posed as an optimization problem. In order to operate in a finite dimensional setting, the constituent properties are expressed using a function $\mathbf{g}(\mathbf{y};\boldsymbol{\theta})$, $\mathbf{y} \in \Omega$, where $\boldsymbol{\theta}$ is a vector of constitutive parameters that also describes their spatial variation. The displacement measurement $\mathbf{u}^{\exp}$ is the input to the optimization procedure. Numerical simulation of the mechanical response of the specimen constitutes the "forward problem". The optimization procedure iteratively adjusts the constitutive parameter vector $\boldsymbol{\theta}$, until the discrepancy between the computationally obtained displacement measures $\mathbf{u}^{\mathrm{sim}} = \{\mathbf{u}_i^{\mathrm{sim}} \big| i = 1, 2\}$ and the experimental observations, $\mathbf{u}^{\exp}$ is minimized. The prediction error, $\mathscr{L}$ (also referred to as the objective function, cost or risk function) adopts the form of normalized mean square error (NMSE):

$$\min_{\boldsymbol{\theta}} \mathscr{L}(\boldsymbol{\theta}); \quad \mathscr{L}(\boldsymbol{\theta}) = \frac{\sum_{i=1}^{n} \|\mathbf{u}_i^{\exp} - \mathbf{u}_i^{\mathrm{sim}}(\boldsymbol{\theta})\|^2}{\sum_{i=1}^{n} \|\mathbf{u}_i^{\exp}\|^2} \tag{6.1}$$

$\mathbf{u}_i^{\mathrm{sim}}$ is obtained from the forward problem, which minimizes the potential energy with model parameters $\boldsymbol{\theta}$ and the loading $\mathbf{F}$ as the inputs:

$$\mathbf{U}^{\mathrm{sim}} = \arg\min_{\hat{\mathbf{u}}^{\mathrm{sim}}} \Pi_p\left(\hat{\mathbf{u}}^{\mathrm{sim}}; \boldsymbol{\theta}, \mathbf{F}\right) \tag{6.2}$$

and then sampling the simulated displacement field $\mathbf{U}^{\mathrm{sim}}$, $\mathbf{u}^{\mathrm{sim}}$ for discrete values that correspond to measured data. The model estimate is obtained from Eq. 6.1 as:

$$\hat{\boldsymbol{\theta}}_n = \arg\min_{\boldsymbol{\theta}} \mathscr{L}(\boldsymbol{\theta}) \tag{6.3}$$

The strict convexity of the objective function in Eq. 6.1 with respect to the displacement field $\mathbf{U}^{\mathrm{sim}}$ is obvious, and consequently there is a unique displacement vector $\mathbf{u}^{\mathrm{sim}}$ corresponding to the global minimum in Eq. 6.1. However, $\mathbf{u}^{\mathrm{sim}}$ consists of a set of discrete samples from $\mathbf{U}^{\mathrm{sim}}(\mathbf{y})$. Whether the constitutive parameter set $\hat{\boldsymbol{\theta}}_n$ is unique for a given displacement vector $\mathbf{u}^{\mathrm{sim}}$ is not as obvious. The identifiability condition that ensures the existence of a unique solution $\hat{\boldsymbol{\theta}}_n$ is discussed in the following section.

The solution accuracy depends on the following factors: (1) the amplitude of measurement noise; (2) the amount of experimental observations, n. (3) the inference of the material model,

such as the assumption of the form of properties' spatial variability, $\mathbf{g}(\boldsymbol{\theta}; \mathbf{y})$. In what follows, we particularly focus on the effect of measurement noise and, following the statistical inference theory [158, 159], provide a mathematical framework to show that the prediction error $\mathscr{L}$ and the model estimate $\hat{\boldsymbol{\theta}}_n$ are statistically consistent. That is, the model estimate asymptotically converges to the optimal value with increasing amount of measurement data.

6.2.2 Optimization with noisy data

The set of displacement measurements $\mathbf{u}^{\text{exp}}$ is considered to consist of into the true displacement values $\mathbf{u}$ and a measurement noise term $\boldsymbol{\epsilon}$:

$$\mathbf{u}^{\text{exp}} = \mathbf{u} + \boldsymbol{\epsilon} \tag{6.4}$$

where $\boldsymbol{\epsilon}$ consists of independent random variables for each displacement measurement (i.e., measurement noise is taken to be spatial uncorrelated). Each error component follows a Gaussian probability distribution with the zero mean and the standard deviation of σ_ϵ. The effect of noise randomness on prediction error can be revealed by substituting Eq. 6.4 to Eq. 6.1:

$$\mathscr{L} = \frac{\displaystyle\sum_{i=1}^{n} \|\mathbf{u}_i - \mathbf{u}_i^{\text{sim}}\|^2 + 2\boldsymbol{\epsilon}_i \cdot (\mathbf{u}_i - \mathbf{u}_i^{\text{sim}}) + \|\boldsymbol{\epsilon}_i\|^2}{\displaystyle\sum_{i=1}^{n} \|\mathbf{u}_i\|^2 + 2\boldsymbol{\epsilon}_i \cdot \mathbf{u}_i + \|\boldsymbol{\epsilon}_i\|^2} \tag{6.5}$$

where $\sum_{i=1}^{n} \|\mathbf{u}_i - \mathbf{u}_i^{\text{sim}}\|^2$ is the true prediction error.

Leveraging the law of large numbers, increasing number of sampling points enables:

$$\frac{1}{n}\sum_{i=1}^{n} \boldsymbol{\epsilon}_i \cdot (\mathbf{u}_i - \mathbf{u}_i^{\text{sim}}) \to \mathbb{E}(\boldsymbol{\epsilon}_i) \cdot \mathbb{E}\left(\mathbf{u}_i - \mathbf{u}_i^{\text{sim}}\right) = 0 \tag{6.6}$$

$$\frac{1}{n}\sum_{i=1}^{n} \|\boldsymbol{\epsilon}_i\|^2 \to \mathbb{E}\left(\|\boldsymbol{\epsilon}_i\|^2\right) = \sigma_\epsilon^2, \quad \frac{1}{n}\sum_{i=1}^{n_j} \boldsymbol{\epsilon}_i \cdot \mathbf{u}_i \to \mathbb{E}\left(\boldsymbol{\epsilon}_i \cdot \mathbf{u}_i\right) = 0 \tag{6.7}$$

Equation 6.6 is held only if $\mathbf{u}_i - \mathbf{u}_i^{\text{sim}}$ is continuous for each model parameter $\boldsymbol{\theta} \in \Theta$. The continuity is ensured by strict convexity of the potential energy Π_p with respect to $\mathbf{u}^{\text{sim}}$ for each $\boldsymbol{\theta}$ (See proof for Proposition 2 in Aswani et al. [159]). The convexity of Π_p in terms of full-field dis-

placement in linear elasticity is standard, for instance when $\mathbf{u}^{\mathrm{sim}}$ represents all nodal displacement values of a finite element model [160]. The convexity of Π_p when $\mathbf{u}^{\mathrm{sim}}$ is a subset of the nodal displacement vector is demonstrated in the appendix at the section 6.5.1. Substituting Eqs. 6.6, 6.7 into Eq. 6.5 and setting $n \to \infty$, the objective function asymptotically converges to:

$$\mathscr{L} \to \frac{\sum_{i=1}^{n} \|\mathbf{u}_i - \mathbf{u}_i^{\mathrm{sim}}\|^2 + 2n\sigma_\epsilon^2}{\sum_{i=1}^{n} \|\mathbf{u}_i\|^2 + 2n\sigma_\epsilon^2} \tag{6.8}$$

The asymptotic expression of $\mathscr{L}$ only contains the variance of measurement noise σ_ϵ and the true prediction error. Therefore, provided that the numerical model used to solve the forward problem represents the true model and that the optimization algorithm selected can identify the global minimum of the objective function, the displacement prediction converges to the true value in the optimization as $n \to \infty$:

$$\text{Risk consistency :} \qquad \mathbf{u}^{\mathrm{sim}} \to \mathbf{u} \tag{6.9}$$

Identifiability condition refers to the case when the true material parameter set $\boldsymbol{\theta}_{\mathrm{true}}$ uniquely defines the true displacements under the applied loading. If identifiability condition is satisfied then the model estimation is also convergent:

$$\text{Estimation consistency :} \qquad \hat{\boldsymbol{\theta}} \to \boldsymbol{\theta}_{\mathrm{true}} \tag{6.10}$$

in which $\hat{\boldsymbol{\theta}} = \hat{\boldsymbol{\theta}}_n|_{n\to\infty}$. However, it is possible that two (or more) different parameter sets, $\hat{\hat{\boldsymbol{\theta}}}$ and $\hat{\boldsymbol{\theta}}$ with $\hat{\hat{\boldsymbol{\theta}}} \neq \hat{\boldsymbol{\theta}}$ lead to the true displacement response $\mathbf{u}$ extracted from the measurement locations, and therefore the true value of $\boldsymbol{\theta}$ cannot be identified from $\mathbf{u}$. In the appendix of section 6.5.2, we demonstrate the identifiability condition for a one-dimensional composite specimen in which the spatial variation of matrix stiffness $E_m(y;\boldsymbol{\theta})$ is characterized using the fiber centroid displacements as input. This study shows that regular arrangement of fibers fails the identifiability condition regardless of the form of the spatial variation of the matrix stiffness. In contrast, random arrangement of fibers typically provides sufficient information to satisfy identifiability condition (more detailed analysis presented in the appendix at section 6.5.2). A general extension to two-dimensional specimen is not straightforward, but it is reasonable to suppose that the identifiability condition is satisfied by

considering sufficiently large datasets on specimens with randomly distributed fibers. 2D numerical examples are provided in the following sections that point to this observation.

Based on risk and estimation consistency of the parameter estimation problem, the noise effect is expected to be mitigated with increasing number of sampling points. Besides noise effect, the consistency of displacement and parameter prediction to the true value also depends on a-priori knowledge of the numerical model in the forward problem. Overfitting to the noise might exist if the form of assumed model is more complex than the true model, but it can be excluded by increasing number of sampling points as addition of noise at each sampling points converges to its standard deviation in Eq. 6.8.

6.2.3 Optimization Algorithms

In the numerical studies performed below, we employed two methods to evaluate the optimization problem stated in Eq. 6.1: (1) enumeration algorithm; and (2) sequential quadratic programming (SQP).

The main idea behind the enumeration algorithm is direct sampling of the parameter space and computation of the objective function at every sampling point. While this approach is clearly computationally prohibitive for cases when the number of parameters exceed 2 or 3 due to exponential scaling of sampling, we employ this approach to map the objective function to study its characteristics. We employ uniform sampling of the parameter space. Parameter bounds are set tight enough such that the objective function can be accurately mapped. For efficiency, we refine the grid near the optimal solution and use parallel evaluation of the sampling points.

For identification studies with more than two properties, the sequential quadratic programming (SQP) is employed due to its applicability for constrained optimization problems with large number of unknowns [161]. In the following examples, the constraints are defined as enforcement of the model parameters within reasonable range. All the parameters are normalized within the range of $[0, 1]$ to unify the scale. Several other gradient-based, evolutionary and other optimization methods could also be employed to solve this problem. The gradients of the objective function with respect to model parameters are evaluated using the finite difference method. In order to improve likelihood of achieving the global minimum, the multi-start method is employed, where optimizations are started with randomly selected initial conditions using stratified sampling in the parameter space.

The final output of model parameter is corresponding the smallest objective function among all the optimizations.

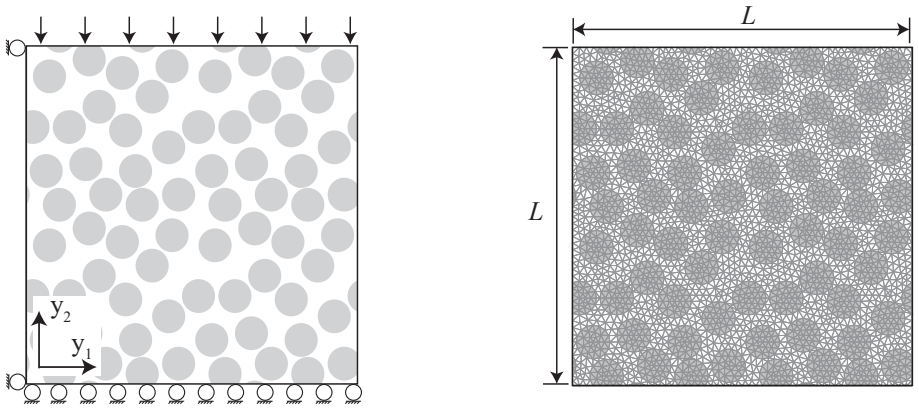

Figure 6.2: Schematic illustration of numerical specimen in the characterization examples. (a) Geometry, loading and boundary conditions. (b) Mesh discretization.

6.3 Numerical examples

A series of numerical examples are conducted based on synthetically generated experiments using unidirectional fiber-reinforced composite specimens. The feasibility of the inverse characterization approach is investigated using enumeration algorithm from the following aspects: (1) the identifiability condition for different fiber arrangements. (2) the effect of measurement noise with different amplitudes on the identification results. (3) the alleviation of noise effect by increasing sampling points and adjusting fiber volume fraction. The capability of the proposed approach in identifying more complex parameter variation are investigated using sequential quadratic programming.

6.3.1 Problem setup

Figure 6.2a illustrates a sample mesoscopic geometry, and the loading and boundary conditions used in the synthetic experiments. Two-dimensional specimens are subjected to 1% strain-controlled compressive loading under plane strain condition. The random arrangement of fibers is created by random sequential adsorption process [162]. The synthetic experimental data is generated by first performing finite element simulations using the open-source package, Calculix [163]. Figure 6.2b shows a sample discretization of the composite specimen. Linear tetrahedral elements are used and

the level of mesh size refinement has been checked to ensure the results' accuracy.

The mechanical properties of the composite constituents are chosen to be similar to a typical graphite reinforced thermoset epoxy composite [93]. The fibers are modeled as transversely isotropic. Fiber moduli are constant within the domain of a fiber and for all fibers within the specimen. The Young's modulus of the isotropic resin is taken to be spatially variable. The resin Young's modulus associated with a spatial point $E_{\mathrm{m}}(\mathbf{y})$ is assumed to be an exponential function of the distance of the material point, $\mathbf{y}$ from the nearest fiber-matrix interface, l:

$$E_{\mathrm{m}}(\mathbf{y}) = \left(E_{\mathrm{int}} - \bar{E}_{\mathrm{m}}\right) \exp\left(-\alpha l\right) + \bar{E}_{\mathrm{m}} \tag{6.11}$$

where E_{int} stands for the resin stiffness at the fiber-matrix interface, α is a parameter that controls the variation of stiffness distribution, $\bar{E}_{\mathrm{m}}$ represents the stiffness at a large distance from the fiber-matrix interface (i.e. $E_{\mathrm{m}} = \bar{E}_{\mathrm{m}}$, with $l \to \infty$) and its value can be considered as the neat resin stiffness. The aforementioned spatial variation is evidenced by the nano-indentation tests in Ref. [98], which reveals an exponential relationship between the indentation modulus and the size of resin pocket. The experimental measurements for E_{int}, $\bar{E}_{\mathrm{m}}$ and α in Ref. [98] are employed for generating synthetic measurements and listed in Table 6.1 along with the Poisson ratio ν_m as well as the fiber properties. The numerical results of the finite element simulations are used as the basis for generating the synthetic experimental data. The data generation mimics the fiber template matching (FTM) algorithm [110, 164], which can detect the 2D coordinates of fiber centroids in images captured within the transverse plane and therefore measure the deformation by comparing the coordinate before and after loading. In the finite element model, an element node is positioned at each fiber centroid to extract the displacement responses in a straight forward manner.

The displacements are polluted with randomly generated synthetic Gaussian noise, the amplitude of which is related to the image resolution in the FTM approach [110]. The correlation between noise amplitude and image resolution is obtained by applying FTM to track the fiber centroid displacements in the synthetic image of undeformed and deformed specimens obtained by the simulation with three different levels of image resolution: 10 pixel, 107 pixel and 325 pixel per fiber diameter. The standard deviations of the absolute error in each displacement component are respectively 0.1661, 0.0104 and 0.003 $\mu\mathrm{m}$. In the following numerical examples, the Gaussian noise

standard deviation in the following synthetic tests ranges from 0 to 0.1 μm.

Table 6.1: Material properties of the composite constituents

Elastic properties of epoxy resin				
E_{int} [GPa]	α	$\bar{E}_m$ [GPa]	ν_m	
7.5426	0.23465	5.06	0.34	
Elastic properties of fiber				
E_1 [GPa]	E_2 [GPa]	G_{12} [GPa]	G_{13} [GPa]	ν_{31}
276	19.5	7.169	70	0.24

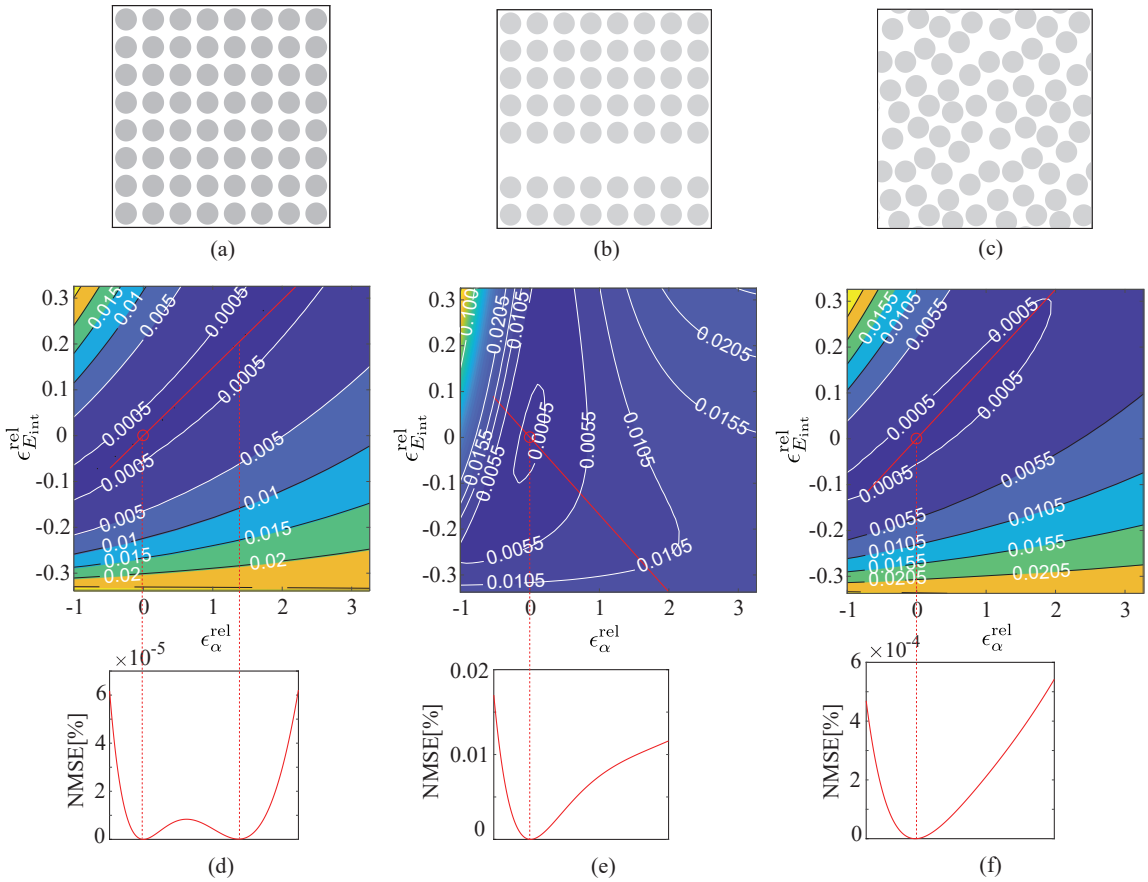

Figure 6.3: The specimen with (a) regular grid of reinforcements, (b) a grid of a resin rich region, and (c) random fiber arrangement. (d,e,f) The corresponding objective function landscapes in E_{int} - α space scaled by relative error $\epsilon^{\text{rel}}_{\boldsymbol{\theta}}$. The second row shows the objective function value along the red line segment embedded in the parameter space.

6.3.2 Identifiability assessment

A more general assessment of identifiability condition is provided in the appendix (See section 6.5.2) in a one-dimensional setting. This section demonstrates the identifiability condition for 2D numerical specimens. For visualization purposes, the problem is studied for two unknown parameters (i.e. $\boldsymbol{\theta} = \{E_{\text{int}}, \alpha\}$). Identifiability is checked by directly plotting the objective function landscape probed using the enumeration algorithm. Three specimens were created with different fiber arrangements as shown in Fig. 6.3. The specimens include a regular grid of reinforcements (Fig. 6.3a), a regular grid with a resin rich region (Fig. 6.3b) that occurs in a laminated arrangement, and a specimen with random fiber arrangement (Fig. 6.3c). No measurement noise is added to fiber centroid displacements. Figure 6.3d-f shows the contours of objective function (denoted by percentage value) generated at the grid points in the parameter space. The contour is displayed in the parameter space scaled by the relative error:

$$\epsilon_{\boldsymbol{\theta}}^{\text{rel}} = \left| \frac{\hat{\theta} - \theta_{\text{true}}}{\theta_{\text{true}}} \right| \tag{6.12}$$

The zero point (denoted by red circle) in the contour plot stands for the true value of these parameters. As shown in Fig. 6.3a, the specimen with uniform resin pocket size show multiple minima since the contour lines near near true value are not closed. The objective function along a line segment that crosses the true minimum (i.e., that corresponds to the correct parameters) is plotted below the contour plot and reaches zero at the point of another parameter set different from the true values. In this case, the parameters are therefore not uniquely identifiable and the optimization problem is not convex. The landscapes for the microstructure with two and more diverse matrix pocket sizes (See Fig. 6.3b,c) shows closed contour lines near the true value and the objective function along the line segment reaches zero only at the true value. The identifiability condition is therefore satisfied and the optimization problems indicate convexity. As further demonstrated in the appendix (See section 6.5.2), the identifiability condition is affected by the sampling of the fiber-to-fiber distance, which describes the functional relationship of the matrix property spatial variation; the number of parameters that describe the spatial variation function, and the measurement samples. The general implication of this study is that in the absence of noise and in a sufficiently large composite with random fiber distribution, where the deformation state is measured using fiber template matching, identifiability is likely to be satisfied even when the spatial variation of the material properties is

relatively complex.

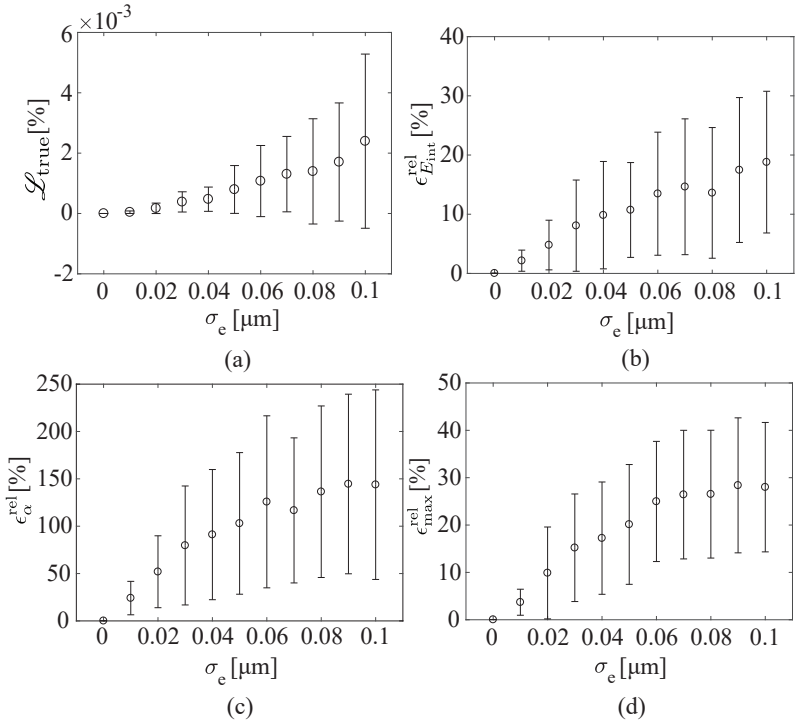

Figure 6.4: The mean value (circle mark) and standard deviation (whisker) of (a) displacement prediction error, (b) E_{int}, (c) α, (d) maximum relative error of stiffness within the distribution, for the characterizations using $200\mu\text{m}$ specimen with different noise levels represented by σ_ϵ.

6.3.3 Noise effect

This section investigates the influence of measurement noise on the identification of the constituent properties. A specimen of size $L = 200\mu\text{m}$ with random arrangement of the fibers (radius of $5\mu\text{m}$) is employed in this study. The fiber volume fraction is set to 55% and there are 280 fibers in total within the specimen. Each displacement component in the synthetic fiber centroid displacement measurements is corrupted with Gaussian noise with zero mean and standard deviation of σ_ϵ. To obtain the variability in the identification result in the presence of noise, synthetic measurements are created 100 times by adding different noise but with the same standard deviations. The effect of noise amplitude is studied by adjusting the value of standard deviation σ_ϵ which takes values from 0 to 0.1 μm with increments of $0.01\mu\text{m}$. Enumeration algorithm is employed for the optimization and optimization are performed for $\{E_{\text{int}}, \alpha\}$ set. Figure 6.4a shows the statistics of the true relative error of displacement prediction ($\mathscr{L}_{\text{true}} := \sum_{i=1}^{n} \|\mathbf{u}_i - \mathbf{u}_i^{\text{sim}}\|^2 / \sum_{i=1}^{n} \|\mathbf{u}_i\|^2$) at each noise

level. The mean value (denoted by circle mark) and the standard deviation (denoted by whisker) of true prediction error are amplified when the noise level increases. The mean value and standard deviation of relative errors in interfacial stiffness E_{int} and spatial variance parameter α are shown in Figs 6.4b,c. The errors in identifying E_{int} and α respectively reach $18.8\% \pm 12\%$ and $143.8\% \pm 100\%$ at the highest noise level. The overall error in the identification of resin stiffness is measured by the maximum relative error within the modulus distribution (named maximum stiffness error herein), expressed by $\epsilon^{\mathrm{rel}}_{\mathrm{max}} = \max_{\mathbf{y}} |(\hat{E}_{\mathrm{m}}(\mathbf{y}) - E_{\mathrm{m}}(\mathbf{y}))|/E_{\mathrm{m}}(\mathbf{y})$, where $E_{\mathrm{m}}(\mathbf{y})$ is the true distribution. As shown in Fig. 6.4c, the maximum stiffness error reaches $28\% \pm 13.7\%$ at the highest noise level, despite significantly higher level of error in the corresponding spatial variance parameter, α. Nevertheless, introduction of measurement error results in significant errors in the identified constituent parameters.

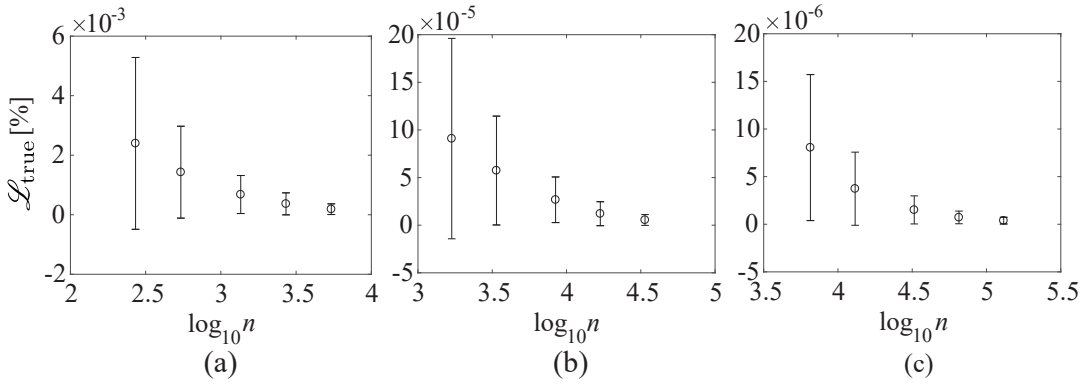

Figure 6.5: The mean value (circle mark) and standard deviation (whisker) of the displacement prediction error for (a) 200 μm, (b) 500 μm (c) 1mm specimen unloaded and reloaded 1,2,5,10,20 times with noise amplitude of $\sigma_\epsilon = 0.1\mu$m. n stands for total number of sampling points.

6.3.4 Alleviating the effects of measurement noise

The corrupting effect of noise can be alleviated by increasing sampling points n, which enables the displacement prediction and model estimation to asymptotically converge to the true value, according to Eqs. 6.9 and 6.10. The increase of n can be achieved by performing multiple experiments in which the noise is generated independently. In the context of using fiber centroids for measurements, n could also be increased by enlarging the specimen size. In the following identification tests, three specimens with the size of 200 μm, 500 μm and 1mm, and the fiber volume fraction of 55% are employed. The total fiber number are respectively 280, 1,750 and 7,000 for each spec-

imen size. In order to increase sampling points, the same specimens were unloaded and reloaded $1, 2, 5, 10, 20$ times. The identification analysis are repeated for 100 times for each specimen loaded n_{exp} times. The measurement error is introduced differently for each identification analysis with the amplitude of $\sigma_e = 0.1\mu\text{m}$.

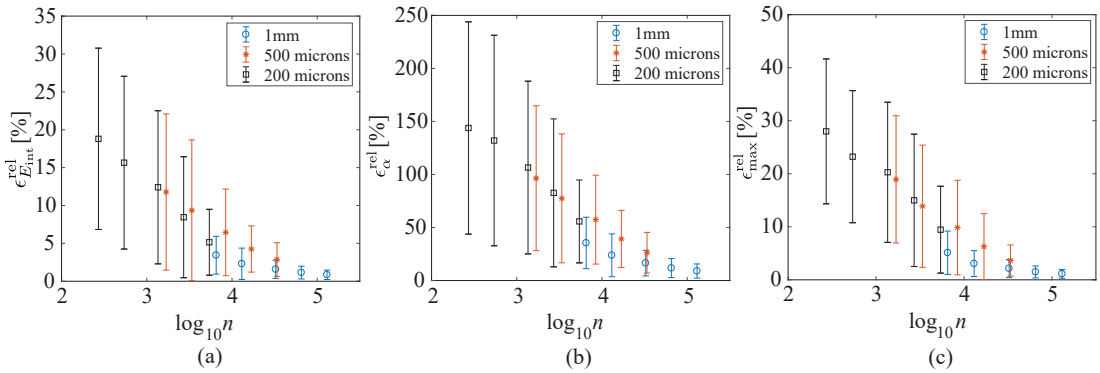

Figure 6.6: The mean value (circle mark) and standard deviation (whisker) of the relative error of (a) E_{int}, (b) α, and (c) maximum relative error of stiffness within the distribution, for the characterizations of 200 μm, 500 μm and 1mm specimen unloaded and reloaded 1,2,5,10,20 times with the noise amplitude of $\sigma_\epsilon = 0.1\mu\text{m}$.

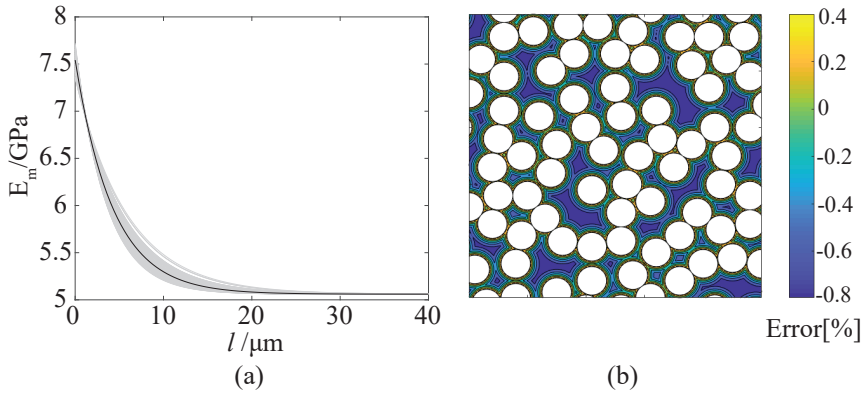

Figure 6.7: (a) The estimated resin stiffness distribution (grey lines) vs. true distribution (black line) along the distance from the nearest fiber l, (b) The contour of relative error of the resin stiffness: $(\hat{E}_{\text{m}}(\mathbf{y}) - E_{\text{m}}(\mathbf{y}))/E_{\text{m}}(\mathbf{y})$ over the central inner $100\mu m \times 100\mu m$ region for one of the estimation, based on the measurement 1mm specimen loaded 20 times.

Figures 6.5a-c respectively show the mean values and ranges of displacement prediction error obtained by enumeration algorithm for each specimen as the size of the measurement dataset n increases. The prediction error reveals less variance with increasing n and the error introduced by the measurement noise is reduced.

Figure 6.6 shows the mean value and standard deviation of the estimate error (E_{int}, α and maximum stiffness error) when the sampling number n increases. The results for each specimen size are discriminated by different colors and markers. For a fixed-sized specimen, we observe a monotonically decreasing trend of bias and variance in the identified parameters with increasing load cycles. Compared among different specimen sizes, the convergence is not monotonic because the reduced rate of noise terms $\boldsymbol{\epsilon}_{(i)} \cdot (\mathbf{u}_{(i)} - \mathbf{u}^s_{(i)})$ and $\boldsymbol{\epsilon}_{(i)} \cdot \mathbf{u}_{(i)}$ in Eqs. 6.6 and 6.7 are different if the specimen changes, but we still observe an overall reduction trend in the estimation error by increasing the specimen size and load-unload cycles. The maximum stiffness error reduces from $28\% \pm 13.7\%$ (200 μm specimen loaded single time) to $1.48\% \pm 1.13\%$ (1mm specimen loaded 10 times) and $1.12\% \pm 0.82\%$ (1mm specimen loaded 20 times). Figure 6.7a shows all the estimated stiffness distributions as a function of the distance from the nearest fiber based on the measurements of 1mm specimen loaded 20 times (denoted by grey lines) and compared to the true value (denoted by black lines). The stiffness error is largest at $l = 0$ (i.e., at the interface) and at the interval of $2\mu\text{m} < l < 15\mu\text{m}$. The latter range is much larger than the average size of the distance between neighboring fibers in the 55% volume fraction specimen. As shown in Fig. 6.7b which indicates the contours of stiffness relative error, we also see the same trend that the higher level of stiffness discrepancy exists at the fiber/matrix interface and the center of the resin pocket. These trends are therefore attributed to scarcer data informing stiffness identification near the interface and within the $[2 - 15]\mu m$ range.

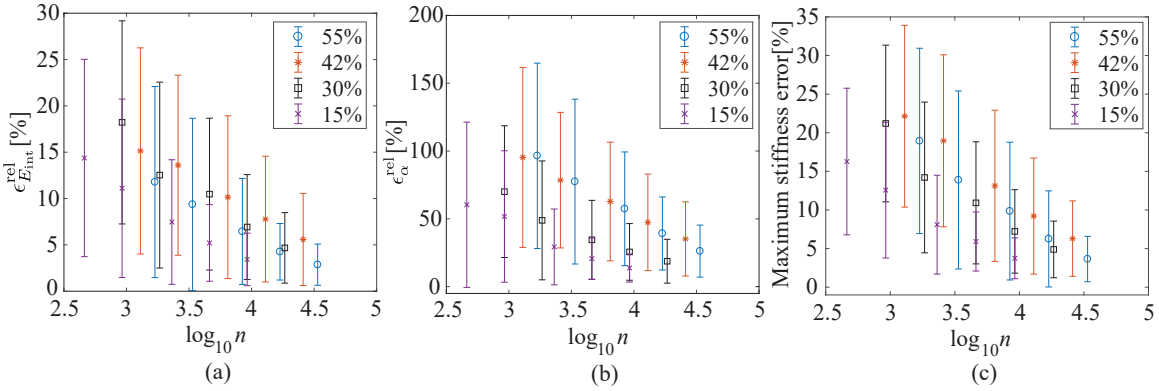

Figure 6.8: The mean value (circle mark) and standard deviation (whisker) of the relative error of (a) E_{int}, (b) α, and (c) maximum relative error of stiffness within the distribution, for the characterizations of 500 μm specimen with 15%, 30%, 42% and 55% fiber volume fraction loaded 1, 2, 5, 10, 20 times with the highest noise level of $\sigma_\epsilon = 0.1\mu m$.

6.3.5 Effect of fiber volume fraction

This section analyzes the effect of fiber volume fraction on identification results. The fiber volume fraction affects property identification in two ways. For a fixed-sized specimen, a reduction in fiber volume fraction indicates reduction of measurement data (assuming data collection is restricted to fiber centroid displacements) and hence adversely affect the identification process. However, a relatively low fiber volume also implies that a higher variation in fiber-to-fiber distance in the specimen to present, leading to better sampling of spatial variability of the property. In this example, we consider fiber volume fractions 15%, 30%, 42%, 55% in 500 μm specimens. Each specimen is subjected to 1, 2, 5, 10, 20 load-unload cycles. Identification analysis are repeated 100 times, and synthetic measurements are generated using measurement noise level of $\sigma_e = 0.1\mu\mathrm{m}$. Figure 6.8 shows the mean value and standard deviation of the characterization error for each volume fraction and measurement data size n. The reducing trend in E_{int} error is apparent. Decreasing volume fraction also significantly lowers the estimation error for the spatial variation term α. This is because the specimen with lower volume fraction has larger sizes of resin pockets amid the fibers, and the spatial variation in resin modulus is more evenly sampled. There is a higher sensitivity of displacement response to the changes in the spatial variation term α and therefore the noise effect is decreased, although the specimen with smaller volume fraction has less sampling points. The results also imply that the characterization of resin-rich region which have substantial spatial variation of stiffness can be more accurate than the fiber-rich region in the composite specimen.

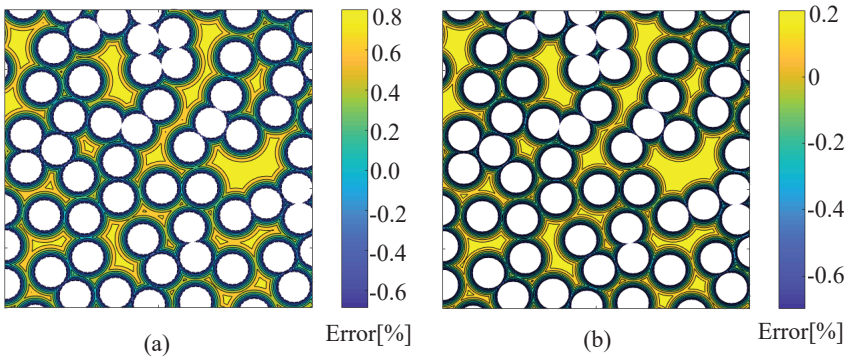

Figure 6.9: The contour of resin modulus relative error over the central $100\mu m \times 100\mu m$ region within 500 μm specimen obtained by the optimization with the unknown parameter of (a) $\boldsymbol{\theta} = \{E_{\mathrm{int}}, \alpha, \nu_{\mathrm{m}}\}$ and (b) $\boldsymbol{\theta} = \{E_{\mathrm{int}}, \alpha, \bar{E}_{\mathrm{m}}, \nu_{\mathrm{m}}\}$

6.3.6 Characterization Including Other Epoxy Resin Properties

This section employs SQP method to identify the full set of parameters for describing resin properties and spatial variability. The scipy python package is used for implementation of SQP approach. Besides E_{int}, α, the resin's Poisson ratio ν_{m} is unknown in the optimization: $\boldsymbol{\theta} = \{E_{\text{int}}, \alpha, \nu_{\text{m}}\}$. Another numerical test also assumes that the resin modulus far away from interface, $\bar{E}_{\text{m}}$ is unknown and needs to be characterized: $\boldsymbol{\theta} = \{E_{\text{int}}, \alpha, \bar{E}_{\text{m}}, \nu_{\text{m}}\}$. Each parameter is constrained within the range of: $E_{\text{int}} \in (0, 10)$, $\bar{E}_{\text{m}} \in (0, 10)$, $\alpha \in (0, 1)$, $\nu_{\text{m}} \in (0, 0.5)$ and normalized within the range of $[0, 1]$ to unify the scale. The initialization for the optimization is randomly selected within the stratified regions in the parameter space. Multiple optimizations are performed by selecting different initializations in the stratified regions. Both two tests adopt the specimen with 42% fiber volume fraction subjected to 20 load-unload cycles. The synthetic measurements of fiber centroid displacements are generated based on the reference parameters in Table 6.1 and the measurement noise amplitude is $\sigma_e = 0.01\mu\text{m}$.

Table 6.2: Prediction error of SQP optimization

	$\epsilon^{\text{rel}}_{\bar{E}_{\text{m}}}$	$\epsilon^{\text{rel}}_{\alpha}$	$\epsilon^{\text{rel}}_{E_{\text{int}}}$	$\epsilon^{\text{rel}}_{\text{max}}$	$\epsilon^{\text{rel}}_{\nu_{\text{m}}}$
Case 1		-7.32%	-0.68%	0.96%	0.01%
Case 2	-0.3%	-5.03%	-0.7%	0.68%	$6.4 \times 10^{-4}\%$

As shown in Table 6.2, the characterization results of two cases show fairly good agreement of resin stiffness and Poisson ratio compared to reference values. The maximum stiffness error $\epsilon^{\text{rel}}_{\text{max}}$ obtained by both cases are around 1% and the discrepancy of Poisson ratio identification from the reference value is negligible. The identification of $\bar{E}_{\text{m}}$ in Case 2 indicates that the resin modulus far away from the interface can be characterized based on scarce data of fiber displacements, although it is not directly revealed in the specimen domain. The contour of stiffness relative error is shown in Fig. 6.9, where the pattern is similar to Fig. 6.7b: the error is largest at the interface or at the center of resin pocket. The maximum error is not shown in Fig. 6.7a because the resolution of contour is limited.

6.4 Conclusion

A generalized optimization framework for inverse characterization of in-situ spatial heterogeneous composite properties is proposed based on transverse displacements measurement. The robustness of optimization formulations under the effect of random measurement noise is demonstrated by the statistical consistency of the model estimation. According to statistical inference theory, the statistical consistency is satisfied based on continuity of risk measures, which is proved to be unconditionally satisfied in this problem, and identifiability of model parameter, which is proved to be dependent on the microstructure configuration and characteristics of property distribution function. The proposed model is validated based on synthetic measurement of fiber centroid displacement to calibrate epoxy resin properties. The characterization results show noise mitigation when increasing the number of fiber samplings (related to larger specimen size and more loading times) or the size of resin pocket (related to smaller fiber volume fraction).

6.5 Appendix

6.5.1 Strict convexity of forward problem formulations

Using the finite element method, potential energy in terms of nodal displacement vector $\mathbf{U}$, the stiffness matrix $\mathbf{K}$ and force vector $\mathbf{F}$ is expressed as [160]:

$$\Pi_p = \frac{1}{2}\mathbf{U}^T\mathbf{K}\mathbf{U} - \mathbf{U}^T\mathbf{F} \tag{6.13}$$

Let's now consider that $\mathbf{u}_{\text{sim}}$ consist of a subset of the nodal displacements. Aggregating the displacement at the measurement points, Eq. 6.13 can be rewritten as:

$$\Pi_p = \frac{1}{2}\begin{bmatrix}(\mathbf{u}_{\text{sim}})^T, (\mathbf{u}_{\text{r}})^T\end{bmatrix}\begin{bmatrix}\mathbf{K}_{\text{ss}} & \mathbf{K}_{\text{sr}} \\ \mathbf{K}_{\text{rs}} & \mathbf{K}_{\text{rr}}\end{bmatrix}\begin{bmatrix}\mathbf{u}_{\text{sim}} \\ \mathbf{u}_{\text{r}}\end{bmatrix} - \begin{bmatrix}(\mathbf{F}_{\text{s}})^T, (\mathbf{F}_{\text{r}})^T\end{bmatrix}\begin{bmatrix}\mathbf{u}_{\text{sim}} \\ \mathbf{u}_{\text{r}}\end{bmatrix} \tag{6.14}$$

where, $\mathbf{u}_{\text{r}}$ collects the nodal displacements at the locations other than the measurement points, $\mathbf{K}_{\text{ss}}$, $\mathbf{K}_{\text{sr}}$, $\mathbf{K}_{\text{rs}}$ and $\mathbf{K}_{\text{rr}}$ are stiffness submatrices, $\mathbf{F}_{\text{s}}$ and $\mathbf{F}_{\text{r}}$ are force subvector after reordering.

Let consider $\mathbf{U}^* = [\mathbf{u}^*_{\text{sim}}, \mathbf{u}^*_{\text{r}}]^T$ are the true state of nodal displacement. The principle of mini-

mum energy $\partial\Pi_p/\partial\mathbf{U}|_{\mathbf{U}=\mathbf{U}^*} = 0$ results in:

$$\mathbf{K}_{\mathrm{ss}}\mathbf{u}^*_{\mathrm{sim}} + \mathbf{K}_{\mathrm{sr}}\mathbf{u}^*_{\mathrm{r}} = \mathbf{F}_{\mathrm{s}} \tag{6.15}$$

$$\mathbf{K}_{\mathrm{rs}}\mathbf{u}^*_{\mathrm{sim}} + \mathbf{K}_{\mathrm{rr}}\mathbf{u}^*_{\mathrm{r}} = \mathbf{F}_{\mathrm{r}} \tag{6.16}$$

Assume another state of nodal displacement $\mathbf{U}^{**} = [\mathbf{u}^{**}_{\mathrm{sim}}, \mathbf{u}^*_{\mathrm{r}}]^T$, in which only $\mathbf{u}^{**}_{\mathrm{sim}}$ is different. The strict convexity of potential energy with respect to subset of nodal displacement $\mathbf{u}_{\mathrm{sim}}$ leads to the following inequality:

$$\Pi_p\left(\mathbf{U}^{**}\right) - \Pi_p\left(\mathbf{U}^*\right) - \frac{\partial\Pi_p}{\partial\mathbf{u}_{\mathrm{sim}}}\Delta\mathbf{u}_{\mathrm{sim}} > 0 \tag{6.17}$$

where $\Delta\mathbf{u}_{\mathrm{sim}} = \mathbf{u}^{**}_{\mathrm{sim}} - \mathbf{u}^*_{\mathrm{sim}}$. Substituting Eq. 6.14, 6.15 and 6.16 to Eq. 6.17 results in:

$$[\Delta\mathbf{u}_{\mathrm{sim}}]^T[\mathbf{K}_{\mathrm{ss}}][\Delta\mathbf{u}_{\mathrm{sim}}] > 0 \tag{6.18}$$

Therefore, the strict convexity is satisfied only if $[\mathbf{K}_{\mathrm{ss}}]$ is positive definite. It is well-known that the stiffness matrix $[\mathbf{K}]$ is already positive definite according to energy minimization principal, which leads to $\mathbf{x}^T\mathbf{K}\mathbf{x} > 0$ for arbitrary non-zero vector $\mathbf{x} \in \mathbb{R}^N \backslash \{\mathbf{0}\}$. Let assume another arbitrary non-zero vector $\mathbf{v} \in \mathbb{R}^n \backslash \{\mathbf{0}\}$ and $\mathbf{x}^* = [\mathbf{v}; \mathbf{0}]$. $[\mathbf{K}_{\mathrm{ss}}]$ is positive definite because:

$$\mathbf{x}^{*T}\mathbf{K}\mathbf{x}^* = \begin{bmatrix}\mathbf{v}^T, \mathbf{0}^T\end{bmatrix}\begin{bmatrix}\mathbf{K}_{\mathrm{ss}} & \mathbf{K}_{\mathrm{sr}} \\ \mathbf{K}_{\mathrm{rs}} & \mathbf{K}_{\mathrm{rr}}\end{bmatrix}\begin{bmatrix}\mathbf{v} \\ \mathbf{0}\end{bmatrix} = [\mathbf{v}^T][\mathbf{K}_{\mathrm{ss}}][\mathbf{v}] > 0 \tag{6.19}$$

6.5.2 Discussion of identifiable condition in 1D composite specimen

Let consider a fiber-reinforced composite bar of length L (See Fig. 6.10) under the displacement loading U. There are totally n fibers with the radius of r and stiffness of E_f. The matrix stiffness E_m is assumed to be spatially varied with the distance (l) from the nearest fiber interface. The fiber centroid displacements $u_{(i)}, i = 1, 2, \ldots n$ are inputs of optimization for characterizing the spatial

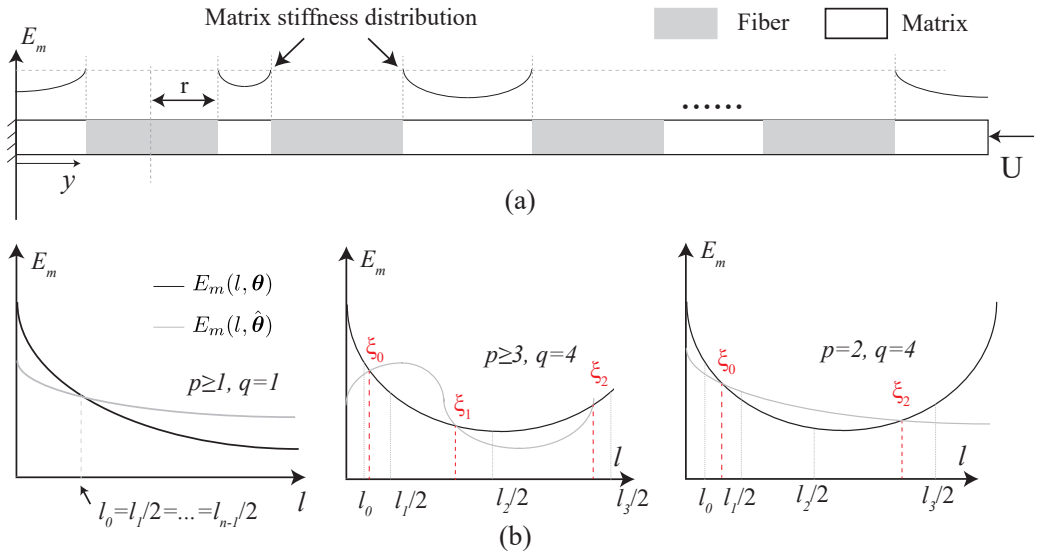

Figure 6.10: (a) Schematic illustration of 1D composite specimens. (b) The three cases for the specimen with uniform matrix length (left), with diverse matrix length and $p \geq q-1$ (middle), $p < q-1$ (right). The identifiability condition is not satisfied for the left and middle cases.

variance parameter $\boldsymbol{\theta}$ of matrix stiffness. It is straightforward to obtain $u_{(i)}$'s expression:

$$u_{(i)} = \frac{\left[\sum_{j=0}^{i-1} \bar{C}_{m_j} l_j E_f + (2i-1)r\right] U}{\sum_{j=0}^{n+1} \bar{C}_{m_j} l_j E_f + 2nr}; \quad i = 1, 2 \ldots n \tag{6.20}$$

where $\bar{C}_{m_i}$ stands for the average compliance of the matrix part between $i-1^{th}$ and i^{th} fiber, $\bar{C}_{m_0}$ for the matrix part between left specimen boundary and the leftmost fiber, $\bar{C}_{m_{n+1}}$ for the matrix part between right boundary and rightmost fiber. In terms of matrix length l_i, the average compliance is expressed as:

$$\bar{C}_{mi} = \begin{cases} \dfrac{1}{l_i} \displaystyle\int_0^{l_i} \frac{\mathrm{d}x}{E_m(l;\boldsymbol{\theta})}; & i = 0, n \\ \dfrac{2}{l_i} \displaystyle\int_0^{l_i/2} \frac{\mathrm{d}x}{E_m(l;\boldsymbol{\theta})}; & i = 1, 2 \ldots n-1 \end{cases} \tag{6.21}$$

Let assume another equivalent displacement measurements $\hat{u}_{(i)}$ led by the constitutive parameters $\hat{\boldsymbol{\theta}}$ and the corresponding average compliance of matrix is $\hat{\bar{C}}_{m_i}$. Substitute Eq. 6.20 to $u_{(i)} = \hat{u}_{(i)}$

and condense out E_f, r, there is:

$$\bar{C}_{m1} l_1 - 2\bar{C}_{m0} l_0 = \hat{\bar{C}}_{m1} l_1 - 2\hat{\bar{C}}_{m0} l_0 \tag{6.22}$$

$$\bar{C}_{m(i+1)} l_{i+1} - \bar{C}_{mi} l_i = \hat{\bar{C}}_{m(i+1)} l_{i+1} - 2\hat{\bar{C}}_{mi} l_i \tag{6.23}$$

According to Cauchy mean value theorem, there exists $\xi_0 \in [\min\{l_0, l_1/2\}, \max\{l_0, l_1/2\}]$, $\xi_1 \in [\min\{l_1/2, l_2/2\}, \max\{l_1/2, l_2/2\}]$, $\ldots \xi_{n-1} \in [\min\{l_{n-1}/2, l_n/2\}, \max\{l_{n-1}/2, l_n/2\}]$ which transforms Eq. 6.22,6.23 into:

$$E_m(\xi_i; \boldsymbol{\theta}) = E_m\left(\xi_i; \hat{\boldsymbol{\theta}}\right) \tag{6.24}$$

The identifiability condition is not held if $\hat{\boldsymbol{\theta}} \neq \boldsymbol{\theta}$ is satisfied within the interval of $\xi_0 \in [\min\{l_0, l_1/2\}, \max\{l_0, l_1/2\}]$, $\xi_i \in [\min\{l_i/2, l_{i+1}/2\}, \max\{l_i/2, l_{i+1}/2\}], i = 1, 2 \ldots n-1$. If $l_i = l_{i+1}, i = 1, 2 \ldots n-1$, Eq. 6.24 is unconditionally satisfied, indicating that the identifiability condition is not held for the specimen with uniform matrix length (indicated in left figure in Fig. 6.10b). If $l_i \neq l_{i+1}, i = 1, 2 \ldots n-1$, there exists diverse size of matrix parts and the satisfaction of Eq. 6.24 depends on the existence of intersection point between $E_m(y; \boldsymbol{\theta})$ and $E_m\left(\xi_i; \hat{\boldsymbol{\theta}}\right)$. Let assume the maximum number of diverse matrix length within the specimen is q and the number of maximum allowable intersection points is p. If $p \geq q-1$, Eq. 6.24 is then satisfied at all the intervals and the identifiability condition is not held (shown in middle figure in Fig. 6.10b). If $p < q-1$, Eq. 6.24 cannot be satisfied at some intervals (e.g., $[l_1/2, l_2/2]$ in the right figure of Fig. 6.10b) and the identifiability condition is satisfied.

CHAPTER 7

CONCLUSIONS

This thesis has proposed a novel physics-based multiscale failure modeling for composite material, also called multiscale discrete damage theory (MDDT). MDDT adopts a new scheme of failure representations at different spatial scales which is motivated by experimental observation, and proposes a regularization scheme to alleviate the mesh-size sensitivity issue with multiscale consistency. The key contributions in this thesis with respect to MDDT and its extensions are listed as follows:

1. MDDT tracks microscopic failure in discrete surfaces within the microstructure and bridges it to continuum representation of damage at the coarse scale based on homogenization principle. It provides a new multiscale approach to model diffuse damage at composite structure level by considering it as culmination of discrete microcrack in terms of microstructure periodicity. Continuum damage representation brings the well-known issue of mesh-size sensitivity, and it is alleviated by employing the concept of macroscale element size-dependent microstructure volume. The microstructure domain size is adjusted in an "effective" manner by scaling the coefficient tensors in the reduced-order model as a function of the macroscale element size. The model's capabilities for modeling complex failure mechanisms are demonstrated based on numerical experiments of open-hole cross-ply composite laminates subjected to tensile loading, which shows good agreements with experiments.

2. MDDT model is then extended to fatigue analysis. The long-term cyclic sensitive failure response in the time domain is evaluated based on temporal multiscale modeling which accelerates the high-cycle fatigue in a great extent. The investigation also put constraints on the form of cyclic sensitive failure constitutive law to avoid the conflicts with the mesh-size objectivity regularization, which assumes that the fracture energy is dissipated in the softening regime under fatigue degradation. The capabilities of extended MDDT for modeling fatigue growth of complex failure modes are demonstrated using open-hole cross-ply laminates, which matches well with experimental failure pattern. The numerical experiments also find that relative fatigue resistances against mode I and mode II fracture can control the

propagation of specific failure modes.

3. The adaptivity to re-oriented crack is integrated to MDDT by selecting the reduced-order basis at arbitrary orientation (i.e. failure path or microstructure orientation) with rotational transformation, leveraging the rotational invariance of microstructure in the rotational plane. The identification criterion of crack orientation and nucleation is proposed based on the adaptivity concept and achieves great efficiency as opposed to a-priori defined multiple failure paths in a fixed-oriented microstructure. A hybrid strategy is required to deal with the possibility that the crack nucleates out of rotational plane. The extension is applied to delamination migration modeling and achieves good agreement with the experiments.

4. Viscoplasticity modeling is integrated into homogenization-based multiscale model to describe the shear non-linearity effect in matrix phase of composite materials. The regularization based on reevaluation of coefficient tensors is incorporated for resolving the issue of inaccurate stress redistribution in the yielded material phase, and achieves good match with DNS results in terms of stress-strain response.

5. A generalized optimization framework is proposed for inverse characterization of in-situ composite material properties provide a reliable input for multiscale model. The proposed approach can characterize the spatial variability of constituent properties by inversely calibrating the coefficients of distribution function. The estimation of optimization is demonstrated with statistical consistency under the stochastic effect of measurement noise and they are asymptotic convergent to the true solution with employing more samples. The proposed approach is validated based on synthetic measurements of fiber centroid displacements, and the outcomes indicate a significant noise mitigation with increasing number of fiber samplings and larger size of resin pocket.

Beyond this thesis, there is definitely potential of MDDT to enhance the capabilities for a broader range of failure modeling:

1. MDDT admits various types of physics-based failure constitutive law to describe the failure processes in the failure path. Chapter 3 has extended MDDT to fatigue with integrating cyclic sensitive damage evolution law. Other constitutive models can be also integrated for broader

range of failure mechanisms, such as adhesive for joint failure, friction for compression failure, matrix ligament after fiber fracture, etc.

2. The reduced-order basis can be adjusted or enhanced. Chapter 4 applies rotational transformation to reduced-order basis for adapting to re-oriented kinking crack. As also mentioned in chapter 4, the number of basis functions for discretizing failure path could be increased to better represent the progressive nature of crack formation. Higher-order basis can be also employed for more accurate approximation of the response field.

3. More complex microstructure feature (like woven structure) and failure path can be introduced in MDDT. A dynamics identification criterion could not only select failure path orientation (as chapter 4 does), but select failure path morphology as well. Besides, MDDT has potentials to study specific failure mechanisms by designating special failure path, such as fiber pull-out/debonding mechanisms within fiber/matrix interface, fiber bridging effect for matrix cracking across the fiber, etc.

4. MDDT can be incorporated with element enrichment method (such as floating node method) to alleviate the mesh-bias issue, the propensity of macroscale cracks to follow mesh lines as mentioned in chapter 4.

References

[1] S Mazumdar. What will drive composites growth in 2015. *Composites manufacturing magazine*, 2015.

[2] Monalisa Das, Sasmita Sahu, and Dayal R Parhi. A review of application of composite materials for aerospace structures and its damage detection using artificial intelligence techniques. In *International Conference on Artificial Intelligence in Manufacturing & Renewable Energy (ICAIMRE)*, 2019.

[3] Peter Wright, X Fu, I Sinclair, and SM Spearing. Ultra high resolution computed tomography of damage in notched carbon fiber—epoxy composites. *Journal of composite materials*, 42 (19):1993–2002, 2008.

[4] Seyed Hamid Reza Sanei, Ercole J Barsotti, David Leonhardt, and Ray S Fertig III. Characterization, synthetic generation, and statistical equivalence of composite microstructures. *Journal of composite materials*, 51(13):1817–1829, 2017.

[5] T Hobbiebrunken, M Hojo, KK Jin, and SK Ha. Influence of non-uniform fiber arrangement on microscopic stress and failure initiation in thermally and transversely loaded cf/epoxy laminated composites. *Composites science and technology*, 68(15-16):3107–3113, 2008.

[6] Michael J Bogdanor, Caglar Oskay, and Stephen B Clay. Multiscale modeling of failure in composites under model parameter uncertainty. *Computational mechanics*, 56(3):389–404, 2015.

[7] J.C. Ding and W. Xu. Determination of mode i interlaminar fracture toughness of composite by a wedge-insert double cantilever beam and the nonlinear j integral. *Composites Science and Technology*, 206:108674, 2021. ISSN 0266-3538. doi: https://doi.org/10.1016/j.compscitech.2021.108674. URL https://www.sciencedirect.com/science/article/pii/S0266353821000300.

[8] R Krueger. The virtual crack closure technique: history, approach and applications. Technical report, 2002.

[9] Zifeng Yuan and Jacob Fish. Are the cohesive zone models necessary for delamination analysis? *Computer Methods in Applied Mechanics and Engineering*, 310:567–604, 2016. ISSN 00457825. doi: 10.1016/j.cma.2016.06.023.

[10] S. Li, M.D. Thouless, A.M. Waas, J.A. Schroeder, and P.D. Zavattieri. Use of a cohesive-zone model to analyze the fracture of a fiber-reinforced polymer–matrix composite. *Composites Science and Technology*, 65(3):537–549, 2005. ISSN 0266-3538. doi: https://doi.org/10.1016/j.compscitech.2004.08.004. URL https://www.sciencedirect.com/science/article/pii/S0266353804002015. JNC13-AMAC-Strasbourg.

[11] X F Hu, B Y Chen, M Tirvaudey, V B C Tan, and T E Tay. Integrated XFEM-CE analysis of delamination migration in multi-directional composite laminates. *Composites Part A: Applied Science and Manufacturing*, 90:161–173, 2016. doi: https://doi.org/10.1016/j.compositesa.2016.07.007.

[12] F.P. van der Meer and L.J. Sluys. Mesh-independent modeling of both distributed and discrete matrix cracking in interaction with delamination in composites. *Engineering Fracture Mechanics*, 77(4):719–735, 2010. ISSN 0013-7944. doi: https://doi.org/10.1016/j.engfracmech.2009.11.010. URL https://www.sciencedirect.com/science/article/pii/S0013794409003518.

[13] De Carvalho, J G Ratcliffe, B Y Chen, S T Pinho, P M Baiz, and T E Tay. Modeling quasi-static and fatigue-driven delamination migration. Technical report, 2014.

[14] F P van der Meer, C Oliver, and L J Sluys. Computational analysis of progressive failure in a notched laminate including shear nonlinearity and fiber failure. *Composites Science and Technology*, 70(4):692–700, 2010. doi: https://doi.org/10.1016/j.compscitech.2010.01.003.

[15] F P Van Der Meer and L J Sluys. Continuum models for the analysis of progressive failure in composite laminates. *Journal of Composite Materials*, 43(20):2131–2156, 2009. doi: https://doi.org/10.1177/0021998309343054.

[16] George Z Voyiadjis and Babur Deliktas. A coupled anisotropic damage model for the inelastic response of composite materials. *Computer methods in applied mechanics and engineering*, 183(3-4):159–199, 2000.

[17] M. Naderi and N. Iyyer. Micromechanical analysis of damage mechanisms under tension of 0°–90° thin-ply composite laminates. *Composite Structures*, 234(May 2019):111659, 2020. ISSN 02638223. doi: 10.1016/j.compstruct.2019.111659. URL https://doi.org/10.1016/j.compstruct.2019.111659.

[18] Qingping Sun, Zhaoxu Meng, Guowei Zhou, Shih Po Lin, Hongtae Kang, Sinan Keten, Haiding Guo, and Xuming Su. Multi-scale computational analysis of unidirectional carbon fiber reinforced polymer composites under various loading conditions. *Composite Structures*, 196(March):30–43, 2018. ISSN 02638223. doi: 10.1016/j.compstruct.2018.05.025. URL https://doi.org/10.1016/j.compstruct.2018.05.025.

[19] TJ Vaughan and CT McCarthy. A micromechanical study on the effect of intra-ply properties on transverse shear fracture in fibre reinforced composites. *Composites Part A: Applied Science and Manufacturing*, 42(9):1217–1228, 2011.

[20] Essam Totry, Jon M Molina-Aldareguía, Carlos González, and Javier LLorca. Effect of fiber, matrix and interface properties on the in-plane shear deformation of carbon-fiber reinforced composites. *Composites Science and Technology*, 70(6):970–980, 2010.

[21] Federico Danzi, Daniele Fanteria, E Panettieri, and M Palermo. A numerical micromechanical study of the influence of fiber–matrix interphase failure on carbon/epoxy material properties. *Composite Structures*, 159:625–635, 2017.

[22] Jacob Fish. *Practical multiscaling*. John Wiley & Sons, 2013.

[23] Rodney Hill. Elastic properties of reinforced solids: some theoretical principles. *Journal of the Mechanics and Physics of Solids*, 11(5):357–372, 1963.

[24] X Zhang and C Oskay. Polycrystal plasticity modeling of nickel-based superalloy in 617 subjected to cyclic loading at high temperature. *Modelling and Simulation in Materials Science and Engineering*, 24(5):55009, 2016. ISSN 1361651X. doi: https://doi.org/10.1088/0965-0393/24/5/055009.

[25] Caglar Oskay, Zimu Su, and Berkcan Kapusuzoglu. Discrete eigenseparation-based reduced

order homogenization method for failure modeling of composite materials. *Computer Methods in Applied Mechanics and Engineering*, 359:112656, 2020.

[26] Damin Xia, Xiang Zhang, and Caglar Oskay. Large-deformation reduced order homogenization of polycrystalline materials. *Computer Methods in Applied Mechanics and Engineering*, 387:114119, 2021.

[27] I. M. Gitman, H. Askes, and L. J. Sluys. Representative volume: Existence and size determination. *Eng. Fract. Mech.*, 74:2518–2534, 2007.

[28] K. Matous, M. G. Kulkarni, and P. H. Geubelle. Multiscale cohesive failure modeling of heterogeneous adhesives. *J. Mech. Phys. Solids*, 56:1511 – 1533, 2008.

[29] C. B. Hirshberger, N. Sukumar, and P. Steinmann. Computational homogenization of material layers with micromorphic mesostructure. *Phil. Mag.*, 88:3603–3631, 2008.

[30] T. B. Belytschko, S. Loehnert, and J. H. Song. Multiscale aggregating discontinuities: a method for circumventing loss of material stability. *Int. J. Numer. Meth. Engng.*, 73:869–894, 2008.

[31] C. V. Verhoosel, J. J. C. Remmers, M. A. Gutiérrez, and R. de Borst. Computational homogenization for adhesive and cohesive failure in quasi-brittle solids. *Int. J. Numer. Meth. Engng.*, 83:1155–1179, 2010.

[32] V. P. Nguyen, O. Lloberas-Valls, M. Stroeven, and L. J. Sluys. Computational homogenization for multiscale crack modeling implementational and computational aspects. *Int. J. Numer. Meth. Eng.*, 2011. doi: 10.1002/nme.3237.

[33] V. P. Nguyen, O. Lloberas-Valls, M. Stroeven, and L. J. Sluys. Homogenization-based multiscale crack modelling: From micro-diffusive damage to macro-cracks. *Comput. Meth. Appl. Mech. Engrg.*, 200:1220 – 1236, 2011.

[34] E W C Coenen, V G Kouznetsova, and M G D Geers. Multi-scale continuous–discontinuous framework for computational-homogenization–localization. *J. Mech. Phys. Solids*, 60:1486–1507, 2012.

[35] E. Bosco, V. G. Kouznetsova, E. W. C. Coenen, M. G. D. Geers, and A. Salvadori. A multi-scale framework for localizing microstructures towards the onset of macroscopic discontinuity. *Comput. Mech.*, 54:299–319, 2014.

[36] P.J. Sanchez, P.J. Blanco, A.E. Huespe, and R.A. Feijóo. Failure-oriented multi-scale variational formulation: Micro-structures with nucleation and evolution of softening bands. *Comput. Meth. Appl. Mech. Engrg.*, 257:221 – 247, 2013.

[37] G. Pijaudier-Cabot and Z. P. Bazant. Nonlocal damage theory. *J. Eng. Mech.*, 113:1512–1533, 1987.

[38] M. G. D. Geers, R. de Borst, W. A. M. Brekelmans, and R. H. J. Peerlings. Strain-based transient-gradient damage model for failure analyses. *Comput. Methods. Appl. Mech. Engng.*, 160:133–153, 1998.

[39] V. Kouznetsova, M. G. D. Geers, and W. A. M. Brekelmans. Multi-scale constitutive modelling of heterogeneous materials with a gradient-enhanced computational homogenization scheme. *Int. J. Numer. Meth. Engng.*, 54:1235–1260, 2002.

[40] J. Oliver, M. A. Caicedo, E. Roubin, A. E. Huespe, and J. A. Hernandez. Continuum approach to computational multiscale modeling of propagating fracture. *Comput. Meth. Appl. Mech. Engrg.*, 294:384–427, 2015.

[41] I. M. Gitman, H. Askes, and L.J. Sluys. Coupled-volume multi-scale modelling of quasi-brittle material. *European Journal of Mechanics - A/Solids*, 27:302 – 327, 2008.

[42] M. J. Bogdanor, S. Mahadevan, and C. Oskay. Uncertainty quantification in damage modeling of heterogeneous materials. *Int. J. Mult. Comp. Eng.*, 11:289–307, 2013.

[43] M. J. Bogdanor, C. Oskay, and S. B. Clay. Multiscale modeling of failure in composites under model parameter uncertainty. *Comput. Mech.*, 56:389–404, 2015.

[44] S. Zhang and C. Oskay. Hybrid multiscale integration for directionally scale separable problems. *Int. J. Numer. Meth. Engng.*, 113:1755–1778, 2018.

[45] J. Yvonnet and Q.-C. He. The reduced model multiscale method (R3M) for the non-linear homogenization of hyperelastic media at finite strains. *J. Comput. Phys.*, 223:341–368, 2007. ISSN 0021-9991. doi: {10.1016/j.jcp.2006.09.019}.

[46] M. Cremonesi, D. Neron, P. A. Guidault, and P. Ladeveze. A pgd-based homogenization technique for the resolution of nonlinear multiscale problems. *Comput. Meth. Appl. Mech. Engrg.*, 267:275–292, 2013.

[47] H. Moulinec and P. Suquet. A numerical method for computing the overall response of nonlinear composites with complex microstructure. *Comput. Meth. Appl. Mech. Engng*, 157: 69–94, 1998.

[48] G. J. Dvorak and J. Zhang. Transformation field analysis of damage evolution in composite materials. *J. Mech. Phys. Solids*, 49:2517–2541, 2001.

[49] J. C. Michel and P. Suquet. Computational analysis of nonlinear composite structures using the nonuniform transformation field analysis. *Comput. Meth. Appl. Mech. Engng*, 193:5477–5502, 2004.

[50] R. Crouch and C. Oskay. Symmetric meso-mechanical model for failure analysis of heterogeneous materials. *Int. J. Mult. Comp. Eng.*, 8:447–461, 2010.

[51] Caglar Oskay and Jacob Fish. Eigendeformation-based reduced order homogenization for failure analysis of heterogeneous materials. *Computer Methods in Applied Mechanics and Engineering*, 196(7):1216–1243, 2007. ISSN 00457825. doi: 10.1016/j.cma.2006.08.015.

[52] P Sparks and C Oskay. The Method of Failure Paths for Reduced-Order Computational Homogenization. *International Journal for Multiscale Computational Engineering*, 14(5):515–534, 2016. ISSN 1543-1649. doi: https://doi.org/10.1615/IntJMultCompEng.2016018702.

[53] C Oskay. Two-level multiscale enrichment methodology for modeling of heterogeneous plates. *International journal for numerical methods in engineering*, 80(9):1143–1170, 2009. doi: https://doi.org/10.1002/nme.2652.

[54] Shuhai Zhang and Caglar Oskay. Reduced order variational multiscale enrichment method for elasto-viscoplastic problems. *Computer Methods in Applied Mechanics and Engineering*, 300:199–224, 2016.

[55] Lyle R Deobald, Gerald E Mabson, Bernhard Dopker, D M Hoyt, Jeff Baylor, and Doug Graesser. Interlaminar fatigue elements for crack growth based on virtual crack closure technique. *Collection of Technical Papers - AIAA/ASME/ASCE/AHS/ASC Structures, Structural Dynamics and Materials Conference*, 5(April):4656–4663, 2007. ISSN 02734508.

[56] Stephen Jimenez and Ravindra Duddu. On the parametric sensitivity of cohesive zone models for high-cycle fatigue delamination of composites. *International Journal of Solids and Structures*, 82:111–124, 2016. ISSN 00207683. doi: 10.1016/j.ijsolstr.2015.10.015. URL http://dx.doi.org/10.1016/j.ijsolstr.2015.10.015.

[57] A Turon, J Costa, P P Camanho, and C G Dávila. Simulation of delamination in composites under high-cycle fatigue. *Composites Part A: Applied Science and Manufacturing*, 38(11): 2270–2282, 2007. ISSN 1359835X. doi: 10.1016/j.compositesa.2006.11.009.

[58] O. J. Nixon-Pearson, S. R. Hallett, P. W. Harper, and L. F. Kawashita. Damage development in open-hole composite specimens in fatigue. Part 2: Numerical modelling. *Composite Structures*, 2013. ISSN 02638223. doi: 10.1016/j.compstruct.2013.05.019.

[59] Shigeki YASHIRO and Tomonaga OKABE. Numerical Prediction of Fatigue Damage Progress in Holed CFRP Laminates Using Cohesive Elements. *Journal of Solid Mechanics and Materials Engineering*, 3(11):1212–1221, 2009. ISSN 1880-9871. doi: 10.1299/jmmp.3.1212.

[60] T. Okabe and S. Yashiro. Damage detection in holed composite laminates using an embedded FBG sensor. *Composites Part A: Applied Science and Manufacturing*, 43(3):388–397, 2012. ISSN 1359835X. doi: 10.1016/j.compositesa.2011.12.009.

[61] Endel V. Iarve, Kevin Hoos, Michael Braginsky, Eric Zhou, and David H. Mollenhauer. Progressive failure simulation in laminated composites under fatigue loading by using dis-

crete damage modeling. *Journal of Composite Materials*, 51(15):2143–2161, 2017. ISSN 1530793X. doi: 10.1177/0021998316681831.

[62] Jianxu Shi, David Chopp, Jim Lua, N. Sukumar, and Ted Belytschko. Abaqus implementation of extended finite element method using a level set representation for three-dimensional fatigue crack growth and life predictions. *Engineering Fracture Mechanics*, 77(14):2840–2863, 2010. ISSN 00137944. doi: 10.1016/j.engfracmech.2010.06.009.

[63] Chen Wang and Xiwu Xu. An extended phantom node method study of crack propagation of composites under fatigue loading. *Composite Structures*, 154:410–418, 2016. ISSN 02638223. doi: 10.1016/j.compstruct.2016.07.022. URL http://dx.doi.org/10.1016/j.compstruct.2016.07.022.

[64] Bijan Mohammadi, Babak Fazlali, and Davood Salimi-Majd. Development of a continuum damage model for fatigue life prediction of laminated composites. *Composites Part A: Applied Science and Manufacturing*, 93:163–176, 2017. ISSN 1359835X. doi: 10.1016/j.compositesa.2016.11.021. URL http://dx.doi.org/10.1016/j.compositesa.2016.11.021.

[65] Eugene Fang, Xiaodong Cui, and Jim Lua. A continuum damage and discrete crack-based approach for fatigue response and residual strength prediction of notched laminated composites. *Journal of Composite Materials*, 51(15):2203–2225, 2017. ISSN 1530793X. doi: 10.1177/0021998317705975.

[66] Paria Naghipour, Evan J Pineda, Brett A Bednarcyk, Steven M Arnold, and Anthony M Waas. Fatigue analysis of notched laminates: A time-efficient macro-mechanical approach. *Journal of Composite Materials*, 51(15):2163–2180, 2017. ISSN 1530793X. doi: 10.1177/0021998316668569.

[67] Thomas E Wilt, Steven M Arnold, and Atef F Saleeb. A Coupled/uncoupled computational scheme for deformation and fatigue damage analysis of unidirectional metal-matrix composites. In *ASTM Special Technical Publication*, volume 1315, pages 65–82, 1997.

[68] Robert Crouch, Caglar Oskay, and Stephen Clay. Multiple spatio-temporal scale modeling

of composites subjected to cyclic loading. *Computational Mechanics*, 51(1):93–107, 2013. ISSN 01787675. doi: 10.1007/s00466-012-0707-9.

[69] Robert Crouch and Caglar Oskay. Accelerated time integrator for multiple time scale homogenization. *International Journal for Numerical Methods in Engineering*, 101(13):1019–1042, mar 2015. ISSN 00295981. doi: 10.1002/nme.4863.

[70] Michael J Bogdanor, Stephen B Clay, and Caglar Oskay. Interacting Damage Mechanisms in Laminated Composites Subjected to High Amplitude Fatigue. *Journal of Engineering Mechanics*, 145(10):1–11, 2019. ISSN 07339399. doi: 10.1061/(ASCE)EM.1943-7889.0001655.

[71] Ron H J Peerlings, W A Marcel Brekelmans, René de Borst, and Marc G D Geers. Gradient-enhanced damage modelling of high-cycle fatigue. *International Journal for Numerical Methods in Engineering*, 49(12):1547–1569, 2000.

[72] Jacob Fish and Caglar Oskay. A nonlocal multiscale fatigue model. *Mechanics of Advanced Materials and Structures*, 12(6):485–500, 2005. ISSN 15376494. doi: 10.1080/15376490500259319.

[73] M W McElroy, F Leone, J Ratcliffe, M Czabaj, and F G Yuan. Simulation of delamination-migration and core crushing in a CFRP sandwich structure. *Composites Part A: Applied Science and Manufacturing*, 79:192–202, 2015. doi: https://doi.org/10.1016/j.compositesa.2015.08.026.

[74] R. Krueger, M. K. Cvitkovich, T. K. O'Brien, and P. J. Minguet. Testing and Analysis of Composite Skin/Stringer Debonding under Multi-Axial Loading. *Journal of Composite Materials*, 34(15):1263–1300, 2000. doi: https://doi.org/10.1177/002199830003401502.

[75] S R Hallett, B G Green, W G Jiang, and M R Wisnom. An experimental and numerical investigation into the damage mechanisms in notched composites. *Composites Part A: Applied Science and Manufacturing*, 40(5):613–624, 2009. doi: https://doi.org/10.1016/j.compositesa.2009.02.021.

[76] N V De Carvalho, B Y Chen, S T Pinho, J G Ratcliffe, P M Baiz, and T E Tay. Modeling delamination migration in cross-ply tape laminates. *Composites Part A: Applied Science and Manufacturing*, 71:192–203, 2015. doi: https://doi.org/10.1016/j.compositesa.2015.01.021.

[77] M W McElroy, R Gutkin, and M Pankow. Interaction of delaminations and matrix cracks in a CFRP plate, Part II: Simulation using an enriched shell finite element model. *Composites Part A: Applied Science and Manufacturing*, 103:252–262, 2017. doi: https://doi.org/10.1016/j.compositesa.2017.10.006.

[78] X. F. Hu, X. Lu, and T. E. Tay. Modelling delamination migration using virtual embedded cohesive elements formed through floating nodes. *Composite Structures*, 204(May):500–512, 2018. ISSN 02638223. doi: 10.1016/j.compstruct.2018.07.120.

[79] B R Seshadri, N V de Carvalho, J G Ratcliffe, G E Mabson, and L Deobald. Simulating the clamped tapered beam specimen under quasi-static and fatigue loading using floating node method. *AIAA/ASCE/AHS/ASC Structures, Structural Dynamics, and Materials Conference, 2018*, (210049):1–15, 2018. doi: https://doi.org/10.2514/6.2018-0971.

[80] B. Y. Chen, T. E. Tay, S. T. Pinho, and V. B.C. Tan. Modelling delamination migration in angle-ply laminates. *Composites Science and Technology*, 142:145–155, 2017. ISSN 02663538. doi: 10.1016/j.compscitech.2017.02.010.

[81] H K Adluru, K H Hoos, E V Iarve, and J G Ratcliffe. Delamination initiation and migration modeling in clamped tapered laminated beam specimens under static loading. *Composites Part A: Applied Science and Manufacturing*, 118(June 2018):202–212, 2019. doi: https://doi.org/10.1016/j.compositesa.2018.12.020.

[82] D C Pham, X Cui, X Ren, and J Lua. A discrete crack informed 3D continuum damage model and its application for delamination migration in composite laminates. *Composites Part B: Engineering*, 165:554–562, may 2019. doi: https://doi.org/10.1016/j.compositesb.2019.02.045.

[83] L F Varandas, A Arteiro, G Catalanotti, and B G Falzon. Micromechanical analysis of inter-

laminar crack propagation between angled plies in mode I tests. *Composite Structures*, 220 (March):827–841, 2019. doi: https://doi.org/10.1016/j.compstruct.2019.04.050.

[84] K Yun, Z Wang, L He, and J Liu. A damage model based on the introduction of a crack direction parameter for FRP composites under quasi-static load. *Composite Structures*, 184 (May 2017):388–399, 2018. doi: https://doi.org/10.1016/j.compstruct.2017.09.099.

[85] Hong T Hahn and Stephen W Tsai. Nonlinear elastic behavior of unidirectional composite laminae. *Journal of Composite Materials*, 7(1):102–118, 1973.

[86] C. T. Sun and J. L. Chen. A Simple Flow Rule for Characterizing Nonlinear Behavior of Fiber Composites. *Journal of Composite Materials*, 23(10):1009–1020, 1989. ISSN 1530793x. doi: 10.1177/002199838902301004.

[87] G. Z. Voyiadjis and G. Thiagarajan. An anisotropic yield surface model for directionally reinforced metal-matrix composites. *International Journal of Plasticity*, 11(8):867–894, 1995. ISSN 07496419. doi: 10.1016/S0749-6419(95)00035-6.

[88] John G Michopoulos, John G Hermanson, Athanasios Iliopoulos, Samuel Lambrakos, and Tomonari Furukawa. On the constitutive response characterization for composite materials via data-driven design optimization. In *International Design Engineering Technical Conferences and Computers and Information in Engineering Conference*, volume 54792, pages 499–511, 2011.

[89] Caglar Oskay and Jacob Fish. On calibration and validation of eigendeformation-based multiscale models for failure analysis of heterogeneous systems. *Computational Mechanics*, 42 (2):181–195, 2008.

[90] Robert D Crouch, Stephen B Clay, and Caglar Oskay. Experimental and computational investigation of progressive damage accumulation in cfrp composites. *Composites Part B: Engineering*, 48:59–67, 2013.

[91] Robert Crouch, Caglar Oskay, and Stephen Clay. Multiple spatio-temporal scale modeling of composites subjected to cyclic loading. *Computational Mechanics*, 51(1):93–107, 2013.

[92] Michael J Bogdanor and Caglar Oskay. Prediction of progressive damage and strength of im7/977-3 composites using the eigendeformation-based homogenization approach: Static loading. *Journal of Composite Materials*, 51(10):1455–1472, 2017.

[93] Michael J. Bogdanor and Caglar Oskay. Prediction of progressive fatigue damage and failure behavior of IM7/977-3 composites using the reduced-order multiple space-time homogenization approach. *J Compos Mater*, 51(15):2101–2117, 2017. ISSN 1530793X. doi: 10.1177/0021998316665683.

[94] Serge Zhandarov and Edith Mäder. Characterization of fiber/matrix interface strength: applicability of different tests, approaches and parameters. *Composites Science and Technology*, 65(1):149–160, 2005.

[95] EPS Tan, SY Ng, and CT Lim. Tensile testing of a single ultrafine polymeric fiber. *Biomaterials*, 26(13):1453–1456, 2005.

[96] SJV Frankland, VM Harik, GM Odegard, DW Brenner, and TS Gates. The stress–strain behavior of polymer–nanotube composites from molecular dynamics simulation. *Composites Science and Technology*, 63(11):1655–1661, 2003.

[97] Jeremy R. Gregory and S. M. Spearing. Nanoindentation of neat and in situ polymers in polymer-matrix composites. *Composites Science and Technology*, 65(3-4):595–607, 2005. ISSN 02663538. doi: 10.1016/j.compscitech.2004.09.001.

[98] M. Hardiman, T. J. Vaughan, and C. T. McCarthy. Fibrous composite matrix characterisation using nanoindentation: The effect of fibre constraint and the evolution from bulk to in-situ matrix properties. *Composites Part A: Applied Science and Manufacturing*, 68:296–303, 2015. ISSN 1359835X. doi: 10.1016/j.compositesa.2014.09.022. URL http://dx.doi.org/10.1016/j.compositesa.2014.09.022.

[99] Marina Pecora, Olga Smerdova, and Marco Gigliotti. In-situ characterization of the local mechanical behaviour of polymer matrix in 3D carbon fiber composites by cyclic indentation test. *Composite Structures*, 244(March):112268, 2020. ISSN 02638223. doi: 10.1016/j.compstruct.2020.112268. URL https://doi.org/10.1016/j.compstruct.2020.112268.

[100] M. Rodríguez, J. M. Molina-Aldareguía, C. González, and J. Llorca. Determination of the mechanical properties of amorphous materials through instrumented nanoindentation. *Acta Materialia*, 60(9):3953–3964, 2012. ISSN 13596454. doi: 10.1016/j.actamat.2012.03.027.

[101] Jang Kyo Kim, Man Lung Sham, and Jingshen Wu. Nanoscale characterisation of interphase in silane treated glass fibre composites. *Composites Part A: Applied Science and Manufacturing*, 32(5):607–618, 2001. ISSN 1359835X. doi: 10.1016/S1359-835X(00)00163-9.

[102] Sanjeev K. Khanna, P. Ranganathan, S. B. Yedla, R. M. Winter, and K. Paruchuri. Investigation of nanomechanical properties of the interphase in a glass fiber reinforced polyester composite using nanoindentation. *Journal of Engineering Materials and Technology, Transactions of the ASME*, 125(2):90–96, 2003. ISSN 00944289. doi: 10.1115/1.1543966.

[103] Zhong Hu, Mahdi Farahikia, and Fereidoon Delfanian. Fiber bias effect on characterization of carbon fiber-reinforced polymer composites by nanoindentation testing and modeling. *Journal of Composite Materials*, 49(27):3359–3372, 2015. ISSN 1530793X. doi: 10.1177/0021998314562221.

[104] M Hardiman, TJ Vaughan, and CT McCarthy. The effect of fibre constraint in the nanoindentation of fibrous composite microstructures: A finite element investigation. *Computational materials science*, 64:162–167, 2012.

[105] L. P. Canal, C. González, J. M. Molina-Aldareguía, J. Segurado, and J. Llorca. Application of digital image correlation at the microscale in fiber-reinforced composites. *Composites Part A: Applied Science and Manufacturing*, 43(10):1630–1638, 2012. ISSN 1359835X. doi: 10.1016/j.compositesa.2011.07.014.

[106] Mahoor Mehdikhani, Mohammadali Aravand, Baris Sabuncuoglu, Michaël G. Callens, Stepan V. Lomov, and Larissa Gorbatikh. Full-field strain measurements at the micro-scale in fiber-reinforced composites using digital image correlation. *Composite Structures*, 140: 192–201, 2016. ISSN 02638223. doi: 10.1016/j.compstruct.2015.12.020.

[107] J. Chevalier, P. P. Camanho, F. Lani, and T. Pardoen. Multi-scale characterization and modelling of the transverse compression response of unidirectional carbon fiber reinforced

epoxy. *Composite Structures*, 209(July 2018):160–176, 2019. ISSN 02638223. doi: 10.1016/j.compstruct.2018.10.076.

[108] I. Tabiai, D. Texier, P. Bocher, D. Therriault, and M. Levesque. In-situ Full Field Out of Plane Displacement and Strain Measurements at the Micro-Scale in Single Reinforcement Composites under Transverse Load. *Experimental Mechanics*, 60(3):359–377, 2020. ISSN 17412765. doi: 10.1007/s11340-019-00541-z.

[109] Mahoor Mehdikhani, Christian Breite, Yentl Swolfs, Jeroen Soete, Martine Wevers, Stepan V Lomov, and Larissa Gorbatikh. Digital volume correlation for meso/micro in-situ damage analysis in carbon fiber reinforced composites. *Composites Science and Technology*, 213: 108944, 2021.

[110] Peter J. Creveling, William W. Whitacre, and Michael W. Czabaj. A fiber-segmentation algorithm for composites imaged using X-ray microtomography: Development and validation. *Composites Part A: Applied Science and Manufacturing*, 126(August):105606, 2019. ISSN 1359835X. doi: 10.1016/j.compositesa.2019.105606. URL https://doi.org/10.1016/j.compositesa.2019.105606.

[111] Z Su and C Oskay. Mesh size objective fatigue damage propagation in laminated composites using the multiscale discrete damage theory. *Computational Mechanics*, 67(3):969–987, 2021. doi: https://doi.org/10.1007/s00466-021-01978-7.

[112] Zimu Su and Caglar Oskay. Modeling arbitrarily oriented and reorienting multiscale cracks in composite materials with adaptive multiscale discrete damage theory. *Computational Mechanics*, pages 1–18, 2022.

[113] A. Benssousan, J. L. Lions, and G. Papanicolaou. *Asymptotic Analysis for Periodic Structures*. North-Holland, Amsterdam, 1978.

[114] J. M. Guedes and N. Kikuchi. Preprocessing and postprocessing for materials based on the homogenization method with adaptive finite element methods. *Comput. Meth. Appl. Mech. Engrg.*, 83:143–198, 1990.

[115] K. Terada and N. Kikuchi. Nonlinear homogenization method for practical applications. In S. Ghosh and M. Ostoja-Starzewski, editors, *Computational Methods in Micromechanics*, volume AMD-212/MD-62, pages 1–16. ASME, 1995.

[116] Pedro P. Camanho and Carlos G. Dávila. Mixed-mode decohesion finite elements for the simulation of delamination in composite materials. 2002.

[117] I. M. Gitman, H. Askes, and L.J. Sluys. Coupled-volume multi-scale modelling of quasi-brittle material. *European Journal of Mechanics - A/Solids*, 27:302 – 327, 2008.

[118] S Govindjee, G J Kay, and J C Simo. Anisotropic modelling and numerical simulation of brittle damage in concrete. *International Journal for Numerical Methods in Engineering*, 38 (21):3611–3633, 1995. doi: https://doi.org/10.1002/nme.1620382105.

[119] Zdeněk P. Bažant and Byung H. Oh. Crack band theory for fracture of concrete. *Matériaux et construction*, 16(3):155–177, 1983.

[120] P. A. Sparks and C. Oskay. The method of failure paths for reduced-order computational homogenization. *Int. J. Mult. Comp. Eng.*, 14:515–534, 2016.

[121] Marco Salviato, Viet T Chau, Weixin Li, Zdeněk P Bažant, and Gianluca Cusatis. Direct testing of gradual postpeak softening of fracture specimens of fiber composites stabilized by enhanced grip stiffness and mass. *Journal of Applied Mechanics*, 83(11):111003, 2016.

[122] R. M. O'Higgins, M. A. McCarthy, and C. T. McCarthy. Comparison of open hole tension characteristics of high strength glass and carbon fibre-reinforced composite materials. *Compos. Sci. Technol.*, 68:2770–2778, 2008.

[123] Kedar Kirane and Zdeněk P. Bažant. Microplane damage model for fatigue of quasibrittle materials: Sub-critical crack growth, lifetime and residual strength. *International Journal of Fatigue*, 70:93–105, 2015. ISSN 01421123. doi: 10.1016/j.ijfatigue.2014.08.012.

[124] H Khoramishad, A D Crocombe, K B Katnam, and I A Ashcroft. Predicting fatigue damage in adhesively bonded joints using a cohesive zone model. *International Journal of Fatigue*, 32(7):1146–1158, 2010. ISSN 01421123. doi: 10.1016/j.ijfatigue.2009.12.013.

[125] M L Benzeggagh and M Kenane. Measurement of mixed-mode delamination fracture toughness of unidirectional glass/epoxy composites with mixed-mode bending apparatus. *Composites Science and Technology*, 56(4):439–449, 1996. ISSN 02663538. doi: 10.1016/0266-3538(96)00005-X.

[126] M. Kenane and M.L. Benzeggagh. Mixed-mode delamination fracture toughness of unidirectional glass/epoxy composites under fatigue loading. *Composites Science and Technology*, 57(5):597–605, 1997. ISSN 02663538. doi: 10.1016/S0266-3538(97)00021-3.

[127] Caglar Oskay and Jacob Fish. Fatigue life prediction using 2-scale temporal asymptotic homogenization. *International Journal for Numerical Methods in Engineering*, 61(3):329–359, 2004.

[128] Miguel A Jimenez and Antonio Miravete. Application of the finite-element method to predict the onset of delamination growth. *Journal of Composite Materials*, 38(15):1309–1335, 2004.

[129] Luiz F Kawashita and Stephen R Hallett. A crack tip tracking algorithm for cohesive interface element analysis of fatigue delamination propagation in composite materials. *International Journal of Solids and Structures*, 2012. ISSN 00207683. doi: 10.1016/j.ijsolstr.2012.03.034.

[130] S. M. Spearing and P. W.R. Beaumont. Fatigue damage mechanics of composite materials Part III: Prediction of post-fatigue strength. *Composites Science and Technology*, 44(4):299–307, 1992. ISSN 02663538. doi: 10.1016/0266-3538(92)90067-D.

[131] R Ambu, F Aymerich, and F Bertolino. Investigation of the effect of damage on the strength of notched composite laminates by digital image correlation. *Journal of Strain Analysis for Engineering Design*, 40(5):451–461, 2005. ISSN 03093247. doi: 10.1243/030932405X16106.

[132] C M Wang and C S Shin. Residual properties of notched [0/90]4S AS4/PEEK composite laminates after fatigue and re-consolidation. *Composites Part B:Engineering*, 33(1):67–76, 2002. ISSN 13598368. doi: 10.1016/S1359-8368(01)00049-X.

[133] M. König, R. Krüger, K. Kussmaul, M. von Alberti, and M. Gädke. *Characterizing Static and Fatigue Interlaminar Fracture Behavior of a First Generation Graphite/Epoxy Composite*. ASTM International, 1997. doi: 10.1520/stp18270s.

[134] R. H. Martin and G. B. Murri. *Characterization of Mode I and Mode II Delamination Growth and Thresholds in AS4/PEEK Composites*. ASTM International, 1990. doi: 10.1520/stp24115s.

[135] Caglar Oskay and Su Zimu. Prediction of Fatigue Failure in Fibrous Composites Using the Reduced-Order Multiscale Discrete Damage Theory. *SAMPE 2019-Charlotte, NC, May 2019*, 2019.

[136] J. C. Gálvez, M. Elices, G. V. Guinea, and J. Planas. Mixed mode fracture of concrete under proportional and nonproportional loading. *International Journal of Fracture*, 94(3):267–284, 1998. ISSN 03769429. doi: 10.1023/A:1007578814070.

[137] J G Ratcliffe, M. W. Czabaj, and T K O'Brien. A test for chracterizing delamination migration in carbon/epoxy tape laminates. Technical Report August 2013, NASA, 2013.

[138] William H Press, Saul A Teukolsky, William T Vetterling, and Brian P Flannery. Golden section search in one dimension. *Numerical Recipes in C: The Art of Scientific Computing*, page 2, 1992.

[139] R M O'Higgins, M A McCarthy, and C T McCarthy. Comparison of open hole tension characteristics of high strength glass and carbon fibre-reinforced composite materials. *Composites Science and Technology*, 68(13):2770–2778, 2008. doi: https://doi.org/10.1016/j.compscitech.2008.06.003.

[140] Wei H. Ng, Amit G. Salvi, and Anthony M. Waas. Characterization of the in-situ nonlinear shear response of laminated fiber-reinforced composites. *Composites Science and Technology*, 70(7):1126–1134, 2010. ISSN 02663538. doi: 10.1016/j.compscitech.2010.02.024. URL http://dx.doi.org/10.1016/j.compscitech.2010.02.024.

[141] A Makeev, G Seon, Y Nikishkov, Nguyen D., Mathews P., and M E Robeson. Analysis Methods for Improving Confidence in Material Qualification for Laminated Composites. *Journal of the American Helicopter Society*, 64(1):1–13, 2019. doi: https://doi.org/10.4050/JAHS.64.012006.

[142] H Masaki, A Tadashi, T Mototsugu, A Taiji, O Shojiro, and E Yoshihiro. Modes I and II interlaminar fracture toughness and fatigue delamination of CF/epoxy laminates with self-same epoxy interleaf. *International Journal of Fatigue*, 28(10):1154–1165, 2006. ISSN 0142-1123. doi: 10.1016/j.ijfatigue.2006.02.004.

[143] Michael W. Czabaj and James G. Ratcliffe. Comparison of intralaminar and interlaminar mode I fracture toughnesses of a unidirectional IM7/8552 carbon/epoxy composite. *Composites Science and Technology*, 89:15–23, 2013. ISSN 02663538. doi: 10.1016/j.compscitech.2013.09.008. URL http://dx.doi.org/10.1016/j.compscitech.2013.09.008.

[144] M Jirásek and T Zimmermann. Rotating Crack Model with Transition to Scalar Damage. *Journal of Engineering Mechanics*, 124(3):277–284, 1998. doi: 10.1061/(ASCE)0733-9399(1998)124:3(277).

[145] J. G. Rots. *Computational modeling of concrete fracture*. PhD thesis, 1988.

[146] Maria Francesca Pernice, Nelson V. De Carvalho, James G. Ratcliffe, and Stephen R. Hallett. Experimental study on delamination migration in composite laminates. *Composites Part A: Applied Science and Manufacturing*, 73:20–34, 2015. ISSN 1359835X. doi: 10.1016/j.compositesa.2015.02.018.

[147] Xiang Zhang and Caglar Oskay. Eigenstrain based reduced order homogenization for polycrystalline materials. *Computer Methods in Applied Mechanics and Engineering*, 297:408–436, 2015.

[148] Z Xiang and C Oskay. Sparse and scalable eigenstrain-based reduced order homogenization models for polycrystal plasticity. *Computer Methods in Applied Mechanics and Engineering*, 326:241–269, 2017. ISSN 0045-7825. doi: https://doi.org/10.1016/j.cma.2017.07.027.

[149] Jacob Fish, Vasilina Filonova, and Zheng Yuan. Hybrid impotent–incompatible eigenstrain based homogenization. *International Journal for Numerical Methods in Engineering*, 95(1):1–32, 2013.

[150] Jean-Louis Chaboche, Serge Kruch, Jean-François Maire, and T Pottier. Towards a microme-

chanics based inelastic and damage modeling of composites. *International Journal of Plasticity*, 17(4):411–439, 2001.

[151] Zeliang Liu, MA Bessa, and Wing Kam Liu. Self-consistent clustering analysis: an efficient multi-scale scheme for inelastic heterogeneous materials. *Computer Methods in Applied Mechanics and Engineering*, 306:319–341, 2016.

[152] David R Brandyberry, Xiang Zhang, and Philippe H Geubelle. A gfem-based reduced-order homogenization model for heterogeneous materials under volumetric and interfacial damage. *Computer Methods in Applied Mechanics and Engineering*, 377:113690, 2021.

[153] Gianluca Alaimo, Ferdinando Auricchio, Sonia Marfia, and Elio Sacco. Optimization clustering technique for piecewise uniform transformation field analysis homogenization of viscoplastic composites. *Computational Mechanics*, 64(6):1495–1516, 2019.

[154] Bilel Miled, Issam Doghri, Laurence Brassart, and Laurent Delannay. Micromechanical modeling of coupled viscoelastic–viscoplastic composites based on an incrementally affine formulation. *International Journal of solids and structures*, 50(10):1755–1769, 2013.

[155] Issam Doghri, L Adam, and N Bilger. Mean-field homogenization of elasto-viscoplastic composites based on a general incrementally affine linearization method. *International Journal of Plasticity*, 26(2):219–238, 2010.

[156] JL Chaboche, P Kanouté, and A Roos. On the capabilities of mean-field approaches for the description of plasticity in metal matrix composites. *International journal of Plasticity*, 21 (7):1409–1434, 2005.

[157] A. Vigliotti, G. Csányi, and V. S. Deshpande. Bayesian inference of the spatial distributions of material properties supplementary material. *Journal of the Mechanics and Physics of Solids*, 118:74–97, 2018. ISSN 00225096. doi: 10.1016/j.jmps.2018.05.007.

[158] Robert I Jennrich. Asymptotic properties of non-linear least squares estimators. *The Annals of Mathematical Statistics*, 40(2):633–643, 1969.

[159] Anil Aswani, Zuo Jun Max Shen, and Auyon Siddiq. Inverse optimization with noisy data. *Operations Research*, 66(3):870–892, 2018. ISSN 15265463. doi: 10.1287/opre.2017.1705.

[160] Gilbert Strang and George J Fix. An analysis of the finite element method(book- an analysis of the finite element method.). *Englewood Cliffs, N. J., Prentice-Hall, Inc., 1973. 318 p*, 1973.

[161] Paul T. Boggs and Jon W. Tolle. Sequential quadratic programming for large-scale nonlinear optimization. *Journal of Computational and Applied Mathematics*, 124(1-2):123–137, 2000. ISSN 03770427. doi: 10.1016/S0377-0427(00)00429-5.

[162] MA Tschopp, GB Wilks, and JE Spowart. Multi-scale characterization of orthotropic microstructures. *Modelling and Simulation in Materials Science and Engineering*, 16(6): 065009, 2008.

[163] Guido Dhondt. Calculix crunchix user's manual version 2.19. 2021.

[164] Michael W. Czabaj, Mark L. Riccio, and William W. Whitacre. Numerical reconstruction of graphite/epoxy composite microstructure based on sub-micron resolution X-ray computed tomography. *Composites Science and Technology*, 105:174–182, 2014. ISSN 02663538. doi: 10.1016/j.compscitech.2014.10.017. URL http://dx.doi.org/10.1016/j.compscitech.2014.10.017.